Montanuniversitaet Leoben

Doctoral Thesis

Combined atomic force and electron microscopy instrumentation to study microscale plasticity

Josef Kreith

Leoben, April 2015

April 30st, 2015

The doctoral thesis was typeset by the use of KOMA and LaTeX2_ε.

Affidavit

I declare in lieu of oath, that I wrote this thesis
and performed the associated research myself,
using only literature cited in this volume.

Leoben, April 2015

Acknowledgments

I want to thank my advisor Megan Cordill for the support during the last three years, without her purposeful help, this thesis never would have been finished. In hard times, she taught to work aim-oriented: The key to a successful experiment is in the lock to the laboratory door! I also want to thank Christian Teichert for sharing his AFM expertise during lectures and for his advice to improve this thesis.

I am grateful to Christoph Kirchlechner and Nataliya Malyar providing material and non-material support in micromechanics and beyond. The amicable atmosphere at the Erich Schmid Institute directed by Reinhard Pippan and Jozef Keckes was a solid basis to exchange knowledge. Among many staff members helping, I especially want to thank Thomas Schoeberl, Peter Imrich and Marlene Kapp for introducing devices and experimental techniques, or just allowing me to look over their shoulders and letting me ask annoying questions when they were busy with their own experiments. Within Megan's group, I want to thank Oleksandr Glushko, Barbara Putz and Julia Berger who provided support in thin film mechanics.

During my time at the Erich Schmid Institute I found out that most of the problems can be solved by either two approaches: Go to the workshop or ask the metallographer. Franz Hubner gave support for all kinds of (mechanical) problems and Silke Modritsch bailed me out whenever the excuse "I think this could be solved by using a microscope" was (or was not) applicable.

Office assignment is not a request program, but fortune brightly smiled on me and allowed me share the room with Matthias Bartosik, Stefan Hartl, D. Firneis, Andrea Lehner, Michael Meindlhumer and Michael Reisinger. Thanks for the nice time!

The way to the heart of a man is through the stomach: I want to thank Earl (getting grey) Karl Flicker, Juraj Todt, Ruth Treml and Juergen Spitaler for sharing many lunch (and office) hours. Fate has kept Karl's, Juergen's and my path close for about twenty years now!

The spark of the idea to start a PHD thesis arose during my stay at the Institut fuer Struktur- und Funktionskeramik, my first employer. I want to thank Robert Danzer for knocking at the eggshell to start the hatch-out-of-the-egg-process. I also want to thank Peter Supancic for the benevolent support. Clemens Krautgasser provided out of office training hours on the mountain bike.

A special thanks goes to Andreas Kleine and Carsten Michaelsen from Incoatec.

The support from GETec with Tobias Strunz and the AFM team at the EPFL Lausanne is acknowledged. I appreciate the patient help from Anne Mueller, Anfatec, who was providing the knowledge for (in vacuum) AFM experiments.

Thanks, KP for finding me.

Abstract

The yield point in metals depends of its chemical composition, the microstructure and lattice defects. In the last decades a plasticity size effect was also discovered, first shown with nanoindentation experiments and later in compression tests. An increasing number of research groups have investigated the plasticity size effect and have developed experimental methods and theoretical models, however, the size effect is still not fully understood yet.

Plastic deformation in face-centered cubic metals at moderate temperatures and strain rates is governed by the movement of dislocations. It seems obvious that the understanding of the behavior of dislocations in restricted volumes will reveal the mechanisms dictating the plasticity size effect. Different methods are used in literature to investigate plastic deformation and dislocations in constrained volumes. Compression-, tension- and bending-tests have been performed on micro-sized and nano-sized samples in the scanning electron microscope, atomic force microscope and the transmission electron microscope.

In this work, an atomic force microscope was developed that can simultaneously function inside a scanning electron microscope and was utilized for in-situ deformation studies to contribute to the understanding of the plasticity size effect. The new combined instrument is, in contrary to already existing solutions, compatible to various mechanical and micro-mechanical testing equipment. Microcompression and microbending tests have been performed to show the abilities in this field. A new method, called the "indent@edge" method was introduced. The new method is adopted for mechanical testing experiments in combination with atomic force microscopy. The sample preparation for the new method is less complex compared to the preparation of microbeams and micropillars. Thin metal films on polyamid were also strained in air to investigate the plastic deformation and reliability of the metal films for flexible electronic applications. The electrical resistance and the crack density were determined in dependency of the applied strain.

Kurzfassung

Die Flieszgrenze in Metallen haengt nicht nur - wie schon seit langem bekannt - von der chemischen Zusammensetzung, dem Gefuege und Gitterfehlern ab, sondern ist auch bei Einkristallen unter uniaxialer, monotoner Beanspruchung von der Groesze des beanspruchten Volumens abhaengig. Diese Tatsache wurde erst in den letzten Jahrzehnten erkannt, und wird seitdem von einer immer groeszer werdenden Anzahl an Forschungsgruppen untersucht. Unterschiedlichste experimentelle Methoden zur Untersuchung des Groeszeneffektes wurden angewandt, die entwickelten Modelle stimmen jedoch noch nicht vollstaendig mit den experimentellen Erkenntnissen ueberein.

Der maszgebliche Beitrag zur plastischen Verformung bei moderaten Temperaturen und Dehnraten in Metallen kubisch-flaechenzentrierter Gitterstruktur erfolgt durch Versetzungsbewegungen. Es ist naheliegend, dass ein Verstehen der Versetzungsdynamik und -statistik in Abhaengigkeit des Volumens zu einem Verstehen des Groesseneffekts bei plastischen Prozessen fuehren muss. Diesem Sachverhalt wurde durch Wahl der Untersuchungsmethoden Rechnung getragen: Druck-, Zug- und Biegeversuche mit Probengroeszen im Bereich von Mikrometern bis Nanometern wurden unter dem Rasterkraftmikroskop, Elektronenmikroskop und Transmissionselektronenmikroskop durchgefuehrt, um zur Aufklaerung des Groeszeneffektes beizutragen.

Diese Arbeit begleitete die Entwicklung eines in-situ Rasterkraftmikroskops, das im Rasterelektronenmikroskop eingesetzt werden kann und - im Gegensatz zu bereits vorhandenen Geraeten - mit Materialpruefapparaturen kompatibel ist. Das neue in-situ Geraet wurde in unterschiedlichen Versuchskonfigurationen im Rasterelektronenmikroskop als auch an Luft eingesetzt, um das plastische Verhalten von Metallen kubisch-flaechenzentrierter Kristallstruktur in unterschiedlichen Groeszenskalen zu untersuchen. Eine neue experimentelle Methode, die "indent@edge"-Methode wurde vorgestellt. Einerseits eignet sich diese Methode sehr gut fuer in-situ Versuche mit einem Rasterkraftmikroskop, andererseits ist ein einfacheres Herstellungsverfahren der Proben im Vergleich zu miniaturisierten Zug-, Druck- und Biegeproben zu erwarten. Abschlieszend wurden Versuche zur Charakterisierung des plastischen Verhaltens und der Zuverlaessigkeit duenner Metallschichten auf Polyamid an Luft durchgefuehrt. Diese Materialsysteme werden in Geraeten mit flexibler Elektronik eingesetzt. Die Rissdichte und der elektrische Widerstand der Metallschicht wurden in Abhaengikeit der Dehnung bestimmt.

"Why is it never easy?"
Detective William "The Bunk" Moreland
Baltimore Police Department, Homicide Unit

Contents

1. Introduction

1.1. Motivation

For many manmade goods used in everyday life, further development also means miniaturization. Reducing size and weight leads to easier handling, saving of raw materials, supplies and energy. In almost all fields of modern technologies miniaturization is an initial requirement and is often pushed further for each cycle of product evolution. The dimensions of structures in microelectronic devices, the paradigm of the micromechanics community, is being approached by single nanometers. A deep understanding of the change of material properties at decreasing length scales from millimeters, micrometers to nanometers has become mandatory. In this work a large chamber atomic force microscope for use in a scanning electron microscope is introduced to show its capabilities for in-situ micro- and nanomechanical testing to contribute to the understanding of material properties at small length scales.

1.2. Plasticity in metals

Mechanical stress in any material leads to deformation. Depending on the amount of stress, the change in shape can be temporary or permanent. The point were the stress is high enough to cause a permanent deformation is called the yield point, the deformation is called plastic. A deformation that is completely reversible is called elastic. The yield point not only depends on the chemistry of the material, but also on the microstructure and the density and type of lattice defects. In face-centered cubic (FCC) metals, plastic deformation is governed by the movements of dislocations [1, pp. 197]. These line defects, caused by the insertion of extra half planes in the crystal are thoroughly discussed in the books of Weertmann & Weertmann [2] and Hull & Bacon [3].

An image of a cubic crystal (lattice constant, a) with a single edge dislocation is shown in Figure 1.1. The inserted half plane is shown as blue circles, the dislocation line is orthogonal to the image plane and is seen as a dot. The position of the dislocation line is shown as blue circle with a cross, it is enclosed by the Burgers circuit (red lines). The Burgers vector, $\vec{b}$ (black arrow), is the difference to a Burgers circuit not enclosing a dislocation. The gray T facing upside down in the center of Figure 1.1 indicates the edge dislocation. The Burgers circuit encloses a single edge dislocation, so the length of the Burgers vector, $\vec{b}$, is equal to the lattice constant a of the crystal. A second type of dislocation, called screw dislocation, also exists [3, pp. 15] and [2, pp. 4]. For the screw dislocation, the Burgers vector, $\vec{b}$, and the dislocation line are

1
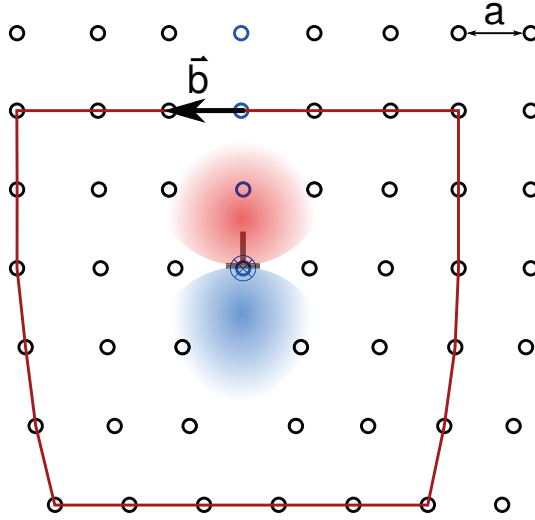
Fig. 1.1.: 2D sideview of a cubic crystal (lattice constant a) with an edge dislocation. The atoms are shown as circles. The inserted extra half plane is colored blue. The Burgers circuit is indicated as red lines, the Burgers vector $\vec{b}$ is shown as a black arrow. The dislocation line is seen as a dot, it is orthogonal to the image plane (blue circle with a cross). The colored areas in the center indicate compressive (red) and tensile (blue) stresses.

parallel to each other. Superpositions of both dislocation types are common and can be described by one and the same Burgers vector.

Inserting a halfplane into a perfect crystal leads to a distortion of the crystal lattice and to a strain of the atoms close to the dislocation line. The stored elastic energy E_{el} is [3, pp. 71]

$$E_{el} \approx G\vec{b}^2, \tag{1.1}$$

where G is the shear modulus. As the stored elastic energy increases with the square of the length of the Burgers vector, dislocations having short Burgers vectors are preferred. The stress field close to the dislocation line is indicated by the colored areas in Figure 1.1. Flipping the figure vertically would lead to a dislocation having a Burgers vector of opposite sign.

The interacting force of a stress field with a dislocation is described by a tensor law called the Peach-Koehler-Equation. Using

$$\vec{G} = \boldsymbol{\sigma}\vec{b} \tag{1.2}$$

the equation can be written in a simplified form [2, p. 61]

$$\vec{F} = \vec{G} \times \vec{t}, \tag{1.3}$$

where $\boldsymbol{\sigma}$ is the stress tensor, $\vec{b}$ the Burgers vector and $\vec{t}$ the unit vector tangent to the dislocation. The Peach-Koehler-Equation states, that the force on the dislocation always is directed normal to the dislocation line.

The movement of a dislocation in the plane of the Burgers vector and dislocation line is called slip, the according plane is called the slip plane. Slip is the preferred movement for dislocations in a FCC crystal at moderate temperatures and strain rates. Dislocations with opposite sign attract each other and can annihilate when they are situated on the same slip plane. A single dislocation also can be annihilated by escaping to the surface, creating a slip step.
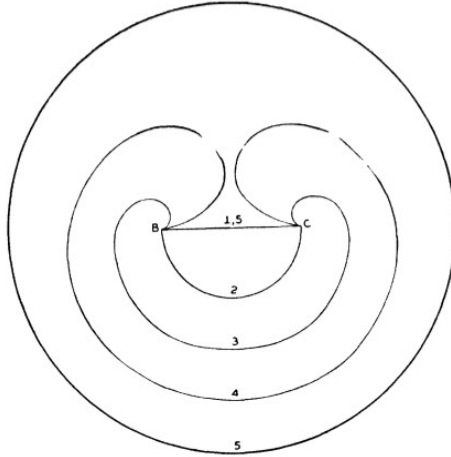
Fig. 1.2.: Frank-Read source [4]: A straight dislocation is pinned between two points B and C (1). A shear stress bows out the dislocation lines (2, 3, 4) until a new dislocation loop and new source is created (5) by annihilation of the converging flanks (4).

At large plastic strains it is common that new dislocations are created during plastic deformation of the material. The most important mechanism to create dislocations is the Frank-Read source [4], consisting of a dislocation pinned by connecting two points, which may be dislocation intersections, precipitates or another kind of defect. An applied shear stress bows out the pinned dislocation until it surrounds both pinning points in the form of a large kidney-shaped loop. The meeting flanks annihilate and create a circular shaped new dislocation on the one hand and a new Frank-Read source between the two pinning points on the other hand. The original drawing of Frank and Read is shown in Figure 1.2 [4]. If the circular dislocation is able to move away, new dislocations will be created. A dislocation pile up creates a back-stress eventually shutting down the dislocation source. The shear stress needed to create a dislocation with the help of a Frank-Read source (FRS) depends on the distance between the pinning points L and the shear modulus G of the material. It is given by [3, pp. 163]

$$\tau_{FRS} \approx \frac{Gb}{L}. \tag{1.4}$$

FCC slip systems

The close packed plane in FCC crystal systems is the $\{1\,1\,1\}$ plane, the direction of the shortest Burgers vector is a $\langle 1\,1\,0 \rangle$. The length is

$$|\vec{b}| = \frac{a}{2} \left| \begin{pmatrix} 1 \\ 1 \\ 0 \end{pmatrix} \right| = \frac{a}{\sqrt{2}}. \tag{1.5}$$

Slip directions different from the mentioned ones are energetically nonpreferential [3], giving 12 $\{1\,1\,1\}\langle 1\,1\,0 \rangle$ directions in total. Adjacent planes intersect along the $\langle 1\,1\,0 \rangle$ directions parallel to the Burgers vector. The $\{1\,1\,1\}$ surface and the three active slip planes form the so called Thompson tetrahedron (Figure 1.3), its faces indicate the slip planes and the edges the directions of the Burgers vectors [5]. The angle between the adjacent planes of the tetrahedron is $70.53°$.

Plastically deforming a $\{111\}$ surface of a FCC single crystal by indentation (Figure 1.3c) shows slip for all possible three intersecting slip planes, leading to three different slip lines at an angle of $60°$. The surface profile of the indented plane would look as shown in Figure 1.4.

To determine the number of dislocations emitted to the surface, the angle between the surface normal and the according slip direction is needed. Because of the high symmetry of the crystal the dot product is equal for all three out-of-plane directions

$$\frac{1}{\sqrt{6}} \begin{pmatrix} 1 \\ 1 \\ 1 \end{pmatrix} \cdot \begin{pmatrix} 1 \\ 1 \\ 0 \end{pmatrix} = \frac{1}{\sqrt{6}} \begin{pmatrix} 1 \\ 1 \\ 1 \end{pmatrix} \cdot \begin{pmatrix} 1 \\ 0 \\ 1 \end{pmatrix} = \frac{1}{\sqrt{6}} \begin{pmatrix} 1 \\ 1 \\ 1 \end{pmatrix} \cdot \begin{pmatrix} 0 \\ 1 \\ 1 \end{pmatrix} = \sqrt{\frac{2}{3}} \tag{1.6}$$

and zero for the in-plane directions. To create a slip step with a vertical height of h_v, the dislocations along the active slip-systems pointing out of the surface plane need to contribute by a total length, d_{ss}, of

$$d_{ss} = \frac{h_v}{cos\theta} = \sqrt{\frac{3}{2}} h_v. \tag{1.7}$$

In the case of the $\{1\,1\,1\}$ surface, both available slip systems (Figure 1.4b) may contribute by the same amount. By knowing only the step height and topography, it's not possible to distinguish if a single slip system or both slip systems are activated.

For the general case of an arbitrary surface and slip system the formula would be

$$d_{ss} = \frac{h_v}{\hat{a}_{ss}\hat{s}_n} \tag{1.8}$$

where $\hat{a}_{ss}$ is the unit vector in the direction of the active slip system, and $\hat{s}_n$ is the unit vector of the surface normal.
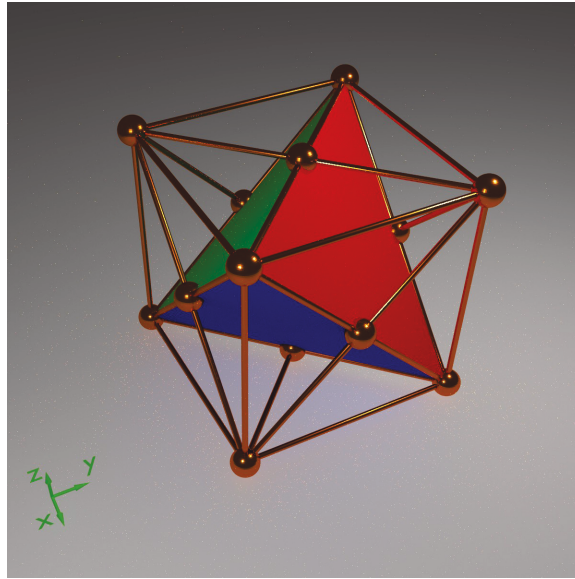
(a)
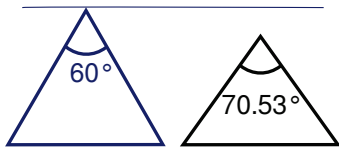
(b)
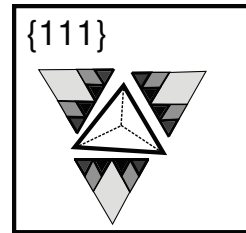
(c)

Fig. 1.3.: (a) Thompson tetrahedron with the following visible surfaces: $\{1\,1\,1\}$ (red), $\{\bar{1}\,\bar{1}\,1\}$ (green) and $\{1\,\bar{1}\,\bar{1}\}$ (blue). **(b)** Blue equilateral triangle, left: Contour of the blue $\{1\,\bar{1}\,\bar{1}\}$ surface of the tetrahedron, black triangle, right: Same as the blue triangle, but top corner moved to the top surface's center atom of the FCC unit cell, showing the dihedral angle of two $\{1\,1\,1\}$ surfaces. **(c)** Slip line patterns close to an indent imprint on a $\{1\,1\,1\}$ surface. Angles of 60° are formed by the slip planes.
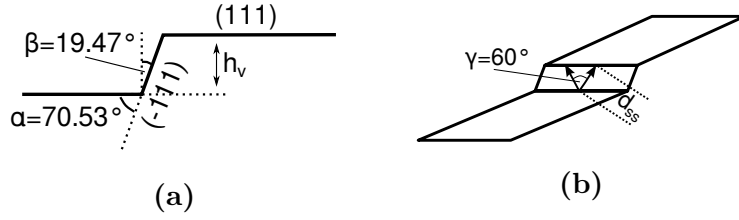
Fig. 1.4.: Typical profile of a single slip step randomly chosen from an indented FCC $\{1\,1\,1\}$ surface. (a) Angles of ascending slip-planes: α is one of the Thompson tetrahedrons dihedral angles (see Figure 1.3b), β is the angle of the vertical slip plane direction with the surface, h_v is the vertical step height, which easily comes from AFM measurements. (b) Slip directions in the $\{\bar{1}\,1\,1\}$ slip plane, d_{ss} contribution of the according slip-system to the total vertical step height.

1.3. Small scale plasticity, micro-mechanical testing

The yield point of a material depends on properties such as the chemistry of the material, the microstructure as well as the density and type of lattice defects. A size dependence of the flow stress σ_y in polycrystalline metals with the grain diameter d was found with the Hall-Petch relation in the middle of the last century [6, 7]:

$$\sigma_y = \sigma_{y0} + \frac{K}{\sqrt{d}} \qquad (1.9)$$

where σ_{y0} is the flow stress without grain boundaries and K is the grain boundary resistance. Another well known plasticity size effect is the indentation size effect described by Nix and Gao [8]. They used the concept of geometrically necessary dislocations (GNDs) to explain the increase in hardness H with smaller indentation depths h, finding the following form for the depth dependence of the hardness:

$$\frac{H}{H_0} = \sqrt{1 + \frac{h^*}{h}} \qquad (1.10)$$

where h^* is a characteristic length that depends on the shape of the indenter. Also uniaxial microcompression test experiments, show a strong size effect for the yield strength [9]. The lack GNDs in this kind of experiments shows, that there are other mechanisms contributing to the size effect, which are not fully understood yet.

1.4. Observation of dislocations

Dislocations are phenomenons at the atomic scale and therefore not directly viewed with an optical microscope or scanning electron microscope (SEM). They are only detected with instruments providing atomic resolutions. The transmission electron

microscope (TEM) makes dislocations visible by the distorted crystal lattice close to the dislocation effecting the electron diffraction. This leads to dark lines on the TEM image [3, pp. 22]. Also the scanning tunnel microscope (STM) provides an atomic resolution, making dislocations directly visible at surfaces [10].

Indirect methods to investigate dislocations are looking at etch pits or slip steps with the optical microscope, SEM or atomic force microscope (AFM). Etch pits are caused by different atom removal rates close to dislocations during surface etching, caused by the different bonding energies of the strained crystal structure. Slip steps are the traces of dislocations which escaped to the surface.

In this work, AFM and SEM, two real space imaging methods, were combined for in-situ investigation of sample surfaces during micro-mechanical testing experiments. Both methods are introduced in the following sections.

1.4.1. The scanning electron microscope

In the middle of the 19th century, Ernst Abbe was working on the improvement of optical microscopes. He found out, that when using light waves for imaging objects in the far field (Fraunhofer region) a theoretical resolution limit can not be overcome. Objects smaller than about half the wavelength of the incoming light cannot be resolved using an optical microscope [11, pp. 246]. The scanning electron microscope (SEM) provides matter waves having wave lengths easily adjustable by the electron acceleration voltage, much smaller compared to visible light.

The electron microscope was invented in the early 20th century by Knoll and Ruska [12], the first SEM was developed a few years later by Ardenne [13]. A focused beam of accelerated electrons is scanned on a sample surface in a raster scan pattern with acceleration voltages of $0.1\,kV$ to $30\,kV$. The electrons enter the sample surface and are scattered elastically or inelastically. The diameter of the electron beam on the sample surface is in the range of $1\,nm$ to $2\,nm$, the scattered electrons interact in a larger sample volume limiting the resolution depending on the acceleration voltage. The scattered electrons are detected by 1D electron detectors, a gray scale image is calculated from the position of the scanning electron beam and the number of scattered electrons detected at that position. The number of scattered electrons depends on various parameters like the surface chemistry and topography.

1.4.2. The atomic force microscope

A few years after the invention of the scanning tunnel microscope (STM) [14] the atomic force microscope (AFM) was invented in the late 20th century by Binnig, Quate and Gerber [15]. An ideally atomically sharp tip attached to a flexible cantilever is scanned on a sample surface with typical scan ranges of $0\,\mu m$ to $100\,\mu m$ and a scanning resolution better than single nanometers. The interaction of the tip with the surface affects the deflection of the cantilever which is kept constant by the AFM scanner motor controller by retracting or approaching the tip. By exactly knowing the scanner
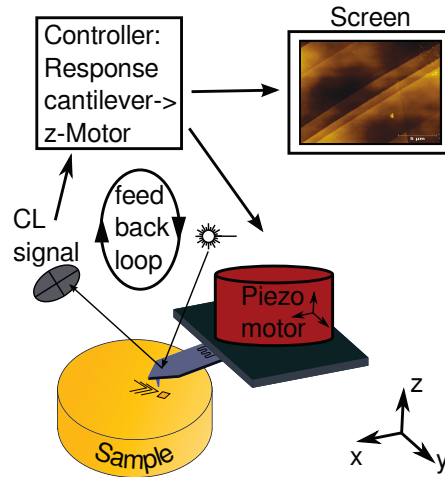
Fig. 1.5.: Schematic of an AFM working principle. A sharp tip is mounted on a flexible cantilever to scan the sample surface. The interaction force of tip and surface is indicated by the deflection of the cantilever and kept constant by the AFM scanner motor controller.

parameters the controller calculates a height topography image from the scanner's x-, y- and z-position. A schematic is given in Figure 1.5.

Two different methods to detect the deflection of the AFM cantilever are shown in Figure 1.5. Systems with an optical lever [16] use a laser beam reflected at the cantilever beam which is detected by a position sensitive photo diode. Self-sensing cantilevers are coated with a piezoresistive material [17] and are connected to a electronic readout circuit. The working principle of self-sensing cantilevers is comparable with the application of strain gauges [18].

1.5. In-situ scanning probe microscopy instruments

Various setups for in-situ scanning probe microscopy instruments (SPMs) have been developed and are introduced in the literature. The following sections give an overview and applications of in-situ instruments used inside of the SEM as combined SPM/SEM devices and standalone devices used outside of the SEM for in-situ mechanical testing experiments.

1.5.1. Existing solutions for combined SPM/SEM instruments

Just a few years after STM and AFM were invented, people were thinking of using them inside of SEMs to combine the complementing benefits of the imaging methods. SEMs provide images with large scan areas up to a few square millimeters at high scan rates, AFMs provide a high resolution surface topography down to the atomic scale, but have limited scan ranges of up to about 100 µm x 100 µm. In the simplest case, the

SEM can be used only as a replacement or enhancement of the optical microscope, which is commonly used in conventional AFMs, to locate and position for AFM scanning. Compared to the optical microscope, the SEM provides higher magnifications and depth of fields but lower recording times. In the more advanced case, images of the SEM giving lateral topographical and chemical information at quite fair resolutions down to the scale of nanometers are combined with SPM scans having atomic resolutions in lateral and vertical directions. In the case of the AFM mechanical, electrical, magnetic and many other properties of the surface can be combined with SEM data gathered via advanced equipment like electron backscatter diffractin (EBSD) or energy dispersive X-ray spectroscopy (EDX).

Existing combined solutions: A chronological overview

In 1988, six years after Binnig's, Rohrer's, and Gerber's work introducing the STM technique [19, 14], Vasquez [20] demonstrated a STM incorporated to a SEM instrument (Figure 1.6a). SEM- and STM-images of a stamper used to fabricate optical discs were made, having a spatial resolution of about 1 nm in the lateral and vertical directions. Issues with sample contamination caused by the SEM electron beam acting as an insulating layer inhibiting the STM tunneling current were mentioned.

In the year 1994 Ermakov [21] introduced a custom made combined AFM/STM/ SEM instrument. In AFM mode, the SEM beam electrons are scattered off the AFM cantilever and used as the deflection signal, see Figure 1.6b. Even with the turbo pump of the SEM operating, an atomic resolution was achieveable due to the compact design of the device.
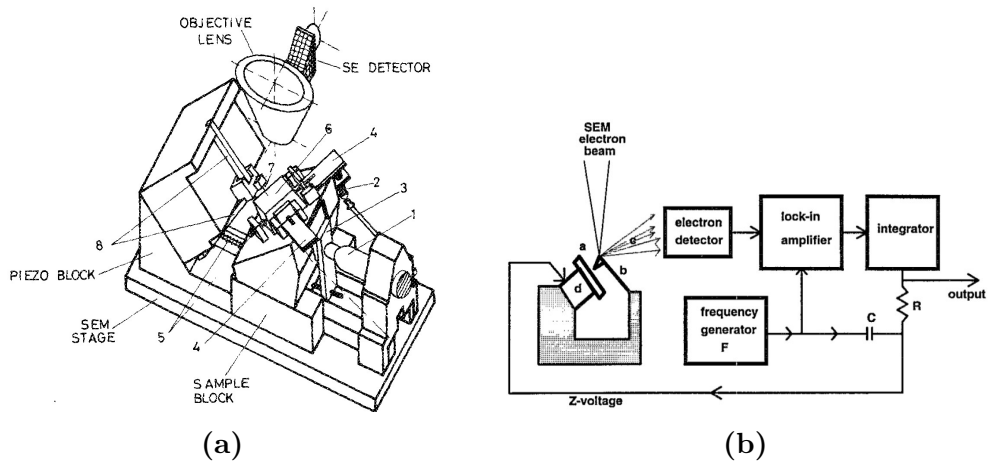

Fig. 1.6.: (a) Vasquez [20] and **(b)** Ermakov [21] showing the schematics of their combined SPM/SEM instruments.

In the same year as Ermakov, Stahl [22] showed a custom made AFM (Figure 1.7a) equipped with piezoresistive cantilevers [17], [23, pp. 9] imaging a transmission diffraction grating and conducting paths on integrated circuits. Stahl also referred to a

commercially combined AFM/SEM instrument using an optical lever to detect the AFM cantilever deflection from the company Topometrix [24].

Emundts [25] investigated reactive metal surfaces using a Besocke-type [26] STM in a SEM under UHV conditions. The instrument can simultaneously operate in STM and SEM mode. With the STM atomic resolution is possible and the resolution of the SEM is about 80 nm. Bauerdick [27] used an in-situ AFM to analyze tungsten carbide structures during deposition of silicon inside of a SEM. The AFM, provided by Kleindiek Nanotechnik GmbH [28] (Reutlingen, Germany) is equipped with self-sensing, piezoresistive AFM cantilevers to achieve a compact and guidable setup. Celik and Madenci [29] performed mechanical testing experiments on nanowires in a SEM, using the AFM cantilever of their custom made AFM for imaging and as an indenter to bend the nanowires. The deflection of the AFM cantilever is probed by an optical lever, see Figure 1.7b.

(a)   (b)
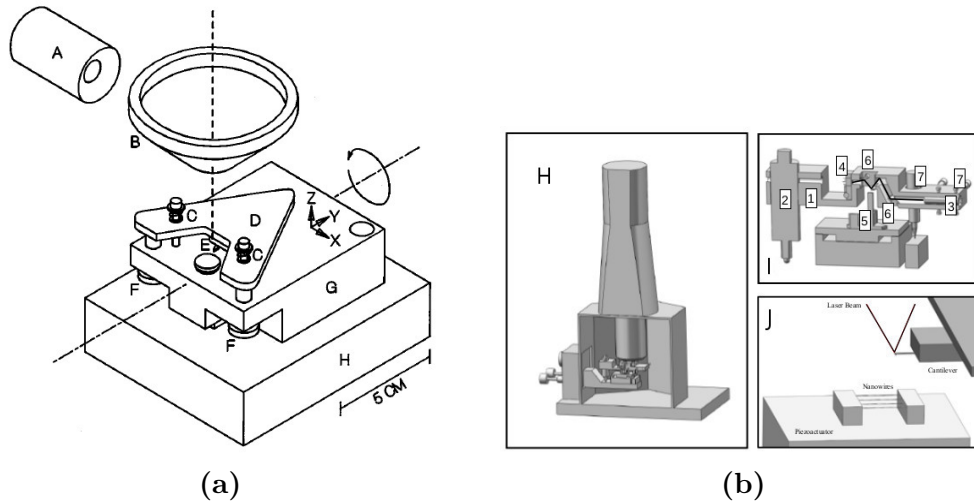
Fig. 1.7.: Schematics of **(a)** Stahl [22] showing components of the SEM (A, B, H) and the AFM (C, D, E, F, G) with a piezoresistive cantilever and **(b)** Celik [29] showing (H) the SEM chamber, (I) the AFM with optical lever and (J) an in-situ setup for testing nanowires.

Most of the AFM/SEM devices described have one thing in common: a very compact device with a small mechanical loop to minimze the influence of vibrations from the SEM turbo pump. The aim of this work is to develop a large chamber AFM for use in the SEM, to contradict designs with a small mechanical loop, which are not compatible with testing equipment for in-situ micro-mechanical experiments. The only author showing a device which could achieve this task in principle is Bauerdick, but no literature of mechanical testing experiments using this setup was found.

1.5.2. In-situ AFMs in material science

SEM and AFM as separate instruments are commonly used for in-situ mechanical testing at a wide range of length scales. Oele [30] developed a three-point bending system compatible with an AFM for in-situ studies of slip in ionic crystals to connect the applied stress distribution in a bent sample with the activation of specific slip planes. Franciosi [31] and Kahloun [32] analyzed slip in single crystalline iron samples having dimensions of millimeters by using a SEM for in-situ compression tests and an AFM for in-situ tensile tests. The main goal of the investigation was to contribute in finding the type and the distribution of activated slip systems in body-centered cubic (BCC) crystals during plastic deformation. Coupeau [33] investigated millimeter sized Nickel-based alloys and LiF single crystals using an AFM during in-situ compression test. They developed a statistical analysis method to determine step height and terrace width of slip steps to identify dislocation sources during compression test experiments. Coupeau and coworkers [34, 35] also investigated the size of thin film buckles to evaluate the adhesion of the film and the substrate. Fukushima used an AFM for micro-mechanical tests on µm to nm sized samples inside of a SEM [36, 37]. Motz et al. performed bending tests on focused ion beam (FIB) machined micronsized beams using a nanoindenter mounted on a commercial AFM [38] to investigate the plasticity size effect in copper. Celik probed the mechanical properties of copper nanowires in a custom made combined AFM/SEM instrument [29]. Figuera, Egberts and Filleter studied dislocations using an STM [10] and AFM [39, 40] for imaging and to indent the surface of gold and KBr single crystal samples in ultra high vacuum (UHV). Nibur, Somerday and Bahr [41] looked at the effect of hydrogen on stainless steel leading to dislocation nucleation and motion at lower indentation loads.

Within this work, a novel combined AFM/SEM instrument was used to investigate microscale plasticity in FCC metals. In-situ material testing experiments were carried out inside of a SEM using a commercial picoindenter. The novel AFM instrument was used to analyze the height and the distribution of the slip steps to evaluate the number of dislocations generated during the mechanical testing experiment.

2. Instrumental
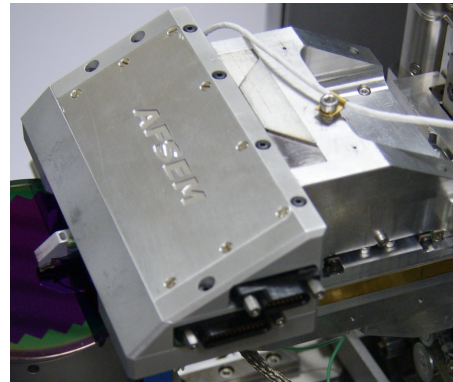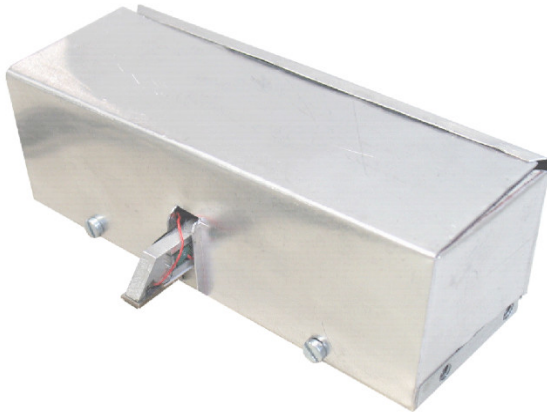
From the very first concepts to the scientific prototype.

2.1. Considerations when using a large chamber AFM in a SEM

When utilizing a large chamber AFM inside of a SEM for in-situ mechanical testing, the following issues gain importance:

- **Thermal drift:** The variety of materials for use inside of a SEM is restricted. Vacuum compatibility, a low mass density and restrictions to the magnetic properties are narrowing the available options. Granite, a typical material for use in air with a very low coefficient of thermal expansion of $5 - 7\,\mu m/K$[1] cannot be used inside of a SEM. Minimizing drift also is an issue for the design of SEM instruments, but the higher SEM scanning speeds make it less critical compared to AFMs.

- **Vibrations:** The vacuum system of a SEM, usually consisting of a rotary pump located in a neighboring room and a turbopump directly attached to the SEM housing are both potential sources of vibrations. Vibrations can be transferred

---

[1]The coefficient of thermal expansion of Aluminum at room temperature is $23.1 \cdot 10^{-6}/K$. Aluminum is a lightweight and well workable metal, often used for structural components. A change in temperature of $0.1\,K$ of an AFM component having a length of $10\,cm$ results in a drift of $23\,nm$. That's 2% of the total scan size when scanning an area of $1\,\mu m \times 1\,\mu m$.

via the vacuum hoses in the case of the rotary pump and in the case of the turbopump the vibrations are directly transmitted to the SEM housing. Electric cables connected to the SEM and SEM equipment can also transmit foot fall sound to the inside of the SEM chamber. SEMs are equipped with sophisticated vibration damping systems, but the requirements for AFMs are even higher to allow the high spatial resolutions in z-direction.

- **Vacuum environment:** A great difference in the in air and in vacuum environment is the different damping of the cantilever in tapping mode, leading to higher Q-values and lower scan speeds. Other factors like potential heating issues of motors and electronic components of the AFM caused by the limited heat conduction also should not be underestimated. Last but not least it should be mentioned that pumping times may prolong the time schedule of the test procedure in vacuum, for example if the cantilever needs to be replaced. The pumping time strongly depends on the SEM instrument used. It can take 15 minutes up to several hours. A change in temperature caused by venting and pumping the chamber leads to thermal drift until achieving thermal equilibrium again. In air, the cantilever replacement should be a simple task, performed in quite a short time.

- **Cabling:** Signal- and control voltages are conducted along long cables and feedthroughs. A pre-amplifier close to the AFM cantilever is needed for reliable signal processing: An electromagnetic interference between the wires must be avoided.

- **Interference of AFM and SEM**: The voltages for the scanner- and tapping piezos may influence the performance of the SEM. The SEM electron beam could effect the performance of the self-sensing cantilever. For high resolution imaging both instruments need to be able to be put into a standby mode to minimize these interference effects.

The combined AFM/SEM instrument for in-situ mechanical testing was developed having the issues mentioned above in mind. The details of how these were overcome will be described in the next section.

2.2. Description of the combined AFM/SEM instrument

In this section the new combined AFM/SEM instrument is described. First the single components of the device with respect to the special adaptions for use in a SEM environment and in-situ testing are explained. After that the characteristics of the instrument, performance tests and methods to improve the performance are shown.

2.2.1. Components

The single components of the combined AFM/SEM instrument are described below. Before introducing them in detail in the following sections, a list with the name of the components and their function is given in Table 2.1.

Component name	Function
Scanner	The AFM cantilever is mounted on the scanner for scanning the x, y and z directions in the range of microns to tens of microns during surface imaging.
Cantilever and readout	The AFM cantilever tip interacts with the surface topography, the readout electronics detect the response of the cantilever to the surface interaction.
AFM controller	The controller interprets the readout signal of the cantilever and controls the AFM scanner via feedback control. The data is recorded and converted into a topography image.
High voltage amplifier	The low voltage control signal of the AFM controller is amplified to a high control voltage of the scanner piezos.
Coarse positioning stage	The AFM scanner is mounted on the the coarse positioning stage for movements in the range of millimeters to centimeters, providing a flexible setup.

Table 2.1.: List of components of the combined AFM/SEM instrument.
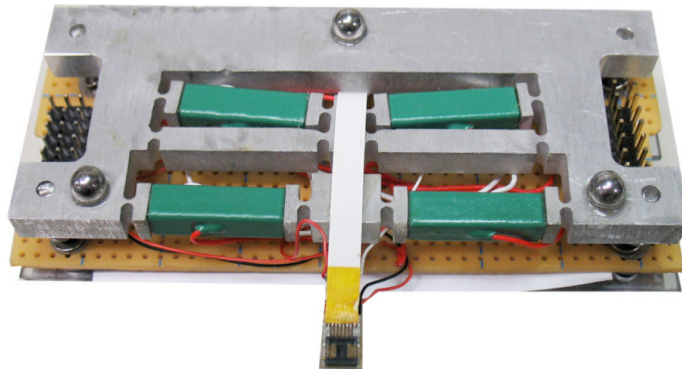
AFM Scanner

Fig. 2.2.: Flexure structure and multilayer piezoactuators of the first prototype x- and y-scanner.

The AFM scanner scans the AFM cantilever on the surface of the sample. It has to provide high scan ranges and speeds, along with a linear voltage-deflection behavior

14

combined with compact dimensions. Negative effects like scanner bow and mechanical crosstalk should be minimized to reduce effort in image postprocessing. The scanner of the combined AFM/SEM instrument is driven by multilayer piezo actuators arranged in three independent frames for x-, y- and z-movement utilizing flexure structures [42]. The frames act as an amplifier for the mechanical movement of the piezos, the independent setup provides a minimum of mechanical crosstalk. An early design of the flexure structure is shown in Figure 2.2. The scanner is developed by GETec [43], the maximum scan range for the current prototype is 27 µm x 27µm in x- and y-direction and 6.8 µm in z-direction, the current prototype operates in open-loop mode, later models will work in closed-loop mode, making scanner calibration unnecessary.

AFM Cantilever and readout

(a)   (b)
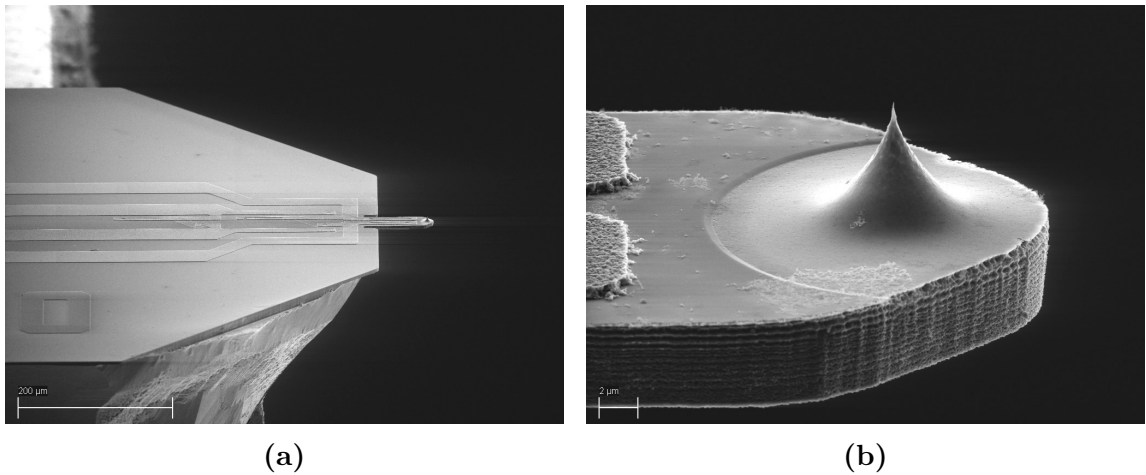
Fig. 2.3.: AFM cantilevers provided by SCL-SensorTech. **(a)** Overview of the cantilever and the cantilever base showing the conductive paths for the piezo-resistive bridge to detect the cantilever deflection. **(b)** AFM Tip.

The cantilever of the AFM was developed to provide a compact footprint of the AFM for easy use and positioning inside of the SEM chamber. Electric self-sensing cantilevers with piezo-resistive [23] bridge deflection sensors were found to fullfill these requirements best. Contrary to a optical lever [16] readout, no laser system including mirrors and no optical detector is needed. The electrical signal of the cantilever is preamplified in the AFM housing inside of the SEM chamber to minimize electrical noise and electrical crosstalk. The design and dimensions of the cantilever were improved to have a resonance frequency and a Q-factor suitable for a vacuum environment. The cantilevers are developed by SCL-SensorTech [44]. In vacuum, the Q-factor of the current cantilevers is about 1000 to 4000, that is quite a good value even compared to the values in air of 200 to 400. A typical resonance frequency is 700 kHz. The geometry of the cantilevers is 85 µm x 30 µm, the thickness is 3 µm to

4 μm and the tip radius is about 10 nm. The AFM cantilever's deflection sensitivity is in the range of 1 μV/nm to 4 μV/nm. Two SEM images of the cantilever and cantilever tip are provided in Figure 2.3.

AFM controller: Hardware and software

The AFM controller and software need to be able to operate the AFM in air and in vacuum. The system provides a Q-control [45] option (see Section 2.2.3) to improve scanning speeds in vacuum. An adaptation of hard- and software was possible during the development of the AFM to follow unavoidable changes of the AFM device. The high voltage amplifiers for the multilayer piezos of the AFM scanner need to be flexible to drive different type of piezos. In case of a failure during testing the AFM prototype, backup channels of the high voltage amplifier and fast and uncomplicated serviceability are of high interest. The AFM software and controller were provided by Anfatec [46], the high voltage amplifier by Techproject [47].

A coarse positioning stage is needed to align the AFM cantilever to the SEM electron beam and for the coarse AFM cantilever approach to the sample surface. The positioning of the sample surface in respect to the cantilever tip and SEM electron beam is provided by the SEM stage. The coarse stage was developed by the Montanuniversitaet Leoben, details are given in Appendix D.

2.2.2. Characteristics and tests

An important part of this work was the characterization and testing of the AFM prototype during its development. Performance tests of the scanner and compatibility tests with the SEM and mechanical testing setup have been carried out. The mechanical noise performance of the AFM scanner and the drift behavior of the AFM mounted on the coarse positioning stage were tested.

Performance of the AFM z-scanner

The scanner is made of three independent frames with flexure structures and multilayer piezoactuators to provide the movements in x-, y-, and z-direction. The flexure structure clamps the multilayer actuators in elastic tension to prevent the formation of cracks inside of the actuators and amplifies their displacement when a electrical voltage is applied. Figure 2.4 shows a schematic sideview of the AFM nose, which provides scanning in the z-direction.

The flexure structures, indicated by blue arrows in Figure 2.4, act as mechanical hinges to transfer and amplify the deflection along the axes of the piezoactuator to a pure z-movement of the mounted AFM cantilever. Lowering the thickness of the structure improves the performance of the AFM nose. If the structure gets too thin, a low spring constant and poor mechanical stability can lead to damage of the multilayer actuators during operation or lead to damage of the nose during the mounting of the cantilever. The deformation of the flexure structure must be purely elastic.
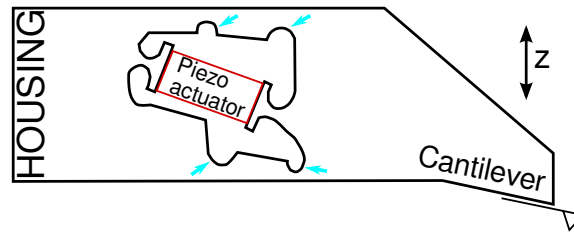
Fig. 2.4.: Schematic sideview of the AFM nose providing scanning in the z-direction. The nose is mounted on the AFM housing on the left side, the AFM cantilever on the bottom right. The blue arrows indicate the positions of the flexures.

To improve the performance of the AFM nose and to make sure that the yield strength of the material in the flexure structure is not exceeded, a mechanical simulation using a finite element method (FEM) model was performed. For this purpose, the software ANSYS Structural Mechanics, Release 14.5 was used. Figure 2.5 shows the simulation for an older prototype version. The performance was much lower than expected and was improved for the current prototype.
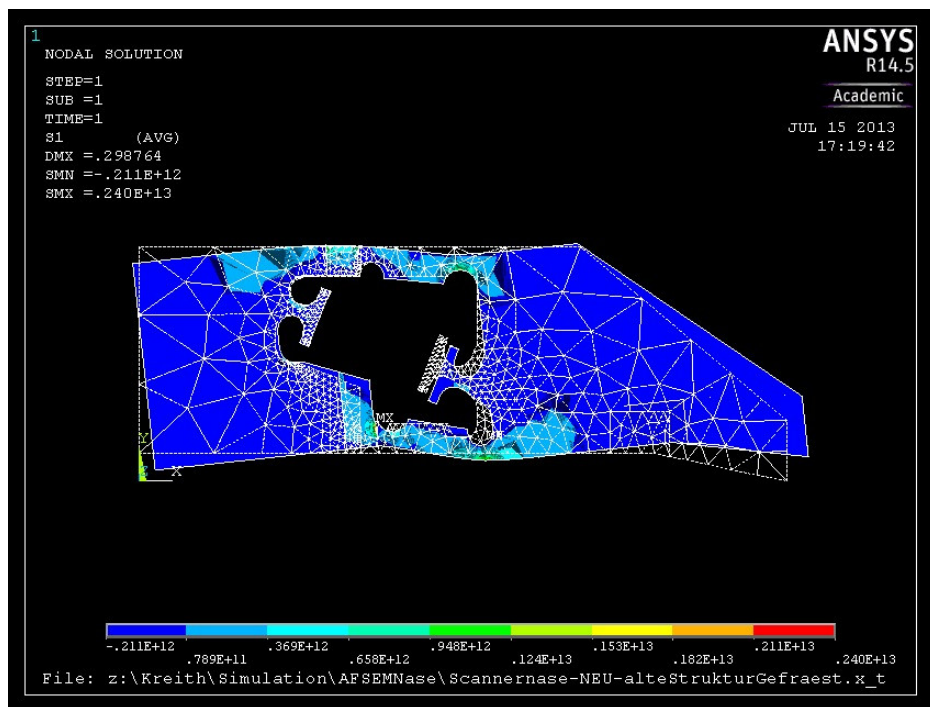
Fig. 2.5.: Solution for the first principal stress of an ANSYS FEM model for a legacy prototype version of the AFM nose.

The solution for the first principal stress in Figure 2.5 shows, that the flexure structures were chosen to be too thick. The mechanical stresses reach far into the bulk material of the nose, leading to an unwanted deformation of the material surrounding

the flexure structure. The unexpected deformation can also lead to mechanical cross talk effects. Furthermore, the high stiffness of the flexure structure leads to performance losses for the piezoactuator. A detailed study and parameter variation was done by the developers of GETec using the software SolidWorks.

Eigenmodes of the AFM scanner

The coarse positioning stage of the AFM and the AFM housing and the SEM stage and the SEM sample holder can be seen as two arms of a tuning fork. This configuration is called a "mechanical loop", having characteristic eigenfrequencies depending on the size and mass of the structure. A setup with low eigenfrequencies in the range of 1 Hz to 50 Hz is susceptible to vibrations of the building, foot fall sound and acoustic noise.

The vibration behavior of the AFM housing was tested using an Agilent 4294A impedance analyzer. The output- and input-signals for the impedance analyzer were amplified using the Anfatec AFM controller and the Techproject high voltage amplifier. The amplified output signal was connected to the x-, y- and z-piezoactuators of the AFM scanner by adding the signal to the output signal of the AFM controller. The signal from the AFM cantilever operated in AFM contact mode was used as the input signal for the Agilent impedance analyzer. During the experiment, the AFM was operated in contact mode using the normal Anfatec controller and software. The type of sample should not have too much influence on this experiment. A flat and hard material is preferable, therefore mica was used. The scan range was set to zero and the gains to very low values to compensate possible drift as well as to keep the distance between surface and cantilever constant. The results of the tests are shown in Figure 2.6.

The slow scanning axes in y-direction shows the lowest eigenfrequency of about 300 Hz followed by the fast scanning x-direction of about 3 kHz. The eigenfrequency of the AFM nose providing the scanning in z-direction is 5 kHz. Similar results are obtained by tapping the AFM housing using a screwdriver or pencil. The voltage of the piezoactuators is recorded using an oscilloscope configured to trigger single events. For all three axis a damped oscillation can be seen. The frequencies of the oscillations are listed in Table 2.2.

	x	y	z
Frequency	2.2 kHz	900 Hz	7.7 kHz

Table 2.2.: Eigenfrequencies determined by tapping the AFM housing and recording the voltage of the piezoactuators.

By tapping the AFM housing, not necessarily the first eigenmode recorded in Figure 2.6 is activated. A mechanical crosstalk between the axis was also detected by both methods. In the first method the crosstalk is indicated by peaks on different axes at exactly the same frequency, with the oscilloscope crosstalk can be detected by tapping the frame responsible for the x-axis and reading the signal from the piezoac-
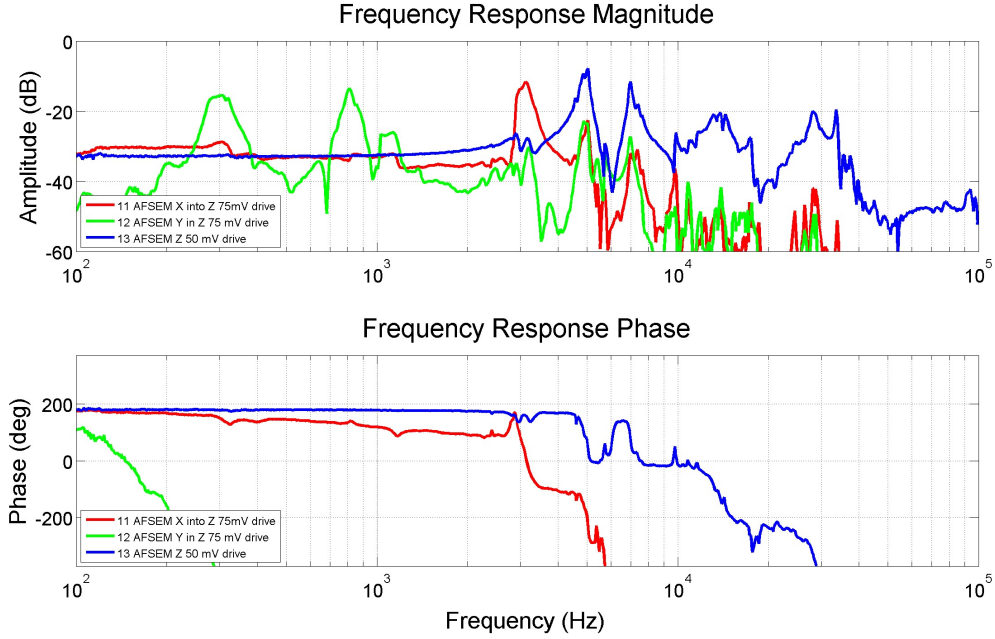
Fig. 2.6.: Spectrum of eigenfrequencies for the AFM scanner. All three scanning axis have been tested. The eigenfrequencies are 300 Hz in x-direction, 3 kHz in y-direction and 5 kHz in z-direction.

tuator for the y-axis. The design of the AFM housing is not limiting the performance of the combined AFM/SEM instrument according to mechanical vibrations.

Drift tests

The main contribution to drift is thermal. But also a mechanical drift of the AFM coarse stage in z-direction was identified. The drift of the coarse stage is initiated by traveling more than one millimeter in z-direction and stops after waiting five to ten minutes. It is caused by the geared belt drive. After reaching thermal equilibrium, the drift on all axes is lower than 0.5 nm/s.

2.2.3. Influences on scanning speed

The maximum scanning speed is determined by the feedback loop and the design of the scanner and cantilever [48, 49]. The eigenfrequencies of the x- and y-scanner need to be significantly higher than the scanning speeds to be able to operate without introducing artifacts. For the desired scanning speeds of up to 10 lines per second, this is easily fulfilled by the new AFM instrument (Section 2.2.2). The cantilever's Q-factor expresses the dissipated energy per oscillation and is correlated with the damping of

the cantilever. For a single damped mass-spring system the formula for Q is

$$Q = \frac{\sqrt{Mk}}{D}, \tag{2.1}$$

where k is the spring konstant, M the mass and D is the damping coefficient. A high Q-factor limits the scanning speed in tapping mode caused by a long transient response time of the cantilever to change its oscillation amplitude [50]. The transient response time, τ, is given by

$$\tau = \frac{Q}{\pi f_c} \tag{2.2}$$

where f_c is the resonance frequency of the cantilever. Fairbairn shows a schematic of an AFM cantilever scanning a vertical step with the z-axis feedback controller turned off. A cantilever with a lower Q-factor responds faster to the change in sample topography (Figure 2.7) [50].

Sample Surface

(a)

Sample Surface

(b)
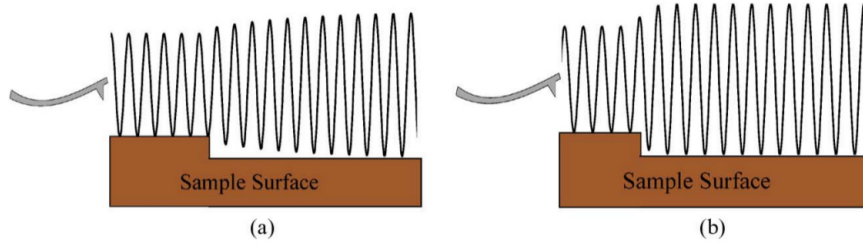
Fig. 2.7.: Fairbairn showing the different response times of cantilevers with different Q-values [50]. **(a)** Higher Q-value, **(b)** lower Q-value.

Accepting a skewed step having a width of 20 nm for a perfect vertical step[1] such as shown in Figure 2.7 would limit the scanning speed to about 2 μm per second. This value was calculated using Equation 2.2 and the cantilever data provided in Section 2.2.1. The scanning speed can be further improved by using the Q-control [45] option provided by the AFM controller software, leading to an improvement by almost a factor of two. Q-control adds a phase-shifted amplitude signal on the tapping piezo to artificially increase the cantilever's damping. If the sample surface is hard enough not to be damaged by the AFM cantilever, the preferred AFM mode for the instrument in vacuum is contact mode, providing higher scanning speeds compared to tapping mode. The maximum settings for the gains of the feedback loop are limited by vibrations of the system which otherwise can lead to resonance effects.

---

[1]The value was chosen to have twice the AFM cantilever tip radius. For a scan range of 20 μm and a scan resolution of 512 lines, the linewidth is 40 nm, allowing a scanning speed of 4 μm per second.

2.3. Experimental configurations of the combined AFM/SEM instrument

The AFM instrument can be used as a stand-alone instrument inside and outside of the SEM chamber. The main goal of its design was creating an instrument compatible with various mechanical testing setups and SEM accessories. One mechanical testing setup in vacuum and one in air is introduced in the following two sections.

In AFM literature, the terms in-vivo, in-vitro, and in-situ are often used for high-speed AFM "real time" experiments, such as the observation of living biological specimens. In the context of this work the expression "in-situ" is used to describe the ability of the instrument to record topography images during mechanical testing experiments. The testing sample is loaded in consecutive steps, the AFM scans are recorded in between the steps. A loading of the sample and simultaneous AFM scanning is not possible.

2.3.1. Combination with a picoindenter

(a)   (b)
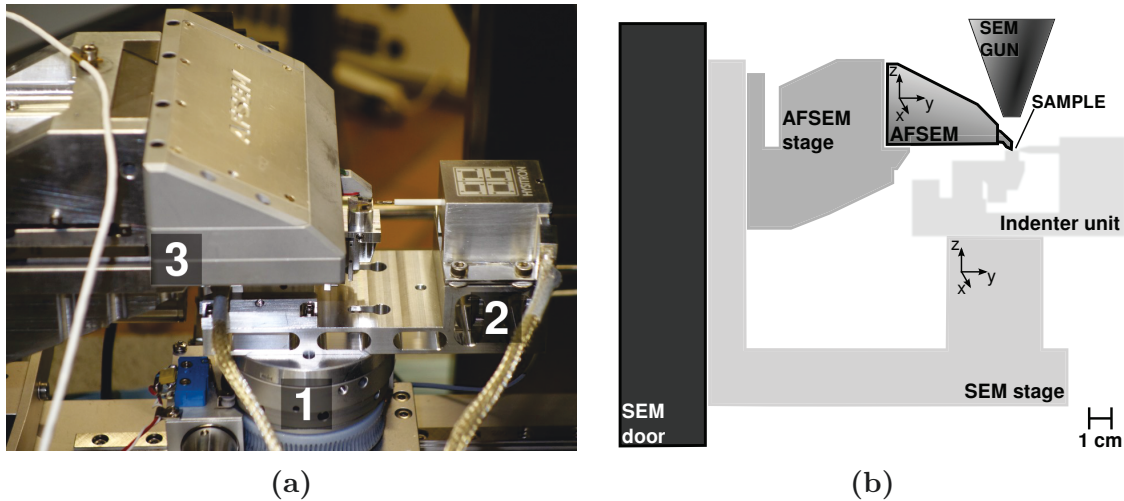
Fig. 2.8.: Photo and schematic of the micromechanical testing setup in the SEM for in vacuum experiments. **(a)** (1) SEM stage, (2) Picoindenter and (3) AFM. **(b)** Schematic drawing of the setup.

Figure 2.8 shows (a) a photo and (b) a schematic of the opened SEM chamber with the AFM mounted on the SEM z-stage on the left side. The picoindenter is mounted on the SEM stage. The AFM can be moved separately by the coarse stage enabling samples and equipment with different heights from 0 cm to 7 cm. The movement of the AFM in the y-direction allows for the retraction of the AFM for high quality imaging with the SEM secondary electron detector (SE detector). The x-direction is only needed to align the AFM cantilever with the SEM beam.

The Hysitron picoindenter [51] can be used with different indenter tips. The maximum indentation force is 10 mN, the maximum indenter deflection is 15 µm. It is equipped with a 3D sample stage to align the sample with the indenter tip. The setup was used for the "indent@edge"-experiment (Section 4.2) and for microbending and microcompression tests (Section 4.4).

2.3.2. Mechanical testing in air

The AFM is also capable of in-situ in air testing. Figure 2.9 shows a setup with a Kammrath & Weiss [52] straining stage. The SEM coarse positioning stage is also used in air to align the cantilever with the sample. An optical USB microscope (not shown in the photo) is used as the optical viewfinder. AFM and coarse stage are mounted on a L-shaped metal holder. An active vibration damping system from Halcyonics (Accurion) [53] reduces building vibrations and footfall sound. A balance table and a custom made housing to reduce acoustic noise completes the in air experimental setup. The setup was used for in-situ fragmentation testing of a thin copper film on a polyimide substrate, see Section 4.5.
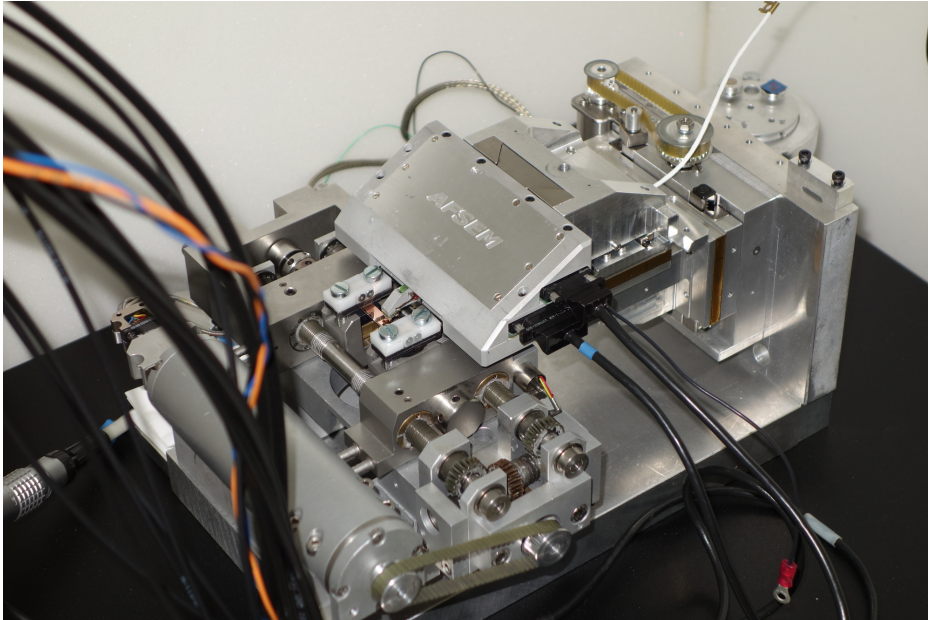

Fig. 2.9.: In air setup including a Kammrath & Weiss straining stage. A thin metal film sample on a polymer substrate is tested.

3. Experimental

In this chapter, sample preparation, characterization methods such as determining the crystal orientation (Section 3.2) and the basic experimental procedure for using the new AFM (Section 3.3) are discussed. Some preliminary remarks dealing with customizing the samples for the combined AFM/SEM instrument are given in Section 3.1.

3.1. Sample requirements for combined AFM/SEM in-situ experiments

After finishing the work to incorporate the new AFM prototype into the micro-mechanical setup in the SEM and being ready for experiments, a second important step needs to be coped with: sample adaption and preparation for the new in-situ AFM/SEM setup. The first section of this chapter will deal with the sample requirements for the new AFM prototype.

3.1.1. Precautions on sample geometry

A typical beginner's mistake during the sample preparation for a standard micro mechanical testing experiment is choosing the wrong dimensions for the features or leaving behind obstacles overlooked during the FIB cutting process. These mistakes often happen when only imaging with the SEM. Figure 3.1 exemplifies the situation by showing a wedge prepared for a micro-compression test. This mistake happens more often than one would think. Possible reasons are underestimating the opening angle of the indenter's cone, which may cause the indenter's side face to touch the neighboring features or other obstacles (Fig. 3.1b). During the FIB cutting obstacles can be overlooked especially on more complicated sample configurations.

For the added AFM scanning, the AFM cantilever needs to have the ability to be approached to the area of interest. Figure 3.2 shows the case for the sample wedge described in Figure 3.1 but from the sideview. Not only can the AFM cantilever hit the sample wedge or other obstacles around the features of interest, indenter and AFM cantilever also may hit each other. Because of this reason, for each experiment shown in Chapter 4, Results, adopted testing configurations were developed, which are introduced in Section 3.2 of this chapter.
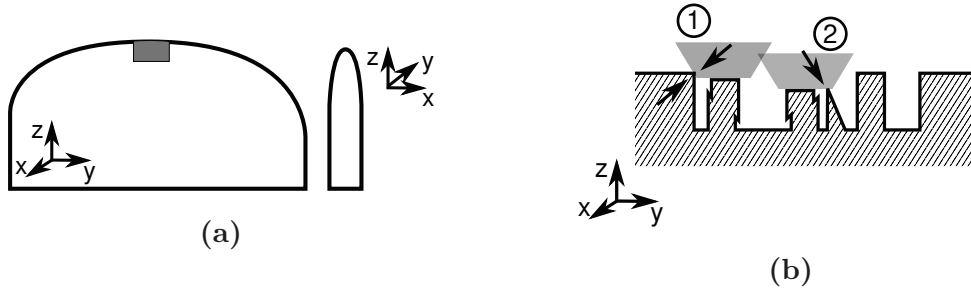
Fig. 3.1.: **(a)** Top- and sideview of an about 1 mm x 1 mm x 150 µm rectangular Cu-plate. The upper edge was thinned by electrochemical etching. Somewhere in the center of the etched area (gray) five to ten testing features are cut using the FIB. **(b)** Detail of the wedge (gray zone in a, topview) with three compression test pillars. At two different positions 1 and 2, the indenter (gray wedge) hits obstacles indicated by arrows during the compression test, which have been overlooked during FIB cutting.
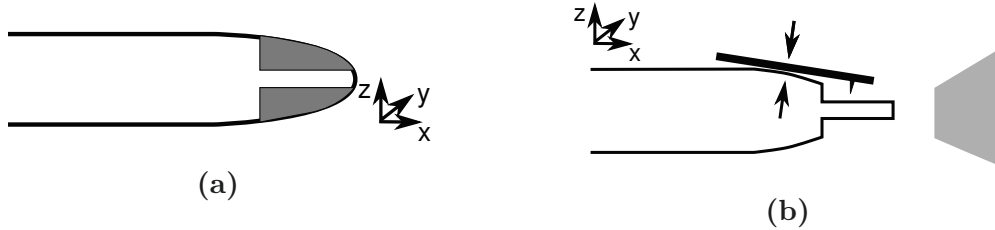
Fig. 3.2.: **(a)** Enlarged side view of the etched sample wedge in Figure 3.1a. The material indicated by the gray areas is removed by FIB cutting. **(b)** The AFM cantilever (black) touches the sample wedge, so that the tip is not able to approach the testing features. On the right side of (b), the compression test indenter (flat punch, gray) is seen.

3.1.2. Physical dimensions of the AFM nose and cantilevers

To prevent an unwanted collision during in-situ testing with the combined AFM/SEM setup, the dimensions and geometry of the AFM nose and the cantilevers need to be known for appropriate sample preparation. Figure 3.3 shows the side view of the AFM nose, the tip of a cantilever and a sample for which the approach of the AFM cantilever would work. For a successful cantilever approach, the angle α at the sample surface shown in Figure 3.3c must not exceed 10° and the distance, d, between the sample surface and the feature surface must not exceed 5 µm.
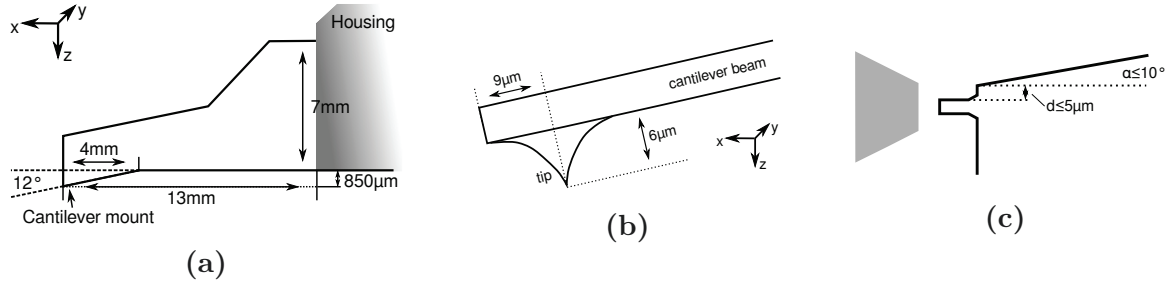
Fig. 3.3.: Dimensions and geometry of the AFM nose and cantilever, the coordinate system is chosen the same way as stated in the AFM software: **(a)** Sideview AFM nose produding out of the housing. The AFM cantilever is not shown. **(b)** Sideview of a type 85x30 µm cantilever. The height of the tip is about 6 µm. **(c)** Geometrical requirements for a compression test pillar on a wedge. The compression test indenter (gray) is indicated on the left side.

All microsamples used in this work have rectangular cross sections. Nonlinear artifacts, for example caused by a scanner bow, are much harder to correct when using round samples, which are quite common in micro-mechanical testing experiments [9]. Details about sample shape and dimensions are given in the according sections later on in this chapter.

3.2. Sample preparation

3.2.1. Brass micro- and nanoindentation bulk samples

The first sample examined by the new in-situ AFM was the surface of a brass single crystal (Copper and 15 wt% Zinc) having micro- and nanoindents on it (Section 4.1). The disk shaped sample (d=1cm, h=4mm) was cut from a single crystal rod. The cut face was mechanically ground and polished. To minimize artifacts from the plastically deformed surface [54, 55, 56], a final step of electrochemical etching was performed. To avoid oxidation of the brass surface taking place in the first few days of being exposed in humid air [57], all experiments (indentation, SEM and AFM imaging) were carried out immediately after sample preparation. Figure 3.4a shows the sample glued on an

AFM holder by silver conductive paste and Figure 3.4b shows the crystallographic planes and directions of the polished surface.

Crystal system and slip

The crystal structure of the Copper (85 wt%) and Zinc (15 wt%) alloy, also called alpha-brass, is a single-phase FCC. The cut face is of type {1 1 1}, which is one of the preferred slip planes. The other three preferred slip planes of the FCC-system cut the sample surface at an angle of 60° (see also Section 1.2). Slip lines close to an indent are exemplified in the right area of Figure 3.4b, showing an indentation imprint at the top and a slip pattern below. The pattern of the slip lines can be used to identify the orientation of the surface plane [58]. In this work, this method was used whenever possible to avoid the more elaborate procedure of EBSD [59] scanning.

(a)   (b)

Fig. 3.4.: (a) Brass single crystal with electropolished surface glued on an AFM holder. **(b)** Sketch of (a) showing the crystallographic planes and directions of the {1 1 1} surface. A segment was cut away at the bottom along a <110> direction. Right area: Highly magnified sketch of an indent (top) plus a typical slip line pattern caused by the plastic deformation. The slip lines, also indicating <110> directions, are exemplified just below the indent.

Determining the lattice constants

To determine the lattice constants of the brass sample a Rigaku Smartlab [60] X-ray diffractometer (XRD) equipped with a thin film attachment goniometer, a sealed tube XRD source and a 1D-detector was used in Bragg–Brentano $\theta - 2\theta$ configuration [61] and [62]. By knowing the samples surface orientation of {1 1 1}, the according peak for the $d_{\{111\}}$ lattice parameter was determined applying Braggs law

$$d = \frac{\lambda}{2\sin\theta},$$ (3.1)

where λ is the wavelength of the X-rays, and d, gives the distance between the lattice planes. For a cubic crystal system the lattice constant a_0 is given by [63]

$$a_0 = d_{hkl}\sqrt{h^2 + k^2 + l^2}.$$ (3.2)

26

From this information the Burgers vector was determined to be

$$\vec{b} = \frac{a_0}{2} \begin{pmatrix} 1 \\ 1 \\ 0 \end{pmatrix}.$$

Copper (85 wt%) and Zinc (15 wt%) Brass is a substitutional alloy. The lattice constants are expected to be close to that of Copper. The diffraction angle 2θ of the Cu-$\{1\,1\,1\}$ planes is 43.318°, giving for a_0 a value of $3.62\,\mathring{A}$ [64, p. 144]. Further details about plasticity and slip in metals are discussed in Chapter 1, Section 1.2 is about the details in FCC crystal systems.

Micro- and nanoindentation: Experimental details

Two different indenters were used for the load ranges $1\,\mathrm{N}$ to $5\,\mathrm{N}$ and $50\,\mathrm{\mu N}$ to $10\,\mathrm{mN}$. For the higher load range a Buehler Micromet 5104 micro-indentation hardness tester with a Vickers pyramid indenter tip and for the lower range a Hysitron TriboScope nanoindenter with a Berkovich 3-sided pyramid indenter, mounted on a Veeco Dimension 3100 AFM were employed. To prevent an overlap of the plastic zones of the single indents, the distance between the indents was chosen to be at least three times higher than the plastic zone diameter [65], [66] and [67]. In the case of the nanoindents, the values for the distances correspond to $25\,\mathrm{\mu m}$–$30\,\mathrm{\mu m}$. Table 3.1 shows a list of the indents made into the prepared brass surface. The type of instrument, the preset load and if the indention was plastic, leaving a permanent imprint on the surface, or elastic are listed.

Indenter	Load	plastic/elastic	Indenter	Load	elastic/plastic
Buehler	5 N	plastic	Hysitron	4 mN	plastic
Buehler	3 N	plastic	Hysitron	3 mN	plastic
Buehler	1 N	plastic	Hysitron	2 mN	plastic
Hysitron	10 mN	plastic	Hysitron	1 mN	plastic
Hysitron	9 mN	plastic	Hysitron	0.75 mN	plastic
Hysitron	8 mN	plastic	Hysitron	0.5 mN	plastic
Hysitron	7 mN	plastic	Hysitron	0.25 mN	elastic
Hysitron	6 mN	plastic	Hysitron	0.1 mN	elastic
Hysitron	5 mN	plastic	Hysitron	0.05 mN	elastic

Table 3.1.: List of performed indents on the surface of the brass single crystal. The three lowest loads showed pure elastic behavior where no permanent imprints were created on the surface.

Radius of the indenter tip

Especially at low loads, the indenter tip rounding has a strong influence on the results of the indentation experiment. The rounding of the tip was estimated by fitting a

Hertzian elastic contact solution (Equation 3.3) to the elastic indentation data on fused quartz (fused silica) [68, pp. 16]. The load P as a function of the displacement δ is

$$P = \frac{4}{3} E_r \sqrt{R} \delta^{\frac{3}{2}} \tag{3.3}$$

where R is the radius of the indenter tip, and E_r the reduced elastic modulus (69 GPa for fused silica). Figure 3.5 shows the according load-displacement data and the elastic contact solutions. Three different indents with loads of 0.75 mN, 1.0 mN and 2.0 mN have been evaluated giving an average value of 749 nm for the radius of the tip. The results are summed up in Table 3.2.
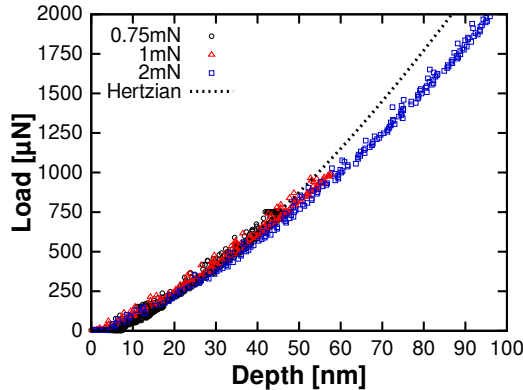
Fig. 3.5.: Elastic indentation data of fused silica fit to a Hertzian solution to estimate the indenter tip rounding.

Maximum load	Radius indenter tip
0.75 mN	725 nm
1.0 mN	827 nm
2.0 mN	696 nm
average	749 nm

Table 3.2.: Results of Hertzian solutions for estimating the tip rounding of the nanoindenter tip. Loads and radii, and the average of the three individual values are listed.

3.2.2. Indents@edge method

In Section 4.2, a new micro-mechanical testing method, the "indents@edge"-method, is discussed. This new kind of experiment was developed to investigate plasticity in a geometrically or dimensionally constrained volume. Plasticity in constrained volumes also was discussed by others, such as Gerberich [69] or Soifer [70].

In the "indents@edge"-method, the lateral face of a cuboid shaped sample is indented at the edge close to the top surface (Figure 3.6a). Due to plastic deformation,

dislocations are nucleated and depending on the depth of the indent, emitted to the surface [67, 71]. The resulting slip steps at the top surface are recorded by the SEM and the AFM.

(a)   **(b)**

Fig. 3.6.: Indents@Edge method: (a) Sketch of the experimental setup to perform an experiment, showing the sample with a {1 1 1} top surface, the AFM cantilever (top, left) and the indenter tip of the Hysitron PI85 SEM picoindenter (upper right side). (b) sample configuration for ion polishing the top surface to remove the plastically deformed layer and for imaging.
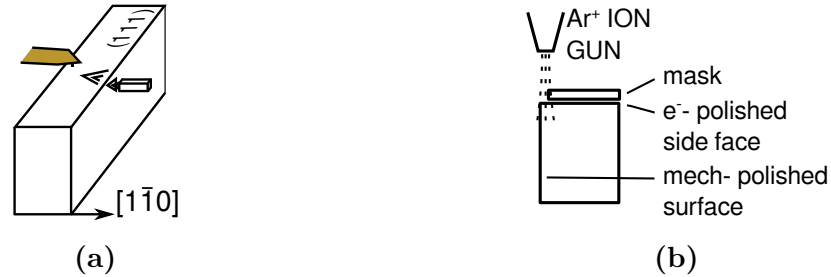
The indentation is performed by the Hysitron PI85 SEM picoindenter [51] with a sharp cube corner tip. The separate sample stage of the picoindenter allows an accurate positioning of the sample relative to the indenter tip in steps of several tens of nanometers. After placing the indenter tip 500 nm to a few microns beyond the {1 1 1} sample surface, indents with loads in the range of 0.5 mN to 10 mN are employed.

Sample preparation

The most challenging step of this otherwise quite straight forward method with high potential to investigate small scale plasticity events in various sample configurations is preparing a well defined 90° shaped edge without modifying the crystalline structure at the edge. Electropolishing both faces of the edge leads to rounding of the corner and is therefore not possible. To overcome these issues, two methods, electropolishing (Struers LectroPol-5) and ion polishing (Hitachi E-3500 ion milling system) were combined.

After grinding and mechanically polishing both surfaces, the side face of the segment of the disk shaped sample was electropolished, protected by a mask and ion polished by positioning the mask and electropolished surface towards the ion gun (Figure 3.6b). The Ar$^+$-ions are only polishing the mechanically treated top surface of the sample. The result is a well defined 90° edge having the plastically deformed surface layers on both adjacent sides removed (Figure 3.7). The size of the area available for indenting is about 0.25 mm^2 to 0.5 mm^2. The shape of the polished section is governed by the shape of the Ar$^+$-beam which is Gaussian.

Fig. 3.7.: Brass single crystal mounted on a sample holder compatible with the Hysitron PI85 SEM PicoIndenter. (a) Overview, black frame: ion polished cross-section (b) Detail showing the small, Gaussian shaped area polished with ions. The size of the polished area is about 0.5 mm^2.

3.2.3. Microbeams and -pillars

Two different methods have been applied for fabricating the microbeams and micropillars used for the micro-mechanical experiments described in Section 4.4. In both cases a 1 mm x 1 mm x 150 µm sized Cu plate was cut out of a single crystalline rod and thinned at one edge by electrochemical etching for faster FIB processing, following the approach of Moser et al. [72]. The microbeam samples were prepared with a Zeiss LEO 1540XB dual-beam FIB workstation. The acceleration voltage of the FIB source's Ga$^+$ ions was 30 kV. The currents used range from 5 nA down to 100 pA for coarse to fine milling, respectively. The main difference of the different methods is the orientation of the Cu wedge, which effects the FIB machining of the testing features. The two methods are separately described in the following subsections.

Microbending beam preparation

For the bending beam samples, the Cu wedge points towards the SEM gun and the AFM cantilever, the indenter is orthogonal to the surface of the Cu plate. The geometry of the bending beams were chosen as described by Kirchlechner et al. [73]. A schematic of the bending beam samples is shown in Figure 3.8b. The method for sample preparation was slightly modified to fit the needs for AFM imaging on top of a wedge. The details are discussed in Section 3.1.2, see also Figure 3.8.

The top surface of the bending beam corresponds to a $\{1\,1\,1\}$ crystal plane and the axis of the bending beam to a $\langle 1\,\bar{1}\,0 \rangle$ crystal direction as described by Motz et al. in [38]. The $\langle 1\,1\,\bar{2} \rangle$ is a gliding direction of a partial dislocation in the FCC system caused by the ABC-stacking sequence of the $\{1\,1\,1\}$-planes [3, pp. 85]. Details about the shape of the bending beams and the crystal directions are shown in Figure 3.8b.

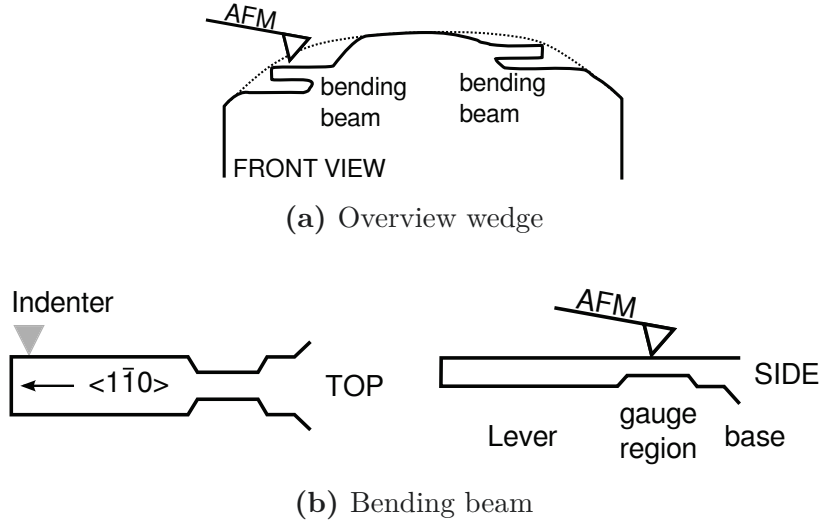**(a)** Overview wedge

(b) Bending beam

Fig. 3.8.: Overview **(a)** and details **(b)** of the sample preparation of bending beams. The dotted line denotes the original wedge before FIB cutting. The Cu wedge is pointing to the SEM gun and the AFM cantilever.

Table 3.3 contains the prepared microsamples used to investigate plasticity at the micron scale in Cu single crystals. The type of micro-mechanical testing experiment, the number of samples prepared and the sample dimensions (overall and gauge length) are listed.

Type	Quantity	Overall Dimensions [µm]	Gauge length [µm]
Bending test	6	4x5x20	5

Table 3.3.: List of bending test samples to investigate plasticity at the micron scale.

Microcompression pillar preparation

Microcompression pillars have been prepared to investigate the deformation behavior of constrained volumes containing a large-angle grain boundary (LAGB) by additionally using the in-situ AFM. The original idea for this kind of experiments was expressed by Ng et al. [74] and later discussed by Imrich et al. [75]. Compared to the method of preparing microbending beams, the surface of the Cu wedge now points to the SEM gun and the AFM cantilever. The wedge faces towards the indenter. Details are seen in Figure 3.9. In this configuration, more undercutting of the wedge is needed, allowing indenter and bending beam to have enough room to move.

Table 3.4 contains the prepared microsamples to investigate dislocation gliding at LAGBs. The type of micro-mechanical testing experiment, the number of samples
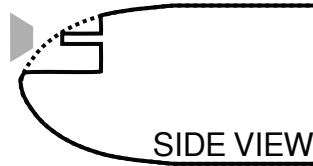
SIDE VIEW

Fig. 3.9.: Overview of the microcompression pillar sample preparation. The dotted line denotes the original wedge before FIB cutting. Compared to the microbending beam preparation method, much more material needs to be removed by the FIB with this method. Already during the coarse FIB cutting, extra care needs to be taken to make sure that both, the indenter (gray, upper left) and the AFM cantilever, are able to reach the sample.

prepared, the number of grain boundaries (GB) in the volume of the sample and the sample dimensions are listed.

Type	Quantity	GB	Dimensions [µm]
Compression	17	0	2x2x6
Compression	4	1	2x2x6

Table 3.4.: Table with microsamples to investigate dislocation gliding at LAGBs. Column three contains the number of grain boundaries (GB) found in the tested volume.

3.3. Processing AFM experiments in SEM

In this section the main points of processing an AFM experiment inside of the Zeiss Leo 982 SEM are discussed. Detailed step by step instructions starting with mounting the AFM inside of the SEM chamber up to tip approach are found in Appendix B and Appendix C.

3.3.1. Precautions before approaching the AFM cantilever to the sample

When closing the SEM chamber with the AFM mounted, wrong stage positions of the SEM stage or the coarse AFM stage may lead to a crash of the AFM and the SEM pole piece. To avoid this, the instructions in Appendix B should be carefully followed. It is particularly important to have the z-position of the SEM stage at the highest working distance. For the Zeiss Leo 982 this means the display for the z-position of the stage must show zero.

After connecting all cables and before turning on the high voltage unit, the system needs to be checked to prevent electrical damage. This is done by watching the signals

of the AFM cantilever in tapping mode using the AFM controller software. After turning on the AFM computer and controller, the AFM cantilever has to show a reasonable amplitude signal when sweeping through the excitation frequencies. If this is not the case, the cantilever is propably not working or the cables are connected wrong. After making sure that everything is working properly, the high-voltage amplifier can be turned on and the SEM chamber is ready for pumping. When the SEM is ready for imaging, the cantilever can be approached to the sample surface.

3.3.2. AFM cantilever approach

Before starting the cantilever approach, the gains of the feedback loop should be set to $k_i = 250$ and $k_p = 500$. It should be made sure that the high voltage unit is turned on. In tapping mode, the amplitude of the AFM cantilever should not exceed 100 nm, this corresponds to a excitation voltage of the tapping piezo of about 0.05 V to 0.3 V. The setpoint should be at a quite low values around 90% to 95%, to keep the interaction force between AFM tip and sample surface as small as possible. After approach, the total distance of the tip interacting with the surface should not exceed 15 nm. Finding the right setpoint varies from cantilever to cantilever and requires practice to gain experience with the instrument and the cantilevers used. The setpoint needs to be adjusted again after a successful cantilever approach. Cantilever approach in vacuum is not comparable to an approach in air because the air damping considerably changes when the AFM cantilever gets closer to the surface. Also long-range van der Waals interactions caused by an H_2O surface layer indicate an imminent contact between the tip and the surface. Both indicating mechanisms are missing in vacuum, that is why the onset of the AFM cantilever at the surface occurs quite spontaneously.

After the sample and the AFM cantilever are coarsely aligned to the SEM's electron beam, the working distance relative to the cantilever is decreased to 10 mm by moving the SEM stage in the z-direction. At a magnification of 500x, sample and cantilever are aligned to the SEM electron beam again, the system is ready for cantilever approach (Figure 3.10). Because of the risk of surface contamination from the electron-beam, the approach should take place away from the area of interest.

As a next step the focus of the SEM's electron beam is changed from the AFM cantilever to the sample surface using the SEM focus wheel. The number of clicks needs to be counted. One click of the focus wheel corresponds to approximately 50 steps with the AFM's coarse stage z-motor. A single step of the z-motor corresponds to about 0.35 µm in step height.

It is strongly recommended not to approach the AFM cantilever in a continuous movement. After each 1000 steps of the coarse AFM stage, the distance should be measured by focusing the SEM beam on the sample surface and the AFM cantilever again. The last 500 to 1000 steps should be done by the auto approach option implemented in the AFM software. Depending on the gains of the feedback system of the AFM, one auto approach cycle takes about 2 seconds. During one auto approach cycle, the AFM's coarse stage does 10 steps. The number of steps depends on the type of AFM nose used. The coarse motor of the AFM should move about 40% of the

(a) Cantilever in focus.   **(b)** Surface in focus.
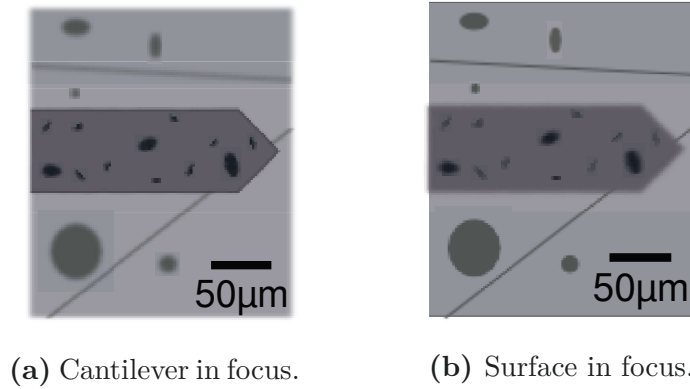
Fig. 3.10.: AFM cantilever before sample approach. The distance between surface and cantilever is measured by counting the clicks of the Focus wheel during changing focus from AFM cantilever (a) to sample surface (b). One click of the focus wheel corresponds to 50 steps of the AFM's coarse z-motor.

total swing of the nose's z-piezo. The auto approach in vacuum is rather slow.

After approach, the working distance of the SEM again can be decreased to a final value of about 8 mm. After finishing the experiments, the working distance of the SEM should be increased first. Retracting the AFM without lowering the z-stage of the SEM potentially leads to a crash with the SEM gun!

4. Results

Within this chapter the experimental results obtained by the new AFM/SEM instrument are presented. Four different scenarios and their benefits to study plastic deformation are exemplified. Its capabilities for use in the SEM for combined AFM and SEM imaging and the compatibility with micro-mechanical testing devices for in-situ experiments inside of the SEM chamber in vacuum are demonstrated as well as experiments in air are shown. To show the performance in air, the plastic deformation of thin films during mechanical straining was investigated.

4.1. Combined AFM and SEM imaging of micro- and nanoindents

4.1.1. Slip step analysis close to micro-indents

The surface of single crystalline brass (85 wt% Cu, 15 wt% Zn) was indented with loads varying from 500 μN to 500 mN, using two different types of indenters. For the load range 500 μN - 10 mN a nanoindenter with a Berkovich tip and for the range 100 mN - 500 mN a microhardness tester with a Vickers pyramid indenter tip was used. For a detailed description of the sample and the surface preparation see Section 3.2.1.

Imaging

The new combined AFM/SEM instrument can be used in air and in vacuum. To find the area of interest for experiments in air, an optical USB microscope is used[1]. Figure 4.1 shows the same indent imaged with the optical light microscope and the SEM. In order to find the exact same spot with the AFM in air and in vacuum by using two different kinds of microscopes, an indent with a high load of 300 mN surrounded by a distinct plastic zone, was chosen.

Figure 4.2 shows the corresponding 2D and 3D images of the AFM scans at the positions shown in Figure 4.1. Both scans were made in tapping mode. The AFM parameters like gains, scan speeds and excitation voltage for the tapping amplitude of the cantilever have been adopted to the different cantilever's damping in air and in vacuum. For comparison, see the AFM scanning parameters listed in Table 4.1.

The original AFM height scans with a size of 30 μm x 30 μm were cropped to 18 μm edge length to show exactly the same region for both environments (air and vacuum)

---

[1]Further details in Section 2.3.2, "Stand-alone in air operation of the AFM".
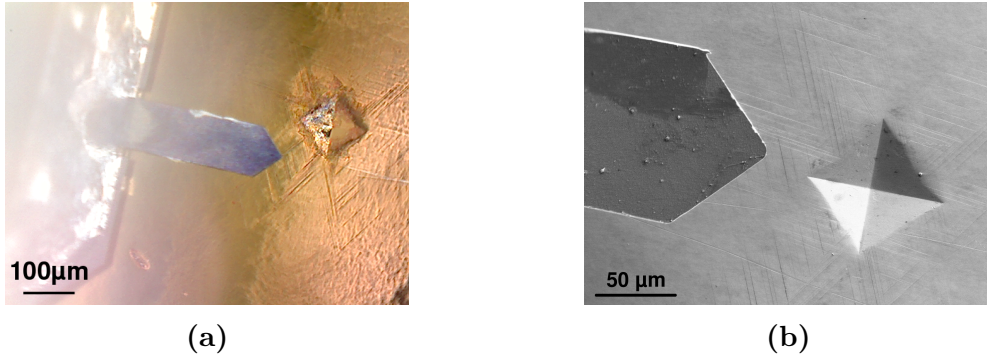
(a)

(b)

Fig. 4.1.: Micro-indent (indentation load 300 mN) on a single crystalline brass surface with AFM cantilever visible on the left side of both images: **(a)** Optical microscope 100x **(b)** SEM 150x. The resolution for both microscopes is sufficient to display the slip steps around the indent, which made repeatedly finding the same spot for AFM imaging in air and in vacuum possible.

Environment	Scan size	Lines	Scan speed	Excitation	k_i	k_p
Air	30 µm x 30 µm	512	$1.5\,\mathrm{s}^{-1}$	0.7 V	60000	100000
Vacuum	30 µm x 30 µm	512	$1\,\mathrm{s}^{-1}$	0.1 V	20000	40000

Table 4.1.: AFM scanning parameters for the scans shown in Figure 4.2. The different environments (air and vacuum) require different settings for the gains, scanning speeds and excitation voltages of the tapping piezo.

and to remove some nonlinear distortions[1] close to the borders of the original scan. After cropping, the tilt was corrected by a mean plane subtraction. Because the sample surface is tilted, caused by the plastic deformation close to the indent, as a second step another plane was subtracted by specifying three points on the triangular shaped upper left section of the surface. No further image correction was applied, all steps were performed using the data analysis tool Gwyddion [77], [78].

The two AFM scans of Figure 4.2 agree very well. The in vacuum image looks slightly unsharp than the in air image. This could have been caused by setting the feedback parameters too low for the in vacuum experiment. To compare the results quantitatively, 1D profiles have been extracted at approximately the same position on each AFM image, see Figure 4.3.

The same methods of 2D tilt correction were applied for the in air and in vacuum scans. Nevertheless, the overall slope of the 1D profiles in Figure 4.3 did not perfectly match each other. A line having a steepness of k=10 nm/µm was subtracted from the

---

[1]At the time of the experiments, only a static 3rd order time independent correction method was implemented by the AFM software [76] to correct the scanner piezos nonlinear electromechanical response of the open-loop AFM.

(a)

(b)

AIR

VACUUM

(c)

(d)
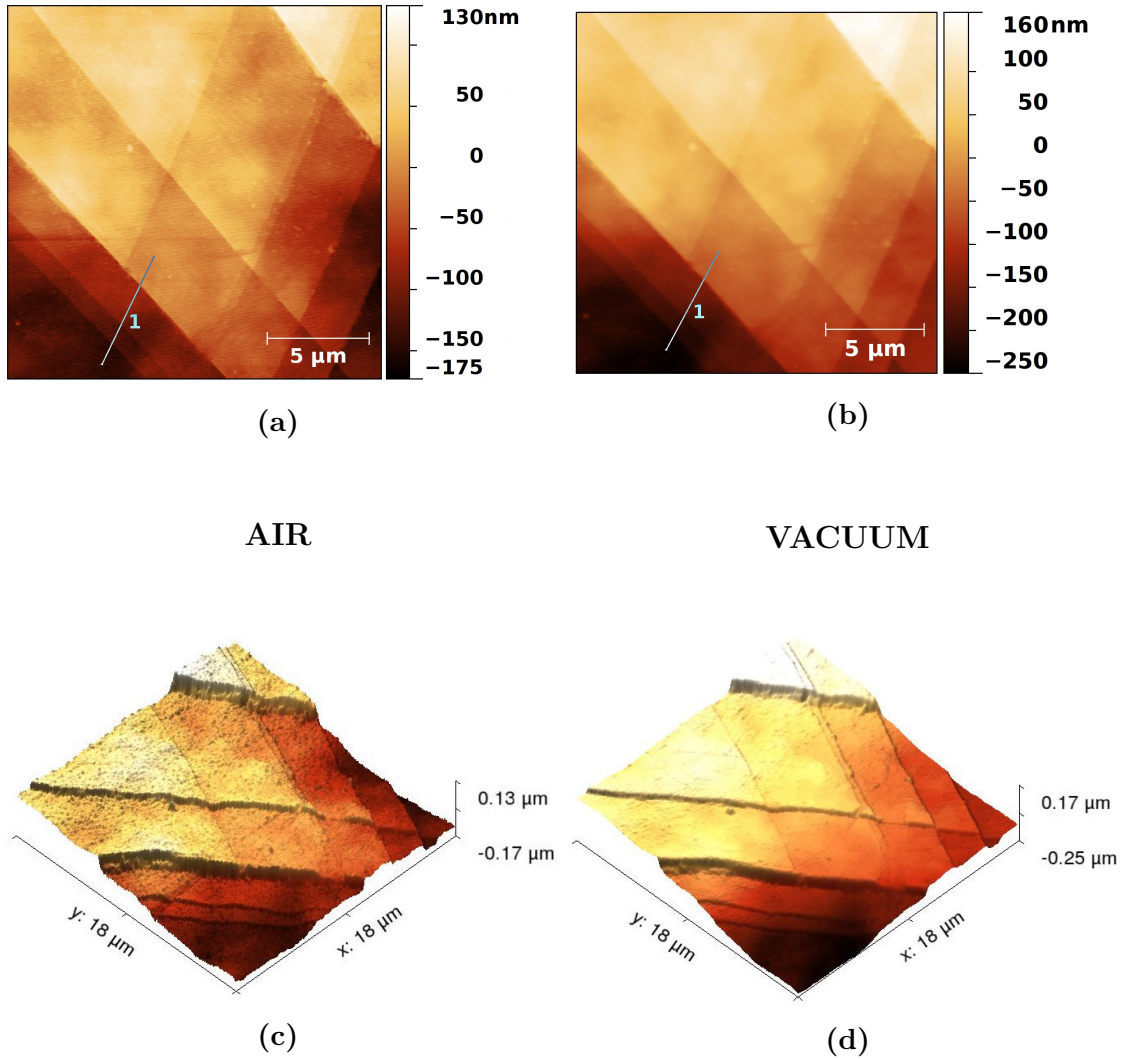
Fig. 4.2.: AFM height images of an 18 µm x 18 µm sized area close to the indent shown in Figure 4.1. 2D scan **(a)** in air and **(b)** in vacuum. Line profiles (blue lines indicated with 1) have been extracted at approximately the same position on each image. 3D images of the **(c)** in air scan and **(d)** in vacuum scan illustrate the good agreement of the two experiments. No image corrections other than cropping and plane subtractions have been performed.

	Vertical [nm]	Lateral [nm]
Air	72.5	227
Vacuum	74.4	172

Table 4.2.: Comparison of the horizontal and vertical distances.

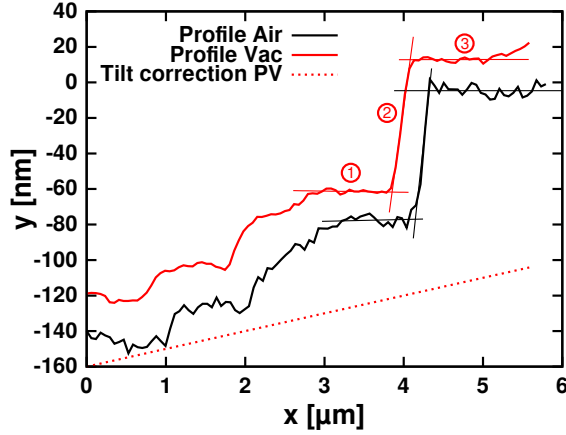**Fig. 4.3.:** 1D profiles, extracted along the lines shown in Figure 4.2a and 4.2b. On both profiles three sections close to the investigated slip step have been approximated by a linear fit (red numbers 1-3). The resulting vertical heights of the slip steps in air (72.5 nm) and vacuum (74.4 nm) show perfect agreement. The error in the lateral distances is caused by the high steepness of the slip step connected with a relative low lateral resolution of 58 nm/pixel of the scan.

vacuum profile to correct for the remaining tilt missfit. The vertical and horizontal distances of the slip step were determined for both profiles by fitting three lines in the sections before (1), within (2) and after (3) the step (Figure 4.3). The vertical distance was measured in the center of the step, the horizontal by subtracting the x-coordinates of the intersections of line 2+3 and 1+2, respectively. The fitting range for linear regression was chosen at the flat areas close to the slip step by assuming the steepness of the surface is about the same on both sides of the step. That means, lines 1 and 3 should be parallel.

Contrary to the horizontal data the vertical distances agree very well. The error in horizontal direction is caused by the relative low lateral resolution of only 58 nm/pixel. A tip sample-dilation artifact [79] (also called a tip sample-convolution [80, pp. 111]) should show the same effect on both profiles and therefore not cause any difference. The data for all dimensions is listed in Table 4.2.

Quantitative analysis

To determine the number of dislocations emitted to the surface by measuring the height of the according slip step, the distance along the activated slip systems[1] needs to be known. In case of the brass sample $\{1\,1\,1\}$ surface, it does not correspond to the vertical distance (See Figure 1.4, section 1.2) of the slip step as measured by the AFM, shown in Figure 4.3. The average value of the slip steps' vertical height listed in Table 4.2 is 73.5 nm. Projecting this value along the direction of the active slip

---

[1]Meaning one of the available twelve $\{1\,1\,1\}\langle 1\,1\,0\rangle$ slip systems in FCC crystal systems.

system according to Equation 1.7 gives 90 nm. To know the number of dislocations emitted, the spacing of the {1 0 0} planes of the FCC crystal have been determined by diffraction of X-rays. The lattice constants were determined by using a Rigaku XRD instrument described in Section 3.2.1. As the orientation of the sample surface was already known to be a {1 1 1} (also discussed in Section 3.2.1) and assuming that the according spacing between the {1 1 1}-planes should be close to the {1 1 1} peak of Cu, finding the corresponding peak in the brass sample was quite straight forward. Figure 4.4 shows the experimental data approximated by a Gauss distribution.
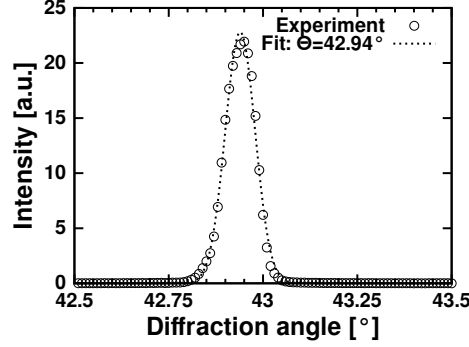

Fig. 4.4.: {1 1 1} peak at a 2θ value of $42.94°$. A Gauss distribution was fit to the data, a Voigt profile also was used giving the same result.

Applying Bragg's law

$$d = \frac{\lambda}{2\sin(\theta)} = \frac{1.5406}{2\sin(21.47)} = 2.105 \mathring{A} \tag{4.1}$$

where d is the perpendicular distance of the lattice planes and λ is the wavelength of the X-rays, $d_{\{111\}} = 2.105 \mathring{A}$ is determined. Knowing $d_{\{111\}}$ leads to the lattice constant, a_0 of the FCC crystal system by projecting the length to the $\langle 1\,0\,0 \rangle$-direction:

$$a = \frac{2.105\sqrt{3}}{\begin{pmatrix}1\\1\\1\end{pmatrix} \cdot \begin{pmatrix}1\\0\\0\end{pmatrix}} = 3.65 \mathring{A} \tag{4.2}$$

The number, n, of emitted dislocations is estimated by dividing the length along the contributing slip system by the length of the Burgers vector $|\vec{b}| = a/2 \cdot |\langle 1\,1\,0 \rangle| = a/\sqrt{2}$ of the FCC crystal's perfect dislocation:

$$n = \frac{\sqrt{3/2}h_v}{a/\sqrt{2}} = \frac{\sqrt{3} \cdot 735}{3.65} \approx 349 \tag{4.3}$$

The value means that 349 dislocations contributed to generate the slip step shown in

Figure 4.2a and 4.2b. A systematic error for the vertical step height h_v caused by a tip sample-dilation was eliminated using best-fit lines at the edges of the slip step. The misalignment of the direction of the vertical step height h_v and the direction of the active slip system in the FCC crystal was taken into account.

A more detailed investigation of the plastic deformation around indents by using the in-situ AFM in SEM was performed by examining smaller indents, having a plastic zone smaller than the maximum available scan size of the AFM scanner. The scans could be used to measure the plastic zone size. By additionally knowing the indentation load, the yield strength of the investigated material can be calculated [81]. The details are described in the next section.

4.1.2. Imaging plastic zones of nanoindents

Three of the nanoindents listed in Table 3.1, on page 27 with loads of $0.5\,\mathrm{mN}$, $5\,\mathrm{mN}$ and $10\,\mathrm{mN}$ are shown for further in depth investigation. The plastic zone surrounding the indents were small enough to be imaged within a single AFM scan. SEM and AFM images, load-displacement curves of the indents and an analysis of the plastic zones and slip steps will be presented in the following.

SEM images of the three representative indents with the loads of $0.5\,\mathrm{mN}$, $5\,\mathrm{mN}$ and $10\,\mathrm{mN}$ are shown in Figure 4.5. All images were taken using the SEM parameters summarized in Table 4.3. For the indents with loads of $5\,\mathrm{mN}$ and $10\,\mathrm{mN}$ the surrounding slip lines reveal the plastic zone around the indents. The indent with the load of $0.5\,\mathrm{mN}$ only showed slip lines inside of the imprint. The lateral dimensions of the $0.5\,\mathrm{mN}$ imprint are in the range of a few hundred nanometers. It is almost impossible to find the imprint by an optical microscope, because these values are close to the theoretical resolution limit found by Abbe [11, pp. 246]. To be able to find all of the imprints and to get a more detailed information about them, the combined AFM/SEM is required.

Parameter	Value
Detector	In lens
Working distance	$4.5\,\mathrm{mm}$
Acceleration voltage	$3\,\mathrm{kV}$
Aperture	$30\,\mathrm{\mu m}$
Magnification	$10\,\mathrm{kX} - 30\,\mathrm{kX}$

Table 4.3.: SEM parameters for imaging the nanoindents.

Some of the slip lines in Figure 4.5c are indicated by drawing lines over them. The slip lines appear almost parallel to the boundaries of the indenter imprint, however this is only a coincidence. Slip occurres on preferred crystal directions, as described in Section 1.2.

To prevent contamination artifacts caused by the SEM electron beam, the SEM scans during the positioning of the AFM cantilever were kept as short as possible
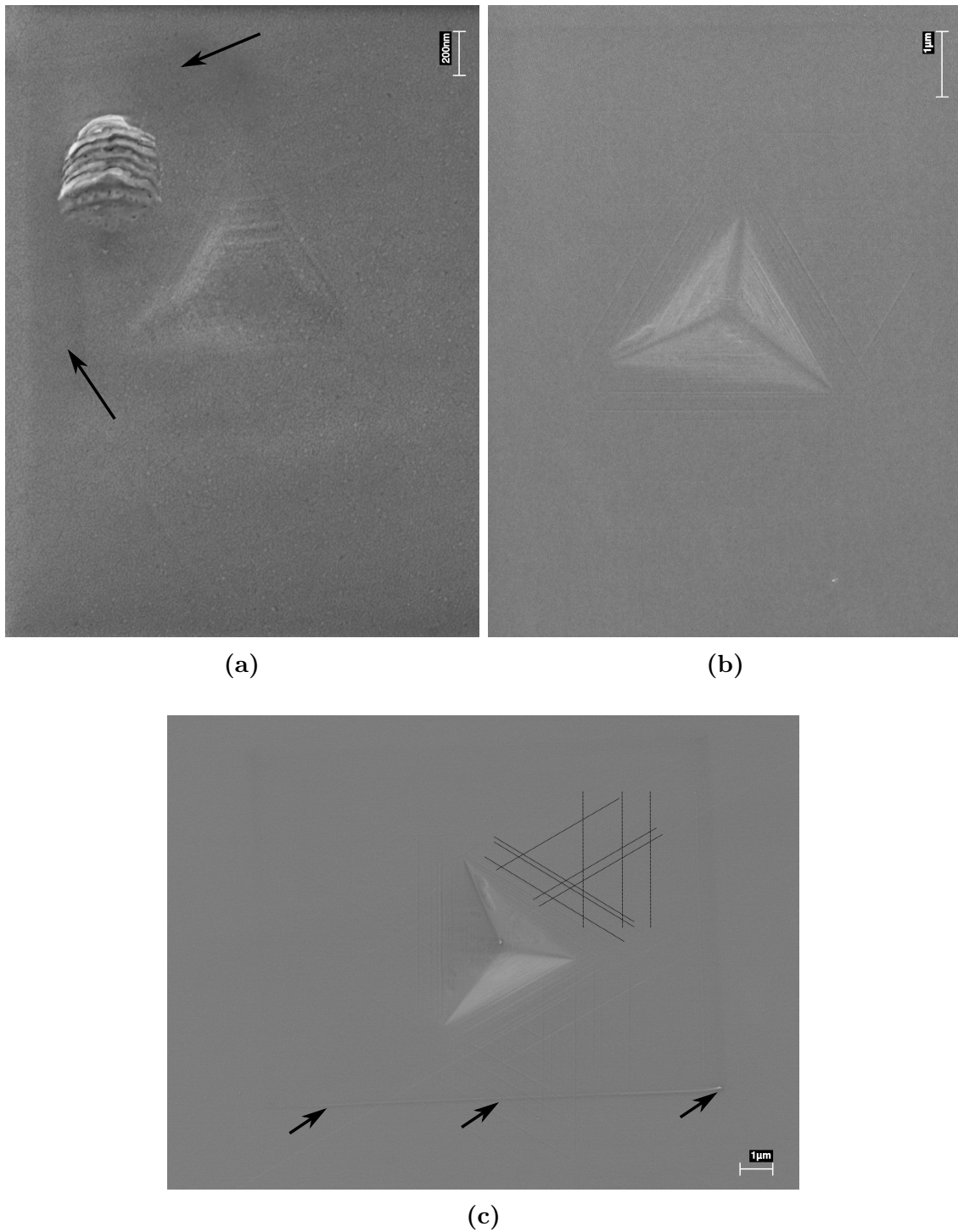
(a)

(b)

(c)

Fig. 4.5.: SEM images of three indents with loads of **(a)** 0.5 mN, **(b)** 5 mN and **(c)** 10 mN. For optimal use of space, (a) and (b) are turned by 90°. Contrary to (a), slip steps are visible around the indents in (b) and (c). (a) shows a distinct line-shaped structure inside of the indent, the lines are parallel to the slip-lines visible in (b). Contamination artifacts are indicated by arrows. Some slip lines in (c) are highlighted by drawing dark lines over them.

and performed at high scanning speeds. Nevertheless, typical rectangular shaped redeposition artifacts can be viewed as dark areas in Figure 4.5a and as bright lines Figure 4.5c. To reduce the electron detector noise, SEM high quality images are taken with low scan speeds. Because of the risk of higher contamination, the high quality SEM images were taken after the AFM scans.

Without tilting the sample, which would need further image processing to correct for image distortion or the help of more sophisticated methods like stereophotogrammetry [82], [83, pp. 207] it is difficult to make the slip steps visible with the SEM. No topographical information like the height of the slip steps or inclination of the surfaces around the indent is ascertainable. The AFM scans having about the same scan area as the SEM images shown in the next section will provide the appropriate information.

AFM scanning parameters and images

All three indents shown in Figure 4.5 also have been investigated by the AFM in vacuum. The scan size was chosen to include the indents and the visible surrounding plastic zones. The basic data of the scans is provided in Table 4.4, Figure 4.6 shows the according 2D height scans.

Indent load	Max. height	Scan size	Lines	Scan speed	k_i	k_p
0.5 mN	90 nm	2.5 µm	512	$0.3 \, \text{s}^{-1}$	500	1000
5.0 mN	350 nm	15 µm	512	$0.3 \, \text{s}^{-1}$	2000	20000
10.0 mN	500 nm	20 µm	512	$0.3 \, \text{s}^{-1}$	1000	4000

Table 4.4.: AFM scanning parameters for imaging the nanoindents.

All images were flattened by consecutively subtracting a mean plane and a plane specified by three arbitrary points, which were believed to be at the same height level. Finally, a median difference line correction was applied. This additional step became mandatory, because the total height difference is much smaller compared to the AFM data of the micro-indents. Before executing the line correction, the indents including the surrounding features were carefully masked out to avoid introducing artifacts [84, 85]. All steps were performed using the data visualization and analysis tool Gwyddion [77], [78].

Qualitatively, the SEM and AFM imaging method show the same results. The indent with the lowest load does not show any evidence of plastic deformation around the imprint. With increasing indentation loads, slip patterns start to evolve and become more pronounced and larger. SEM redeposition artifacts, caused by looking at the imprint during cantilever positioning are also clearly seen with the AFM. The contamination is not just a chemical alteration of the surface but a real deposition of material leading to a detectable change of the surface topography with the AFM. Some linear shaped contamination artifacts are denoted by arrows in Figure 4.6b.

In all three images, the color scale of the AFM data was chosen to reveal only the topographical data around the indent, which corresponds, or at least is quite close
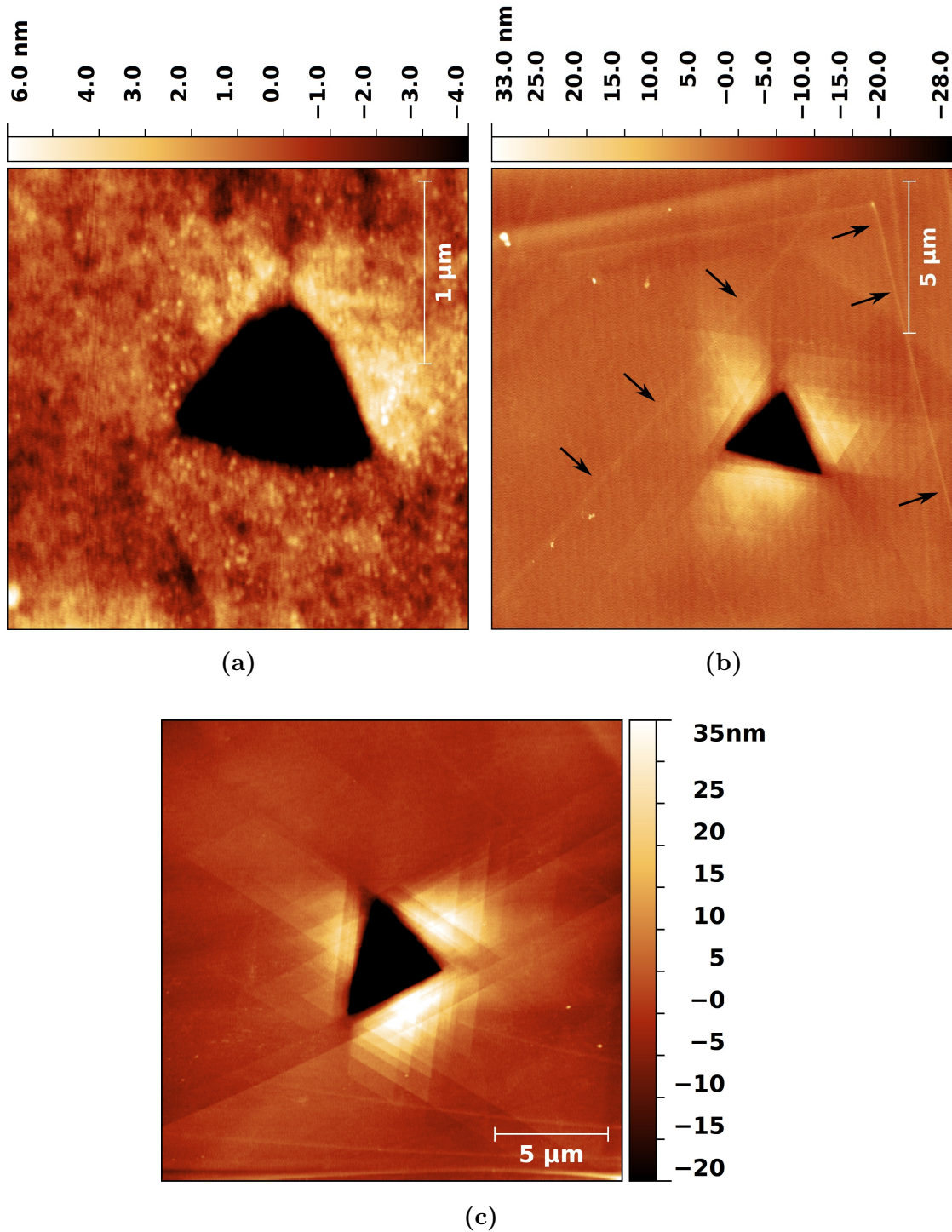
Fig. 4.6.: AFM images of three indents with loads of **(a)** 0.5 mN, **(b)** 5 mN and **(c)** 10 mN. For optimal use of space, (a) and (b) are turned by 90°. Qualitatively the same results as obtained by the SEM images (Figure 4.5) are observed with the AFM. However, the formation of pile-ups is more easily detected and distinguished from sink-in (characteristics of the investigated material) and a quantitative analysis of the topographical data like the step heights is available. Some linear shaped contamination artifacts caused by the SEM electron beam are denoted by arrows in (b).

to the median of the AFM z-topography data. By adjusting the color scale in this quite narrow range, the information of the topography inside of the indent is lost. The indenter imprint can only be seen as a dark triangular shaped area. A detailed analysis of the surface by extracting 1D cross-sections to estimate the height of the slip steps and therefore the number of emitted dislocations is discussed later.

A color scale providing the complete picture of an entire scan's topography cannot be found in the case of the indents shown here. The ratio of the maximum height difference in topography which is a few hundred nanometers compared to the size of the features of interest (single nanometers) is too high to be resolveable. Nevertheless, the 3D images shown in Figure 4.7 can qualitatively provide an overview.

The information given by the 3D images calculated from the AFM data is compareable to the SEM data, which (even more for chemically homogeneous materials) give a pseudo 3D-view of the surface's topography. While the topography information inside of the indents imprints were lost in the 2D view in Figure 4.6 it can be clearly seen in the 3D images.

Analysis of the load-displacement data

Figure 4.8 shows the load-displacement curves of the nanoindents, recorded by the Hysitron controller software. All loading curves show pop-in events [86, 87] at loads in the range of 400 µN to 800 µN. When a pop-in is present in the load-displacement curve a single crystalline material, it indicates that a dislocation avalanche was activated. For the 0.5 mN indent, the pop-in occurs close to the maximum load, almost no further loading takes place. For the 5 mN and the 10 mN indent, the volume around the indent undergoes further plastic deformation with increasing loads without showing additional spontaneous pop-in events. Right after the pop-in, the slope of the load-displacement curve is steeper and almost parallel to the unloading curve of the experiment. The cause for this could be a relaxation of the stored elastic energy of the indenter system, which is transferred into plastic deformation.

In Figure 4.8e the pop-in length (see Figure 4.8a) over the pop-in load of the twelve nanoindentation experiments listed in Table 3.1 are shown. The mean pop-in length is 81 nm. The pop-in length and the pop-in load show a linear relation. This result again indicates, that the stored elastic energy of the loaded indenter is transferred to plastic deformation of the sample surface after the first dislocation avalanche is activated. The number of activated dislocations, N, during the pop-in event can be estimated by [68, p. 93], [88]

$$N = \delta_{exc}/b, \tag{4.4}$$

where δ_{exc} is the pop-in length and b is the length of the Burgers vector. The mean number of dislocations activated for the average value of all pop-in lengths shown in Figure 4.8e using equation 4.4 results to 314.

For the brass sample the activation of the first dislocation avalanche is indicated by a pop-in event. The pop-in event is started by activating a dislocation source or statistically stored dislocations close to the indenter tip near to the theoretical
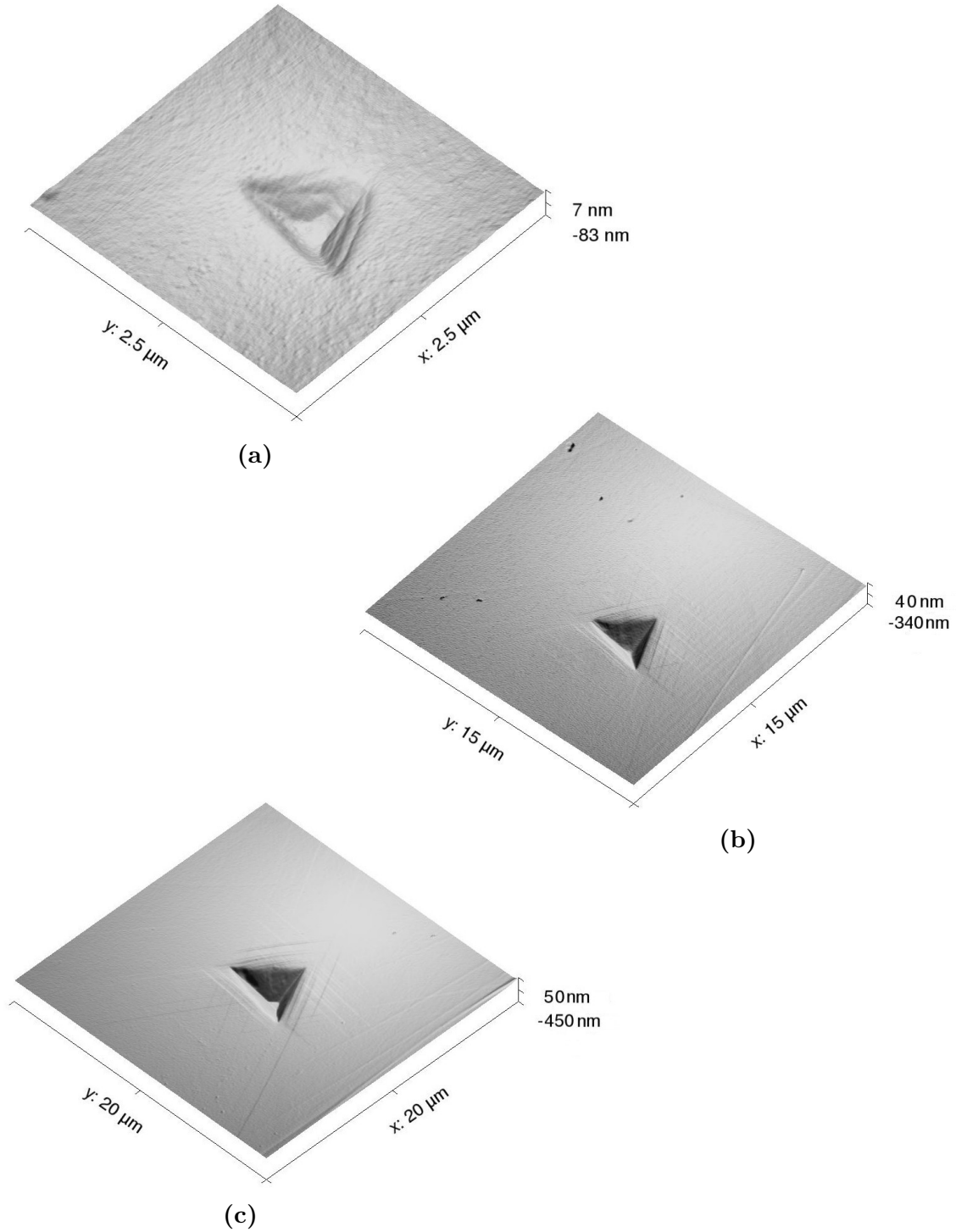
(a)

(b)

(c)

Fig. 4.7.: 3D representation of the AFM data shown in Figure 4.6. The loads of the imprints are **(a)** 0.5 mN, **(b)** 5.0 mN and **(c)** 10.0 mN. The information provided by these images is compareable to the SEM data. The SEM directly outputs a pseudo 3D view of the sample surface.
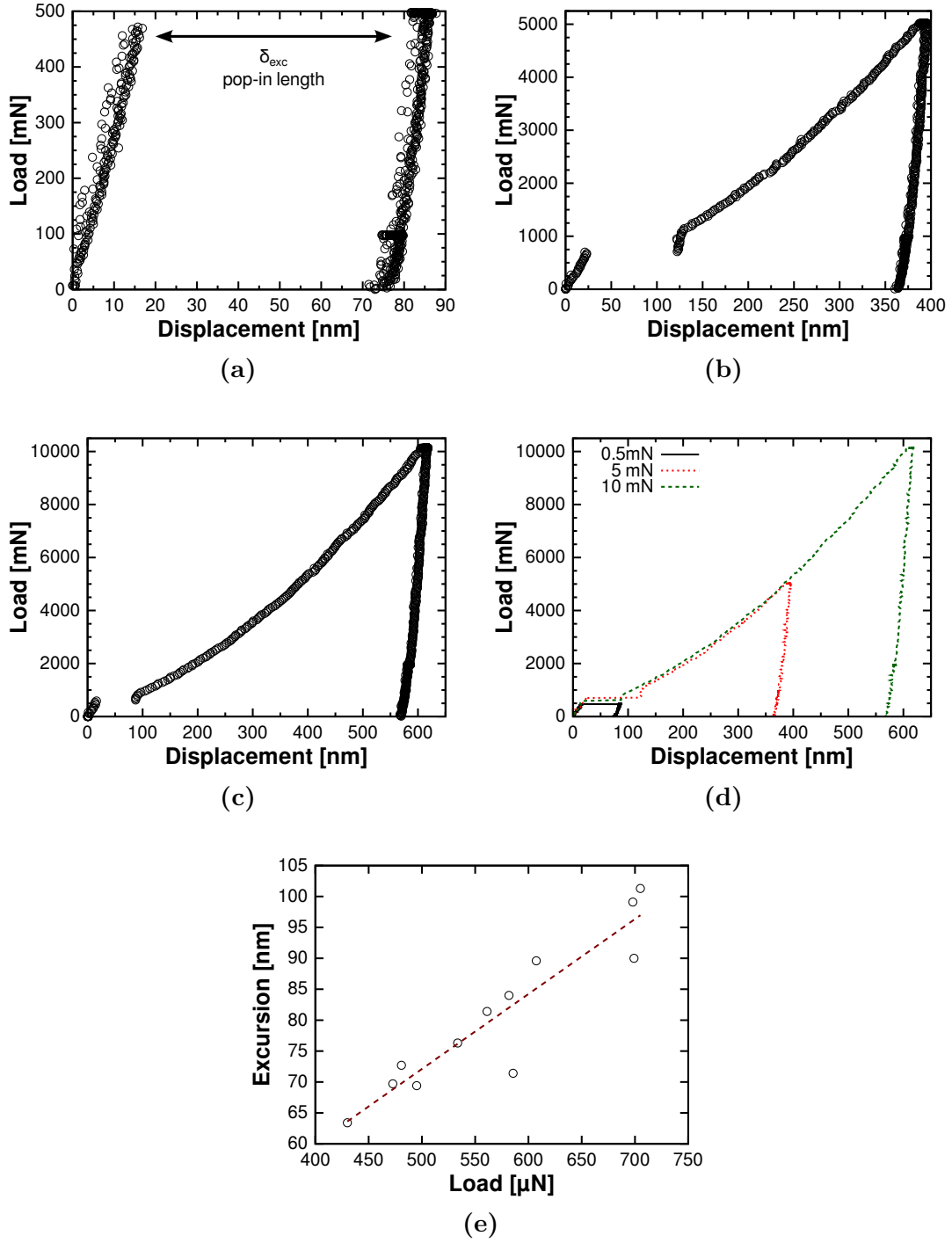
(a)

(b)

(c)

(d)

(e)

Fig. 4.8.: Load-displacement curves for the indents with loads of **(a)** 0.5 mN, **(b)** 5.0 mN and **(c)** 10.0 mN. **(d)** shows all datasets in a single plot. The first dislocation nucleation event (pop-in) appears at loads in the range of 400 µN to 800 µN and occurred in all three experiments. The 0.5 mN indent did not undergo any further plastic deformation after the initial pop-in event. **(e)** Graph of the pop-in lengths over the pop-in loads. Roughly, there is a linear relation between these two characteristics.

strength of the material. In contrary to tungsten (BCC crystal system), or nickel and gold [89, 90], which can show "staircase yielding" for some surface orientations, enough slip systems are available to continuously activate plastic deformation without further distinct pop-in events [91]. In the case of "staircase yielding", after each step of plastic deformation by dislocation avalanches, new dislocation sources or statistically stored dislocations need to be activated or re-activated by the stress field of the indenter. This may occur after a period of elastic loading, leading to the staircase effect [68, pp. 65].

Quantitative slip step analysis, estimating surface emitted dislocations

A quantitative analysis of the height of the slips steps around the nanoindent imprints is shown in Figure 4.9. The graphs show extraced 1D profiles at typical positions of plastic surface deformation close to the indent imprints. The backgrounds of the graphs show the AFM scans already seen in Figure 4.6 but include dark blue lines to indicate the position of the extracted 1D profiles. Depending on the indentation load, slip steps with heights in the range of 2 nm to 10 nm are observed. Increasing the indentation load by a factor of two from 5 mN to 10 mN mainly increases the density of slip steps. The height of the slip steps only slightly increases.
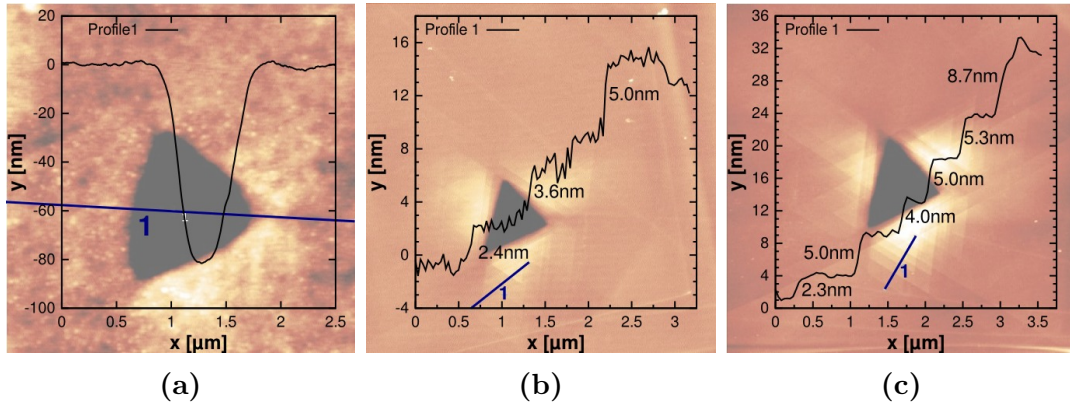

Fig. 4.9.: 1D profiles of the plastic zones around the nanoindent imprints. The background images show the AFM scans including lines indicating the position of the extracted 1D profiles. The indentation loads are **(a)** 0.5 mN, **(b)** 5.0 mN and **(c)** 10.0 mN. Please note the different y-scales!

The same sample material and same orientation of the surface in Section 4.1.1 "Slip step analysis close to micro-indents" was investigated. To calculate the number of emitted dislocations at the slip steps, equation 4.3 was used again. Table 4.5 lists the number of emitted dislocation for the slip steps shown in Figure 4.9. With increasing loads, the density of slip steps is increasing, the height of the single steps remains almost constant.

Indentation load	Step height	Nr. dislocations
5 mN	2.4 nm	11
5 mN	3.6 nm	17
5 mN	5.0 nm	24
10 mN	2.3 nm	11
10 mN	5.0 nm	24
10 mN	4.0 nm	19
10 mN	5.0 nm	24
10 mN	5.3 nm	25
10 mN	8.7 nm	41

Table 4.5.: Calculated number of dislocations for the slip steps shown in Figure 4.9.

The AFM and SEM images of the indent with a maximum load of 0.5 mN show, that number of dislocations activated to create the indent imprint after the first pop-in event are not emitted to the surface. About 300 dislocations contribute to form the indent imprint by plastic deformation. The application of further load after the pop-in activates dislocation sources deeper in the material which cross-slip to the surface. Slip steps in the height of single nanometers are created meaning that at least 10-20 dislocations are required to be visible at the surface. With increasing loads of the nanoindents, the density of slip steps is increasing in favor of the heights of the slip steps.

4.2. Indents@edge-method and combined AFM/SEM imaging

This section provides the background about a new micro-mechanical experiment, called the "indents@edge"-method. In the "indents@edge"-method, the lateral face of a cuboid shaped sample is indented at the edge close to the top surface, which is investigated by the SEM and the combined AFM/SEM instrument (See Section 3.2.2).

The method has the potential to investigate micro-plasticity in geometrically or dimensionally constrained volumes. Starting with the investigation of the indentation size effect (ISE) [92, 8, 93, 94] many different kinds of experiments have been developed to investigate size dependent plasticity. Uchic [9] proposed micro-mechanical testing experiments on FIB machined micro-compression cantilevers. Many others followed developing more complex configurations to investigate multilayered systems [95], large angle- and small angle grain boundaries and twins [74, 96, 75].

All the mentioned works rely on the fabrication of micropillars, which can become quite tedious if the features additionally should contain grain-, twin-boundaries, or other perturbations of interest. By preparing a sharp corner on a cuboid shaped bulk sample, using the new method introduced here, an area with the size of a few tenths of square millimeters is available to carry out indentation experiments. The top surface is ready to investigate plasticity events in lateral and vertical directions by the combined AFM/SEM instrument. By creating quite a large zone ready for mechanical testing, it is easier to include the interested features. To increase efficiency, the investigation of more than one feature in the same area would also be possbile.

4.2.1. Indent@edge on Brass

To provide a proof of concept, the new method is introduced using a brass single crystal. The sample was prepared following the description in Section 3.2.2. Figure 4.10 shows an SEM image of the AFM cantilever (left), the ion polished area prepared for investigation (center) and the tip of the picoindenter (right) with a 3-sided cube corner tip ($R \approx 50nm$).

The ion polished area is not showing a Gaussian shape as expected. This was caused by wear of the ion polisher's pinholes, which changed the ion beam shape. This can change the size of the accessible area for the experiment but has no negative effect on the quality of the polishing. On the left side of the sample, grinding grooves are viewed. The very bright band from the left top to the center bottom of the image is the vertical surface of the sample. The silver conductive paste, gluing the sample to the sample holder is seen further to the right. The paste is about 1 mm under the sample and can only be seen because of the large depth of field of the SEM at the low magnification of 80 x.

After the coarse approach of all components and the alignment to the SEM beam is complete (Figure 4.10), the components are carefully approached for imaging and the indentation experiment. The indenter is just a few hundred nanometers beyond the
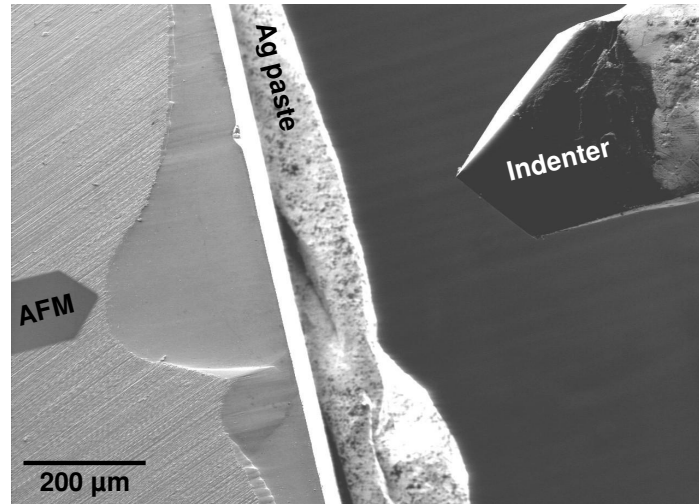
Fig. 4.10.: Overview of the experimental configuration before starting the experiment. The AFM cantilever is at the left, the horizontal ion polished area of interest in the center and the tip of the picoindenter on the right. All parts of the SEM image appear focused because of the large depth of field of the SEM at low magnifications.

sample surface and can still hit the AFM cantilever when it is sitting at the imaging position. The reason for this is because the position of the AFM cantilever tip may lie 6 µm to 8 µm behind the end of the AFM cantilever. During AFM imaging and experiment the respective other part (AFM or indenter) must be retracted for a few tens of micrometers. Details are given in Section 3.1.

Analysis before the experiment

After positioning in the area to carry out the experiment using the SEM in a fast scanning mode, the area of interest was imaged by the AFM. The scanning parameters are listed in Table 4.6 and the image is shown in Figure 4.11. The AFM scan showed a flat area without any slip steps indicating an undeformed area, but revealed surface contamination which was not observed in the SEM. A reason for not observing the contamination with the SEM could be a noisy image, caused by the fast SEM beam scanning speed chosen. The contamination was most likely induced by residues of condensed isopropanol after sample cleaning. The position was avoided by moving the sample a few micrometers and checking the new position using the SEM. To save time, the AFM scan was not repeated, only a slow high resolution SEM scan was performed to ensure proper conditions for the experiment, see Figure 4.11a.

Load-displacement data analysis of the indentation experiment

The indentation experiment was carried out performing six successive loading steps to a maximum load of 12.5 mN and a total displacement of 2.3 µm. Table 4.7 lists

Scan size	Lines	Scan speed	k_i	k_p
4 μm x 4 μm	256	$0.2\,\mathrm{s}^{-1}$	250	500

Table 4.6.: Scanning parameters for the AFM image close to the indented area before the indentation experiment.

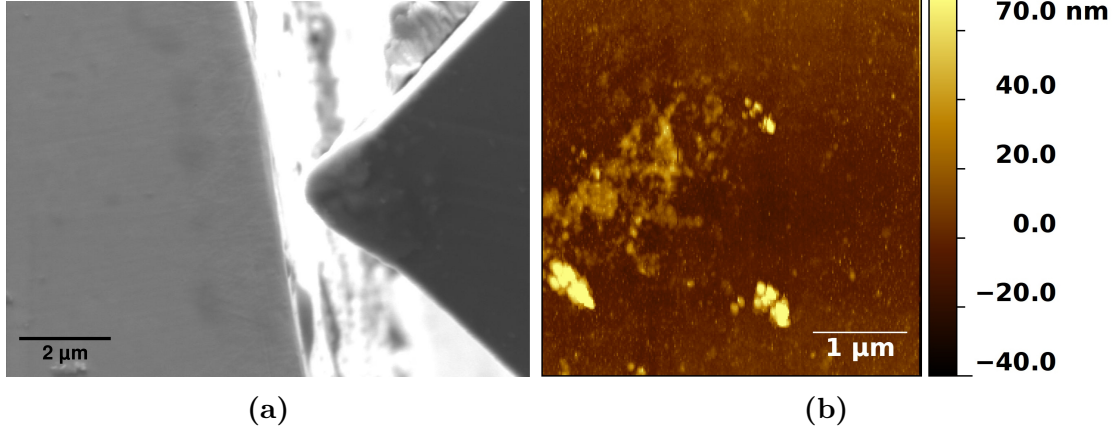(a)   (b)

Fig. 4.11.: (a) SEM image and **(b)** AFM image of the sample surface before the indentation experiment. The SEM image shows a slightly mechanically pre-deformed zone close to the edge. The AFM shows surface contamination. The contamination could have been caused after cleaning the sample again after ion polishing. No slip steps, indicating a plastically pre-deformed zone are viewed by the AFM scan.

the maximum load and maximum displacement after each step. The according load-displacement curves are shown in Figure 4.12, for comparison the 10 mN nanoindentation data of Section 4.1.2 is included in the graph. Please note the different shapes (Berkovich vs. Cube corner) of the indenter and tip radii (750 nm vs. ≈50nm) used for the nanoindentation and the indent@edge experiments, respectively.

The elastic unloading and loading curves for all segments in Figure 4.12 are parallel and the plastic loading curves follow each other perfectly. This indicates that the withdrawing of the indenter after each loading cycle had no negative effect on the experiment and it was possible to repeatedly hit the indent imprint on the sample surface again for each cycle. After each loading step, the surface was probed for arising slip steps by using the SEM to start an AFM scan after the first signs indicating a plastic deformation of the surface.

The load-displacement data does not show any pop-in events. The reasons for this behavior could be:

- Influences from the new type of sample geometry having an unconstrained surface.

- A contribution from the already deformed zone close to the edge of the sample

Step	Max. load	Max. displ.
1	2 mN	0.29 µm
2	4 mN	0.69 µm
3	6 mN	1.1 µm
4	8 mN	1.5 µm
5	9 mN	1.7 µm
6	12.5 mN	2.3 µm

Table 4.7.: List of loading sequences for the brass indent@edge experiment. A cube corner indenter tip was used for the experiments.

caused during preparation. Introduced defects and dislocation sources in the pre-deformed zone may explain the continuous plasticity curve.

- The smaller tip radius of the cube corner used in the indent@edge experiment was unable to activate more statistically stored dislocations (SSDs), preventing distinct pop-in events [68, p. 84], [97].

Compared to the nanoindentation data in Section 4.1.2 the indent@edge experiment also shows a strictly increasing work hardening. Again, note that different indenter tips were used. To reach equal indentation depths, the load for the Berkovich indenter needs to be several times higher than for the cube corner indenter. The influence of the indenter tip geometry on the load-displacement curve is discussed by Fischer-Cripps [98, pp. 24] and Chudoba [99]. A detailed comparison on copper was performed by Srivastava [100].

AFM and SEM data analysis after the experiment

After loading the sample with the nanoindenter's maximum force of 12.5 mN, a slip pattern at the surface was detected by the SEM. The dimensions of the slip pattern indicate the size of the plastic zone under the indent in vertical and lateral direction, see Figure 4.13. The SEM and AFM images are shown Figure 4.14. The parameters for the AFM scan are listed in Table 4.8.

Scan size	Lines	Scan speed	k_i	k_p
6 µm x 6 µm	256	$0.1\,s^{-1}$	250	500

Table 4.8.: AFM scanning parameters for the plastically deformed area of the indent@edge experiment

The radius of the plastic zone is about three times higher than the diameter of the indent imprint. This is in accordance with M. Resters work on vertically scanning indents using the FIB and the EBSD method on Cu $\{1\,1\,1\}$ surfaces [101]. The value for the vertical in-depth direction the plastic zones is about the same as the indent depth, which again corresponds to the data of Rester's work.
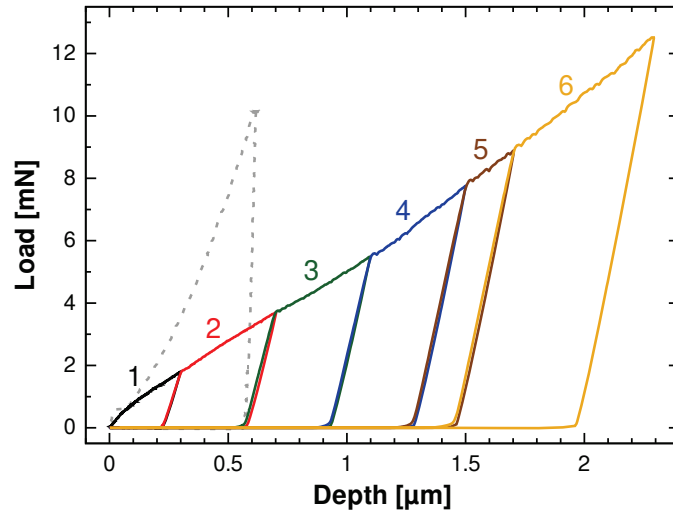
Fig. 4.12.: Load-displacement curves for the indent@edge experiment on the Brass sample. No pop-in events were observed. The single loading segments match each other very well, indicating that the indenter always hit the same position again after each loading step. For comparison, the data from Figure 4.8c is displayed as dashed, gray line.
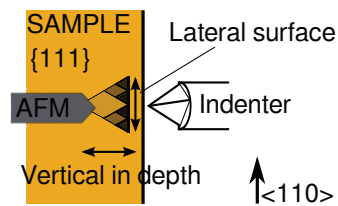

Fig. 4.13.: Sketch of the information given by the indent@edge experiment. By looking at the surface orthogonal to the indented one, not only the lateral extent of the plastic zone but also the vertical in depth information is accessible.
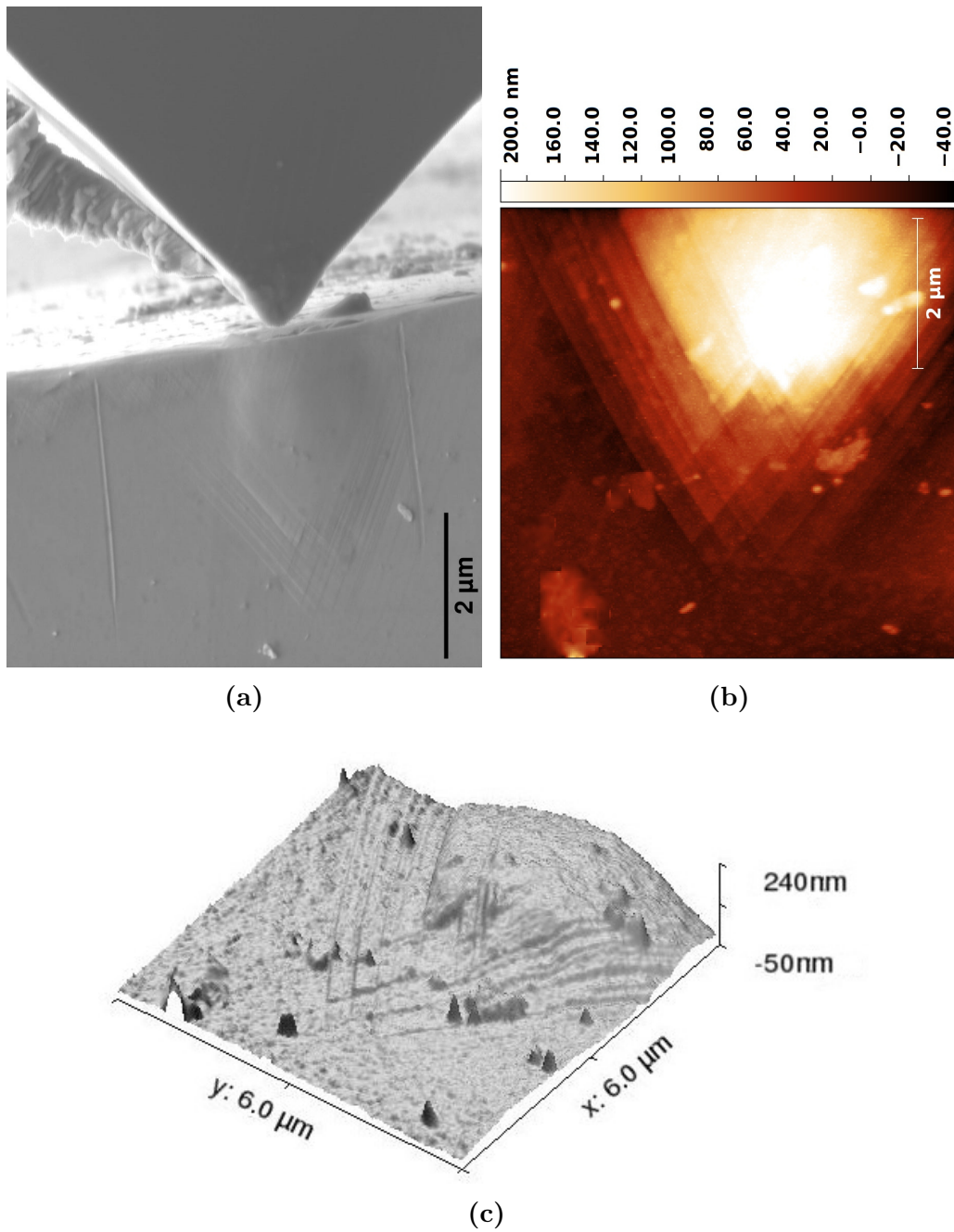
(a)   (b)

(c)

Fig. 4.14.: (a) SEM image **(b)** 2D AFM height image and **(c)** 3D AFM height image of the sample surface after the successful indentation experiment. Close to the edge of the sample, the surface shows a curvature, surrounding the indent. The curvature is viewed best on the SEM image (a) and the 3D AFM image (c).

Close to the edge of the indented surface, no slip steps are observed, but the whole area shows a curvature, indicating a rotation of the crystal orientation close to the indenter tip, as studied by Zaafarani with 3D EBSD and modelling using a crystal plasticity finite element method [102].

Quantitative analysis of the plastic zone

The AFM scan allow a quantitative analysis of the plastic deformed zone of the indent. A characteristic number describing the spatial extension of the plastic zone of the indent is the radius of the plastic zone, R_p. The experimental results of R_p from the AFM scan can be compared with models suggested in the literature as described by Zielinski [103] and Kramer [81]:

$$R_p = \sqrt{\frac{3P}{2\pi\sigma_{ys}}},$$
(4.5)

where P is the applied load and σ_{ys} is the yield strength. The yield strength σ_{ys} and the hardness of a material are related via the Tabor relationship [104]

$$\sigma_{ys} \approx \frac{1}{3}H$$
(4.6)

The hardness was evaluated by using the load displacement data of the nanoindentation experiments listed in Table 3.1 and found to be an average of $1.42\,\mathrm{GPa}$. The radius of the the plastic zone suggested by Kramer's model is

$$R_p = \sqrt{\frac{9 \cdot 12.5}{2\pi \cdot 1.42}} = 3.55\mu m.$$

This value agrees well with the dimensions of the plastic deformed zone shown in Figure 4.14.

Figure 4.15 shows slip step profiles at the bottom of the indent's plastic zone. The height of the slip steps in the area of Profile 1 and Profile 2 is in the range of single nanometers to a few tens of nanometers. The total height of the curvature of the area on the right side, close to the edge of the sample, is about $200\,\mathrm{nm}$. The size of the plastically deformed region is about $4\,\mu\mathrm{m}$ x $8\,\mu\mathrm{m}$ with heights starting from about $200\,\mathrm{nm}$ at the curvature down to steps of single nanometers at the borders on the left and the right side of the curvature.

A detailed analysis at the bottom of the plastic deformed area was performed to investigate a distinct area of plastic deformation which just arises for high indentation loads [67]. The number of emitted dislocations for the two slip steps approximated by dashed lines in Figure 4.15 having heights of $15.2\,\mathrm{nm}$ and $10.2\,\mathrm{nm}$ for Profile 1 and
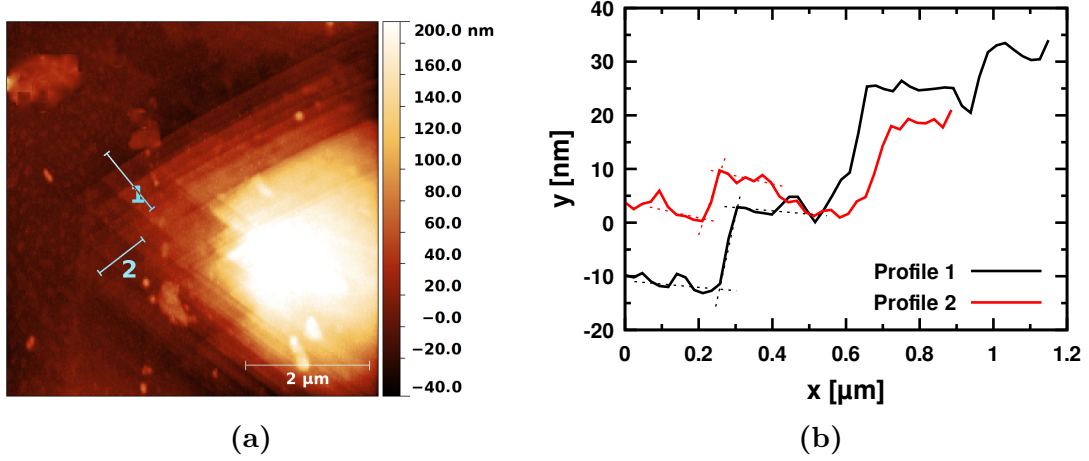
Fig. 4.15.: (a) Profiles in the AFM image, **(b)** graphs showing the profiles in (a). The slip-step heights of the profiles are in the range of 5 nm to 15 nm, the curvature of the surface on the right side has a total height of about 200 nm. The two slip steps approximated by the dashed lines have a height of 15.2 nm (Profile 1) and 10.2 nm (Profile 2).

Profile 2, respectively give for Profile 1

$$n = \frac{\sqrt{3/2}h_v}{a/\sqrt{2}} = \frac{\sqrt{3} \cdot 15.2}{3.65} \approx 72,$$

and for Profile 2

$$n = \frac{\sqrt{3} \cdot 10.2}{3.65} \approx 48$$

dislocations emitted to the surface.

4.3. Indentation experiments: Summary

The plastic zones of micro- and nanoindentation experiments were analyzed by the combined AFM/SEM instrument. The number of emitted dislocations was evaluated in the plastic zone around the imprint of the indented surface. Also an analysis of the plastic zone under the indents was performed by introducing a new experimental method called the "indent@edge"-method. The results agree well with works and models found in the literature.

The AFM and SEM images of the nanoindentation experiments show that with the first pop-in event plastic deformation of the surface is initiated. The dislocations activated in the first pop-in event are not emitted to the surface. About 300 dislocations contribute to the formation of the initial indent imprint through plastic deformation.

The application of further load after the pop-in activiates dislocation sources deeper in the material which cross-slip to the surface. Slip steps in the height of single nanometers are created. With increasing indentation loads, the density of slip steps is increasing in favor of the heights of the slip steps.

The model of Rester [67] suggests that in Region 2 (Figure 4.16) geometrical necessary dislocations are created to form the indenter imprint. In Region A dislocation sources of a second slip system are activated and emitted to the surface (Region 1). Dislocations of opposite sign move, depending on the activated slip system, to regions 3 and 4. For low indentation loads, no dislocation sources in A are activated, that is the reason why the surface around the indent imprints shows no slip steps. The results presented here agree with this model.
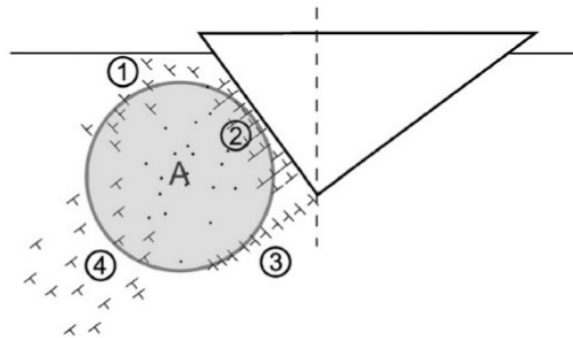

Fig. 4.16.: Model of Rester [67] to explain the movement of dislocations during a indentation experiment.

4.4. Combined AFM and SEM micro-beam and -pillar testing

In this section, the capability of the AFM for in-situ micro-mechanical testing on micro-bending beams and micro-compression pillars is shown. The FIB machined samples are tested using a Hysitron PI85 SEM Picoindenter which is compatible with the combined AFM/SEM instrument (Chapter 2). The preparation of the microsamples is discussed in Section 3.2.3.

4.4.1. Overview of experiment

Figure 4.17a shows micro-bending beams on a copper single crystal prepared by the first method shown in the experimental Section 3.2.3. Figure 4.17b[1] shows micro-compression samples on a copper bicrystal fabricated using the second micro sample preparation method described in the same section. The compression-test pillar in the center contains the grain boundary of the bicrystal. The different crystal orientations of the two grains are viewed on different grayscale levels in the SEM image, caused by the electron channeling contrast [105, 106].
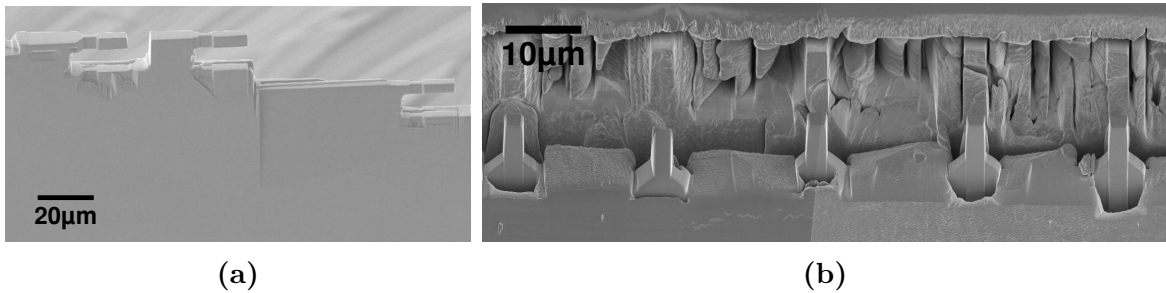

(a)   (b)

Fig. 4.17.: Overview of **(a)** three micro-bending test samples prepared by the first method **(b)** micro-compression test samples prepared by the second method. The testing feature in the center contains a grain boundary.

SEM images give an overview of the bending beam and compression test samples before starting the micro-mechanical testing are given in Figure 4.18. All samples were accessbible for the picoindenter and the AFM. For the bending beams, which are larger than the compression test pillars, a simultaneous approach of AFM cantilever and picoindenter was possible. Simultaneous imaging and mechanical deformation of the sample is not possible because of vibrations caused by movements of the indenter and by spontaneous processes like pop-in events during the plastic deformation.

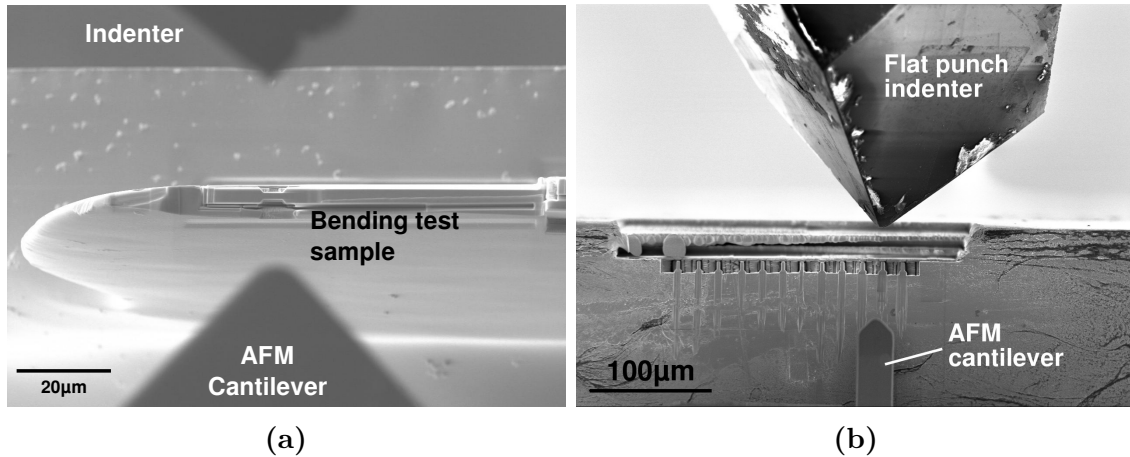[1]Photo with compression test samples provided by Nataliya Malyar, MPIE Duesseldorf

(a) (b)

Fig. 4.18.: SEM image of an overview of **(a)** a micro-bending experiment showing AFM cantilever, bending test sample and picoindenter and **(b)** a micro-compression experiment showing AFM cantilever, compression test samples and picoindenter before carrying out the experiment.

Loading parameters

Table 4.9 shows the loading parameters of the mechanical testing experiments. For the case of bending beams, the load was increased until slip lines were first observed on the surface. The according values for strain and strain rates were chosen with the help of Motz [38] and Kremmer [107] according to their work on mechanical micro-bending experiments. For the compression test pillars, typical values suggested by the Jennings [108] on the transition of the strain-rate sensitivity in nano-sized compression test samples and Imrich's [75] work on micro-compression pillars containing grain boundaries have been chosen. The high maximum outer fiber strain of the bending beam was applied because no slip steps were observed at the sample surface. The reason was contamination caused by the SEM electron beam which is discussed in the following sections.

Type of test	Max. strain	Strain rate
Compression	10 %	$10^{-3}\,s^{-1}$
Bending	25 %	$10^{-3}\,s^{-1}$

Table 4.9.: Loading parameters for the microsamples of the bending- and compression tests.

4.4.2. SEM- and AFM-images of deformed samples

Figure 4.19 shows SEM and AFM height images of the deformed microsamples. If a free-standing feature, like a compression pillar, is scanned by the AFM, additional care

is needed. It should be avoided to scan the sample edge to prevent the AFM cantilever tip from damaging the microsample. The gains of the controller are adjusted to scan slip steps in the height of nanometers, making it nearly impossible for the controller to track micrometer sized step at the sample edge. It should be mentioned again, that the situation is much worse in vacuum compared to in air AFM scans. When adjusting the scan size the so-called overscan parameter needs to be taken into account. This parameter is necessary for a smooth turn around of the AFM nose to prevent abrupt movements when switching from trace to retrace [109] during scanning, which could lead to unwanted vibrations of the AFM system. The overscan parameter for the current prototype of the combined AFM/SEM instrument is set to 10 %. Typical values for the AFM scanning parameters like image resolution, scan speed and gains are given in Table 4.10.
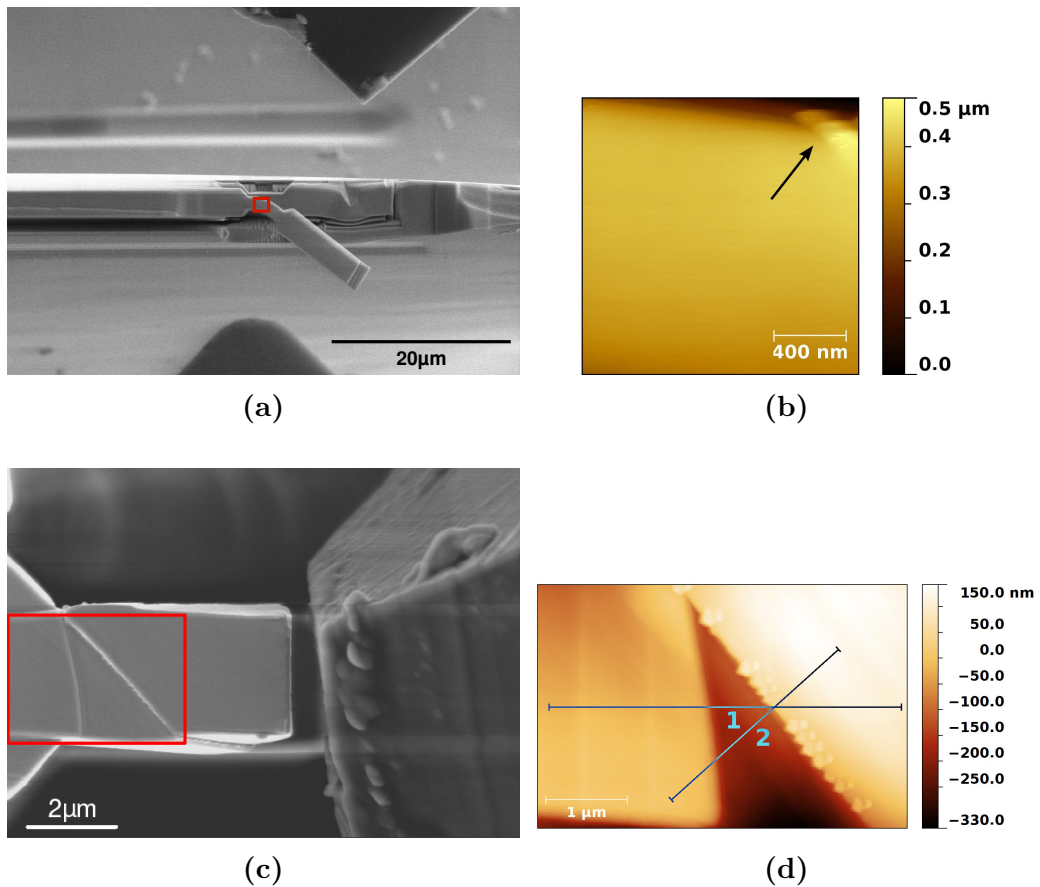

Fig. 4.19.: Details of the deformed microsamples imaged by **(a, c)** SEM and **(b, d)** AFM. The micro-bending sample (a, b) is heavily contaminated, no slip steps can be seen on the surface. A crack (arrow) in the contamination layer is seen in the upper right corner in (b). The micro-compression sample (c, d) was not affected by contamination due to a improved testing procedure. The red rectangles indicate the scanning areas of the AFM.

Scan size	Lines	Scan speed	k_i	k_p
2.5 µm x 2.5 µm	256	$0.25\,\text{s}^{-1}$	200	400

Table 4.10.: Typical scanning parameters for an AFM image of a microsample.

The bending test experiment failed because of heavy surface contamination on the sample from the electron beam. At the top right corner of the bent cantilever's AFM height image a crack in the contamination layer is seen (Fig. 4.19b). The contamination was caused by the SEM electron beam cracking hydrocarbons and a redeposition of the cracked carbon residues on the sample surface [110]. Two main reasons causing the heavy contamination should be mentioned here:

- **Long scanning times:** The bending test experiments were carried out first. The lack of experience in finding the free standing samples having dimensions two to three times smaller than the AFM cantilever led to extraordinarily long electron beam scanning times.

- **Instrumental "quirks":** After an abort by the user of the electron beam scanning with the Zeiss DSM 982, only the image on the computer monitor is frozen, but the electron beam continues to scan the sample surface. This was initially unknown during the experiment.

Contamination of the compression test samples was avoided by

- shorter scanning times during cantilever approach,

- turning off the electron beam by blocking the electrons using an unused position at the SEM aperture wheel,

- acquiring a SEM plasma cleaning system to have a cleaner SEM environment [111, 112].

Applying the improved test procedure for the compression tests led to successful experiments shown in Figure 4.19c (SEM) and Figure 4.19d (AFM). The main plastic deformation of the compression sample occured on two activated slip systems close to the base of the pillar. A few less pronounced slip lines on the same two slip systems are visible on the SEM and AFM images. The height profiles indicated by lines in Figure 4.19d are shown in Figure 4.20.

The SEM, AFM images and line profiles show, that a wedge shaped part of the pillar is squeezed out of the sample to undertake the plastic deformation of the compressed pillar. This behavior should be expected, as the pillar's top and bottom part are clamped by the sample base and the flat punch indenter, restricting a movement orthogonal to the compression axes (see Figure 4.21). Restrictions and preventive measures to achieve valid results in micro-compression test configurations are extensively discussed by Kirchlechner [113, 114].

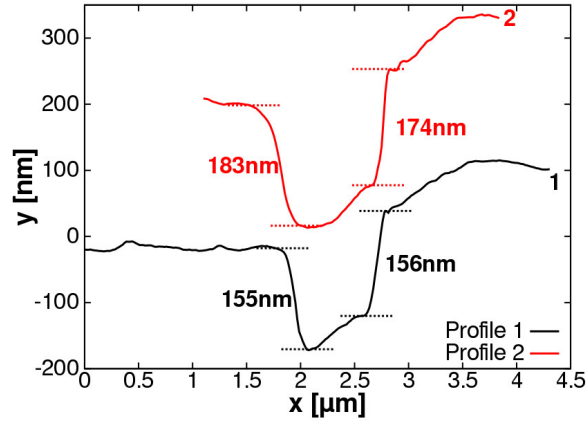**Fig. 4.20.:** Height profiles of the activated slip systems along the lines shown in Figure 4.19d
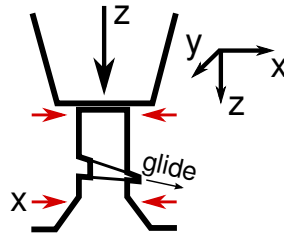

Fig. 4.21.: Sketch of the sideview of a possible compression test experiment along the z-axes. Base and top of the pillar cannot move in the directions orthogonal to the compression axes along the x- and y-direction, indicated by the red arrows. The y-direction faces outwards the page and is not shown.

After overcoming the problems with surface contamination of the micro samples, first successful micro-mechanical tests were performed. For an in-depth analysis of this kind of tests, a higher quantity of samples and testing experiments would have been necessary, exceeding the scope of this work.

4.5. In air in-situ thin film testing

The AFM can also be used as a separate in-situ instrument in air. In this section, the results of mechanical testing experiments on thin metal films deposited on polymer substrates are shown. This kind of material systems are commonly used in flexible electronic devices. To ensure a long life time, these compound systems have to be robust and reliable while stretching and compressing and need to withstand high current densities without failing mechanically or electrically. In this work, 100 nm thick copper films on 50 µm polyimide have been investigated.

A combination of the in-situ AFM with a straining stage and an ohmmeter in 4 point probe configuration allows the examination of this material systems on thinning, crack formation and changes of resistance in the metal layer [115, 116, 117, 118]. The details of the configuration are described in the instrumental chapter, Section 2.3.

4.5.1. Sample and experiment overview

The 100 nm thin films were produced by the deposition of copper on polyimide (brand UPILEX) using electron beam evaporation. The vacuum in the deposition chamber varied slightly between the start and the end of the deposition process ($5 \cdot 10^{-7}$ mbar – $2 \cdot 10^{-7}$ mbar). A deposition rate of $5 \, \text{Å}/s$ was chosen. The thickness of the 8 x 45 mm sized polyimide samples was 50 µm. A detailed description for the sample preparation is given by Berger [119, p. 17], the average grain size of the polycrystalline copper film was determined in the same work with TEM and found to be an average of 80 nm [119, p. 27].

To investigate the mechanical behavior of the thin copper layer on a polyimide substrate, the samples were mounted on a Kammrath & Weiss [52] straining stage and strained in consecutive steps up to a maximum value of 16 %. The initial gauge length was 14 mm. The AFM nose needs to reach the sample surface between the grips of the tensile device, so values smaller than 14 mm for the initial gauge length are not possible.

After each straining step an AFM image of the sample surface was taken. The electrical resistance of the copper film was continuously acquired by a Keithley 2400 digital multimeter [120] in four point probe mode during the whole experiment. Detailed data like sequence number, increase in strain, total strain and the according figure number of the AFM images are listed in Table 4.11.

For each straining step, a quadratic AFM scan of the sample surface with a size of 20 µm x 20 µm was taken to record plastic deformation, necking and crack formation. The scanning parameters, which remained the same for all scans, (Table 4.12) and the AFM height images are shown in Figure 4.22. At a strain of 2 %, no visible plastic deformation or cracking occurred, that is why the according AFM image is not shown and no crack analysis was performed after the first straining step.

The Kammrath & Weiss straining stage provides two symmetrically movable cross heads to keep the center of the sample at the same position. This only works for the very center of the strained sample. A slight deviation in position of the AFM scanner
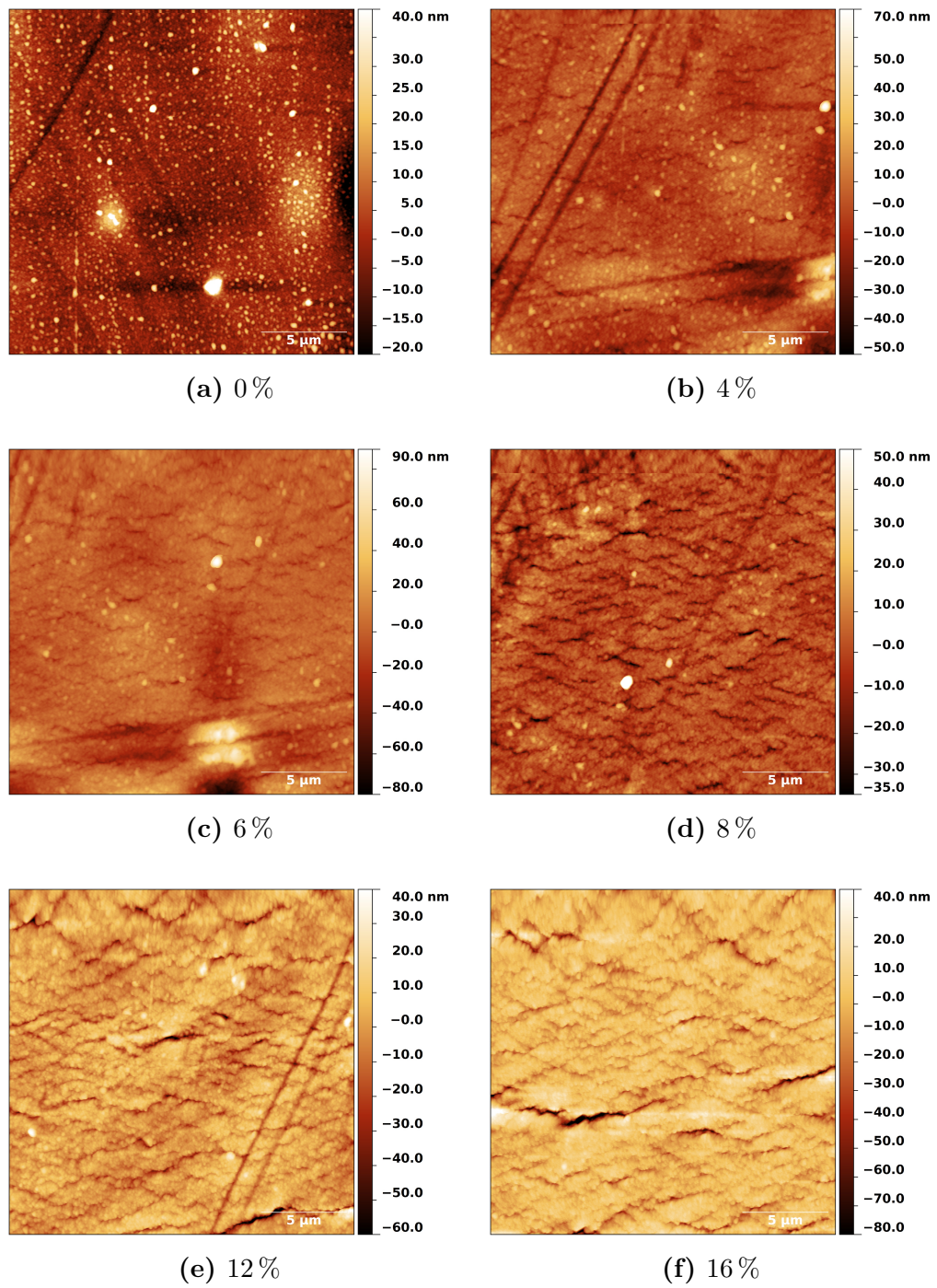
(a) 0 %

(b) 4 %

(c) 6 %

(d) 8 %

(e) 12 %

(f) 16 %

Fig. 4.22.: AFM scans of the strained film after each straining step listed in Table 4.11.

Nr. of step	Δ strain	Total strain	AFM analysis
0	2 %	0 %	Fig. 4.22a
1	2 %	2 %	-
2	2 %	4 %	Fig. 4.22b
3	2 %	6 %	Fig. 4.22c
4	2 %	8 %	Fig. 4.22d
5	4 %	12 %	Fig. 4.22e
6	4 %	16 %	Fig. 4.22f

Table 4.11.: Straining steps performed for the in-situ thin film test. First, the total strain was increased in steps of 2 % and by 4 % during the last two steps.

Nr. of step	Parameter	Value
	Scan size	20 μm
	Lines	1024
0 − 6	Scanspeed	$0.6\,\mathrm{s}^{-1}$
	k_i	5000
	k_p	8000

Table 4.12.: Scanning parameters for the images of the in-situ thin film straining experiment in air.

at the center causes a movement of the area of interest during straining. This was the case for this experiment, so it was not possible to stay at the same position after the straining steps. A microscope with a high magnification of at least 200x would have been needed to detect the small sample movements. With the AFM coarse sample stage, which is also produced for use in air, a correction of the detected AFM position missmatch technically would be possible.

4.5.2. Deformation analysis

The strain dependent average deformation spacing which takes into account both cracks and necks was determined using the method of Cordill [121], this method was utilized on various material systems by Berger [119], Putz [122] and Marx [117]. Cordill's model states that if the depth of a surface depression caused by the straining of the sample exceeds 15% of the film thickness, a crack is detected. If the depression is below 15%, it is just necking (localized film thinning), a sign of the ongoing formation of a crack of the film.

Each AFM image shown in Figure 4.22 was analyzed by investigating three vertical 1D profiles at horizontal postions of 4 μm, 10 μm and 16 μm. Three typical profiles at strains of 0 %, 4 % and 16 % are exemplified in Figure 4.23a. The average deformation spacing as a function of the strain evaluated from all of the 1D profiles is shown in Figure 4.23b. The necking was not evaluated for high strains, because the sample

surface already was strongly deformed and therefore necking was not easy to identify. Depending on the strain, the values for the spacing of the surface features are in the range of $5\,\mu m$ to $0.5\,\mu m$, which is in good agreement with the experiments of Berger [119, p. 34].
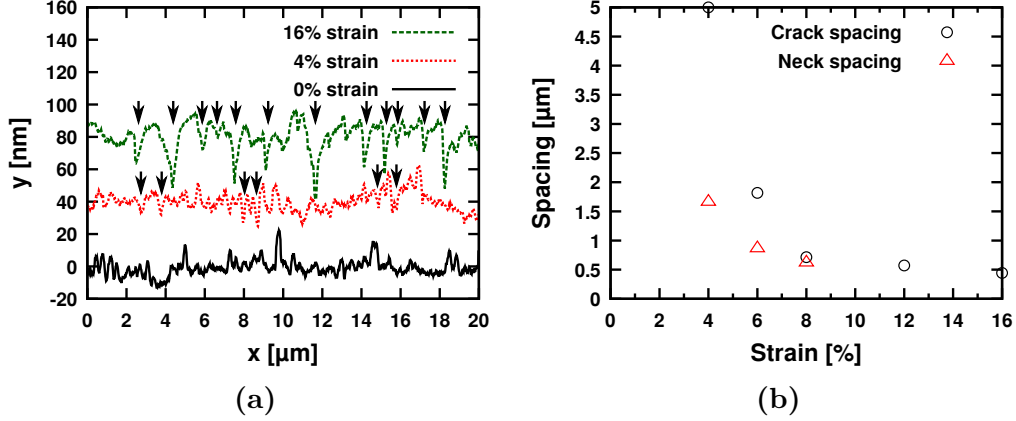

Fig. 4.23.: Analysis of the average crack spacing as a function of the strain. **(a)** Typical 1D profiles of the sample surface at a strain of 0%, 4% and 16%. Necks/cracks indicated by arrows. **(b)** Crack/neck spacing vs. strain.

4.5.3. Strain dependent electrical resistance

The electrical resistance of the film was continuously recorded during the whole experiment using a Keithley 2400 multimeter in 4 point probe configuration. The average values of the resistance recorded after each straining step and the relative resistance R/R_0 are given in Table 4.13. The relative resistance was calculated after subtracting the parasitic resistance $R_{parasitic} = 0.797\,\Omega$, which was evaluated by knowing the electrical resistivity of copper, the sample dimensions, and the electrical resistance R_{0film} of the thin copper film before straining,

$$R_{parasitic} = R_{0measured} - R_{0film}, \qquad (4.7)$$

giving the resistance R_{film}

$$R_{film}(\epsilon) = R_{measured}(\epsilon) - R_{parasitic} \qquad (4.8)$$

during the mechanical testing experiment. The parasitic resistance is caused by the contact-circuit resistance and a inhomogeneous current density in the thin film close to the probes of the Ohmmeter.

Already after the first straining step, when no change of the surface in the AFM images were observed, an increase in resistance can be seen. The change in resistance is almost linear for the first few steps, and turns into a nonlinear shape with

Nr. of step	$R_{measured}$	R_{film}	ΔR	R/R$_0$
0	1.141 Ω	0.344	-	1.0
1	1.155 Ω	0.358	14 mΩ	1.041
2	1.168 Ω	0.371	13 mΩ	1.078
3	1.180 Ω	0.383	12 mΩ	1.113
4	1.197 Ω	0.4	17 mΩ	1.163
5	1.256 Ω	0.459	59 mΩ	1.334
6	1.341 Ω	0.544	85 mΩ	1.581

Table 4.13.: Resistance data of the thin film straining experiment. At the last straining step, the resistance of the Cu film increased by 58%.

increasing strains at around 10%. At first only the change in dimensions of the sample caused by the straining changes the electrical resistance. Later the main contribution to the resistance curve (Figure 4.24) is caused by the formation of crack and crack extension [123].
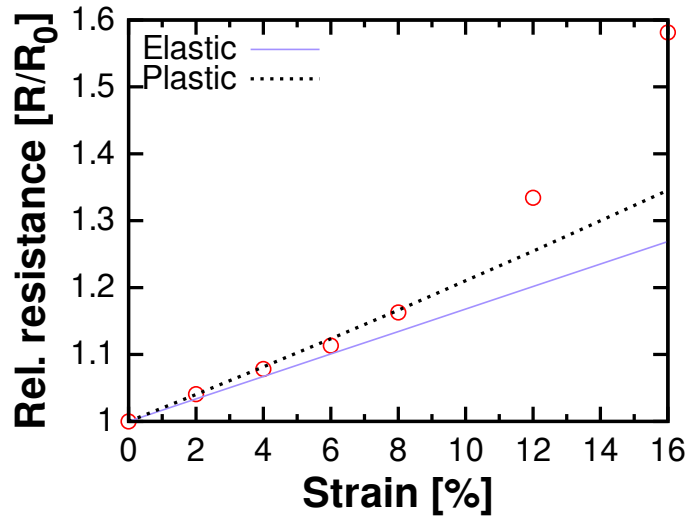

Fig. 4.24.: Relative resistance R/R$_0$ vs. strain of the thin film: Starting with a linear increase the resistance curve turns to a nonlinear behavior when cracks are formed and extended in the thin copper layer.

The initial resistance of the film is given by the resistivity $\rho = 1.721 \cdot 10^{-2} \, \Omega \cdot mm^2/m$ of copper, the initial length L_0 and the initial cross section A_0 of the film

$$R_0 = \rho \frac{L_0}{A_0}. \tag{4.9}$$

During straining the change in resistance is caused by elastic and plastic deformation.

At small strains and having materials with a high Poisson's ratio ν, the initial increase in resistance can be approximated by the following equations[124]:

$$\frac{R}{R_0} = (1 + 2\nu) \cdot \epsilon + 1 \tag{4.10}$$

in the elastic, and

$$\frac{R}{R_0} = (1 + \epsilon)^2 \tag{4.11}$$

in the plastic case. The curves of both equations are shown in Figure 4.24. In the case of the experiment shown here, the measured relative resistance is in good agreement with the linear model until a strain of 2% and coincides with the plastic model until a strain of about 8%. After that the formation of cracks and crack extension increasingly contribute to the film resistance, leading to the nonlinear behavior seen in Figure 4.24.
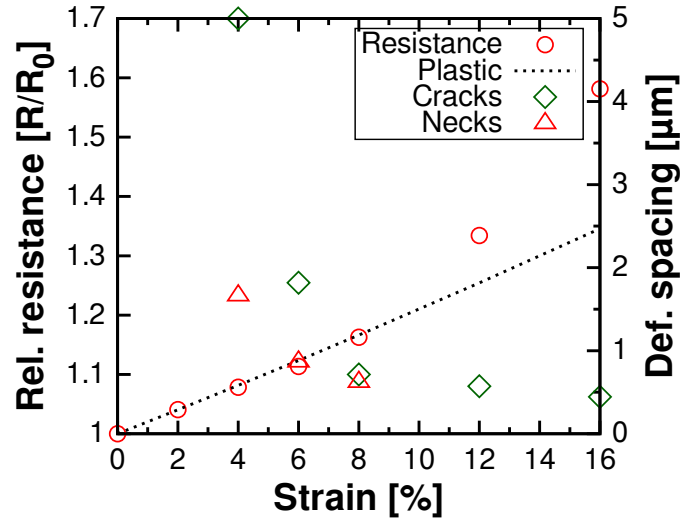
4.5.4. Summary

Fig. 4.25.: Change of relative resistance (left y-axes) and deformation spacing (right y-axes) over strain. The theoretical curve for the change in resistance caused by a homogeneous plastic deformation of the sample is shown as a dotted black line.

The combined AFM/SEM instrument was used for in-situ testing of thin metallic films in air. The electrical resistance and the plastic deformation of the metal film was recorded during mechanical straining. The electrical data was compared with the theoretical case of a pure geometric alteration caused by a plastic deformation of the film. The plastic deformation of the surface of the metal film was quantitatively characterized by evaluating the deformation spacing of formed necks and cracks as a function of mechanical strain. The results for the plastic deformation of the surface

(Figure 4.23) and for the electrical resistance (Figure 4.24) were merged into one graph and are shown in Figure 4.25. For clarity, the theoretical resistance curve as a function of strain for the pure elastic case was omitted.

With the formation of first cracks in the metal film, the electrical resistance of the strained film still follows the expected behavior for the homogeneously plastically deformed case. After a saturation in crack density is reached, an opening of the cracks with further straining leads to a deviation of the resistance curve from the ideal slope. For the investigated copper film, this is the case at strains of about 8%.

5. Summary and Outlook

5.1. Summary

In this work, an AFM was successfully implemented inside of a SEM to perform in-situ mechanical testing experiments using various sample geometries and materials. The combination of an AFM and a SEM, two commonly used instruments in material science research, merges the benefits of two imaging techniques. The SEM provides fast scanning speeds and large scan sizes, while the AFM provides topography images with high z-resolutions and is insensitive to distortions caused by chemically altered surfaces. Microsamples for micro-mechanical testing experiments or any features of interest with sizes not resolveable by optical microscopes are easily localized using the SEM. During a mechanical testing experiment the surface topography is scanned at high resolutions using the AFM to better understand plastic deformation at the micro- and nanoscale.

The design of the AFM housing, coarse positioning stage and self-sensing AFM cantilevers make this a versatile instrument that is easy to operate remotely inside of the SEM chamber. The design of the AFM nose allows small working distances for the SEM and complex sample configurations. The AFM can be coarsely positioned along three axes independently from the SEM stage, enabling eight independent axes of the combined AFM/SEM instrument. It is ideal for in-situ micro-mechanical testing in vacuum, but also can operate as a stand-alone AFM for in vacuum and in air experiments.

The AFM consists of a coarse stage operated by two stepper motors and a piezo stick slip motor. The AFM scanner is operated by piezo multilayer actuators in a flex structure configuration. Strain gauges attached at the multilayer actuators allow an easy calibration of the system according to the linearity of the scanner. The use of self-sensing AFM cantilevers provides a compact footprint of the device which is easy to operate because laser alignment is not necessary.

The sample positioning and cantilever approach is carried out with the help of the SEM. This leads to prolonged SEM electron beam scanning times and a potential contamination of the sample surface caused by the electron beam cracking hydrocarbons. The contamination has to be avoided by having a clean SEM chamber and clean samples, short SEM scanning times and a standardized cantilever approach procedure to the sample surface. High resolution SEM images should be taken after scanning with the AFM.

The sample preparation for mechanical testing experiments was slightly adopted compared to conventional testing setups in the SEM. The testing features need to be

fabricated close to the top surface of the sample, so the AFM cantilever tip is able to reach them.

Small scale plasticity was examined by investigating

- Micro- and nanoindent imprints and the slip steps surrounding the plastically deformed surface.

- The volume under indents was examined by introducing a new type of experiment called "indent@edge"-method.

- Micro bending beams and compression test pillars during in-situ mechanical testing experiments.

- The electrical and mechanical behavior of strained thin films was studied using in-situ fragmentation experiments in air.

By knowing the orientation of the plastically deformed surface and at least one direction in the surface, all active slip systems contributing to the plastic deformation can be identified. The vertical step heights scanned by the AFM are projected to the directions of the active slip systems to calculate the number of dislocations emitted to the sample surface. The combined AFM/SEM system is capable of determining the number of contributing dislocations to surface plasticity events with a resolution of three to five dislocations.

The plastically deformed surface around nanoindents with different indentation loads was investigated by the new combined AFM/SEM instrument. The indent with the lowest load creating a permanent imprint on the surface didn't show any slip steps around the surface. None of the dislocations generated during a pop-in event which was recorded in the load displacement curve, were emitted to the surface. Only a small fraction of dislocations is emitted to the surface at higher indentation loads, when cross slip occurs or dislocation sources of secondary slip systems become activated. Also, the plastically deformed zone under the indent was investigated by introducing a new experimental method named "indent@edge"-method. The spatial extend of the plastically deformed zone under the indent determined by the new method agrees well with data from the literature.

In-situ straining experiments of thin metal films deposited on polymer substrates have been performed in air. The new AFM was combined with a 10 kN straining stage to investigate the plastic deformation and formation of cracks in the metal film. Additionally the electrical resistance of the film was recorded at the same time. The electrical current in the thin metal film to measure the electrical resistance had no negative effects on the AFM scans. Using the new AFM instrument with a picoindenter applaying a maximum force of 10 mN and a straining stage with a maximum force of 20 kN shows the high flexibility of the instrument.

5.2. Outlook

The new combined AFM/SEM instrument is ready for micro-mechanical testing to study fracture and plasticity at small scales. To contribute to a better understanding of plastic deformation mechanisms at small length scales a higher quantity of samples should be investigated. More materials with different stacking fault energies and crystal structures should also be included. The micro-mechanical testing experiments on bending beams and compression pillars with grain boundaries should be compared with the new indent@edge method. Further SEM characterization techniques like EBSD or EDX should be incorporated with the AFM/SEM setup in order to provide even more information about the microstructure and chemistry.

Necessary improvements for the prototype used in this work would be a better vacuum compatibility in order to reduce outgassing and virtual leaks of the components. The calibration methods to cancel nonlinearities at the image borders when scanning at large scan sizes also should be improved. The coarse stage currently is operated separately from the AFM controller using an external software. It would be more efficient to include the coarse stage control with the AFM controller software which would provide a more compact and simpler user interface.

A new experimental method, the "indent@edge"-method was introduced in this work. The new method simplifies the sample preparation and the procedure of approaching the AFM cantilever to the sample surface. In this work, the plastic deformed zone under nanoindents was investigated, but the new method also has potential to investigate plastic events at twin- and grain boundaries or even fracture in more brittle materials.

A. AFM cheatsheet

The "AFM cheatsheet" contains important data for everyday use. A copy should be near the instrument.
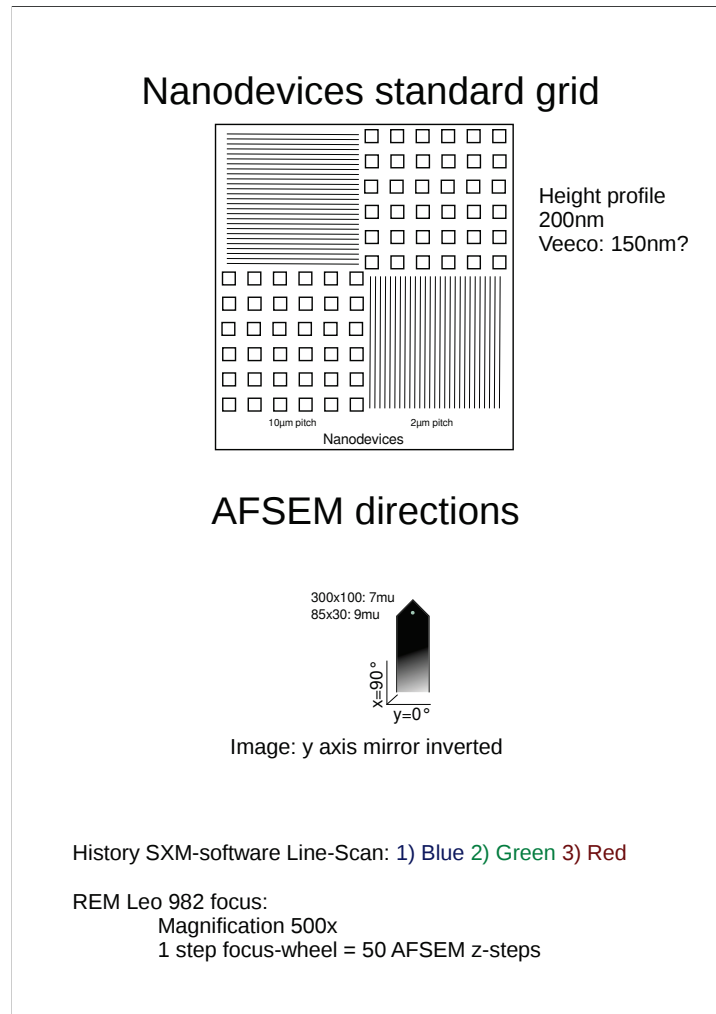

Fig. A.1.: Important data for everyday use: Structure and dimensions of the standard grating, cantilever data such as dimensions and relative position of the tip, a guide for easy approach when working with the SEM and a legend of the live data of the AFM software.

B. Mounting the AFM inside of the SEM chamber

This step by step guide was written for the AFM prototype 2B in combination with the large chamber SEM Zeiss Leo 982 (DSM 982). The size of the current prototype's AFM housing and coarse positioning stage should not be underestimated even for the case of the quite large sample chamber of the DSM 982. Before mounting the AFM, this guide should be read carefully, mistakes during the installation may lead to damage of the AFM or the SEM.

B.1. Preparation

The ASMEC UNAT-SEM indenter needs to be removed before mounting the AFM. The AFM will note fit into the SEM chamber with the ASMEC mounted, leading to a crash of the devices when the SEM chamber door closes.

All steps described here should be carried out having all components of the AFM turned off. The motor controllers of the coarse positioning stage and the high voltage amplifiers for the AFM piezos (HV unit) can become damaged during a "hot plugging" (connecting calbes with units on). The electronics of the SEM are not affected and can stay in normal operation mode.

If the SEM chamber is open for a long time (more than 30 minutes), the pumping time can take several hours. Before opening the chamber, all parts should be identified and prepared to keep the time of the mounting process short.

B.1.1. Cables

The AFM is designed for use in air and in vacuum. As there is only one set of cables, some of the cables for use in air are also needed for the in vacuum setup. Adapter cables are used to fit the vacuum feedthroughs of the SEM chamber. Figure B.1 shows a schematic of the cabling. A technical description of all components is given in the Instrumental Chapter, Section 2.2 "Description of the combined AFM/SEM instrument".

Special care needs to be taken for the parts which are used in air and in vacuum, they should be handled with gloves at all times (even for in air use). Photos of the cables are provided in Figure B.2, a complete list including the type of plugs used and a short description is given in Table B.1.
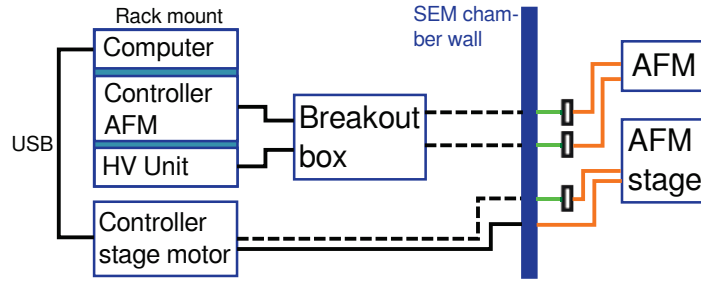
Fig. B.1.: Schematic of the AFM cabling. Black lines: These cables are always in use and always stay in air, dashed black line: used in air when the AFM is mounted in vacuum, green line: only used in vacuum and orange line: used in vacuum and in air.

Cable used for	Type	Plug controller	Plug AFM	Figure
Connect controller, HV unit and breakout box	Mini SMB	Mini SMB	Mini SMB	B.2a
Connect motor controllers and vacuum feedthroughs	multicore cable	D-sub or proprietary	LEMO	B.2b
Connect AFM and vacuum adapter or breakout	multicore cable	mini D-sub	D-sub	B.2c
Connect breakout and vacuum feedthroughs	multicore cable	D-sub	LEMO	B.2d
Connect vacuum feedthroughs and cables at the AFM	multicore cable	LEMO	D-sub	B.2e
Adapter for stepper motors for in air use	multicore cable	LEMO	LEMO	B.2f

Table B.1.: List of all cables and plugs used to connect the components of the AFM. The cables function, its type and the plugs (facing to controller, or facing to AFM) are listed.
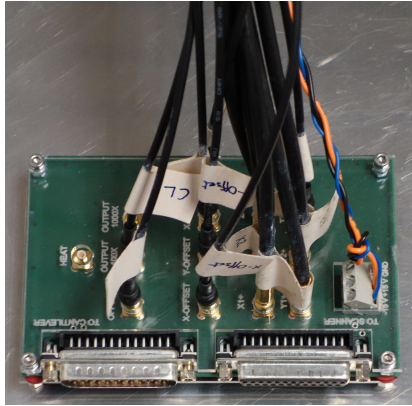
(a)
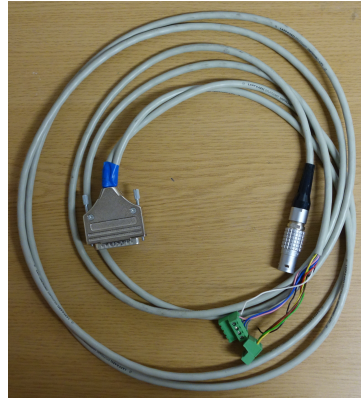
(b)

(c)

(d)

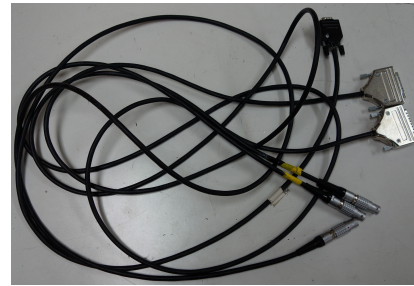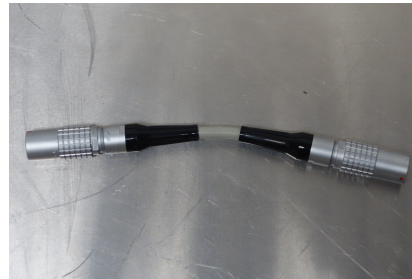**(e)**

(f)

Fig. B.2.: Photos of the cables used to connect the components of the AFM. In vacuum cables are indicated red, they always should be handled with gloves. **(a)** Mini SMB cables connecting controller, HV unit and breakout box, **(b)** cables driving stage motors, **(c)** AFM connectors, **(d)** in air extenders for in vacuum setup, **(e)** in vacuum extenders, **(f)** in air motor adapter. A detailed description is given in Table B.1
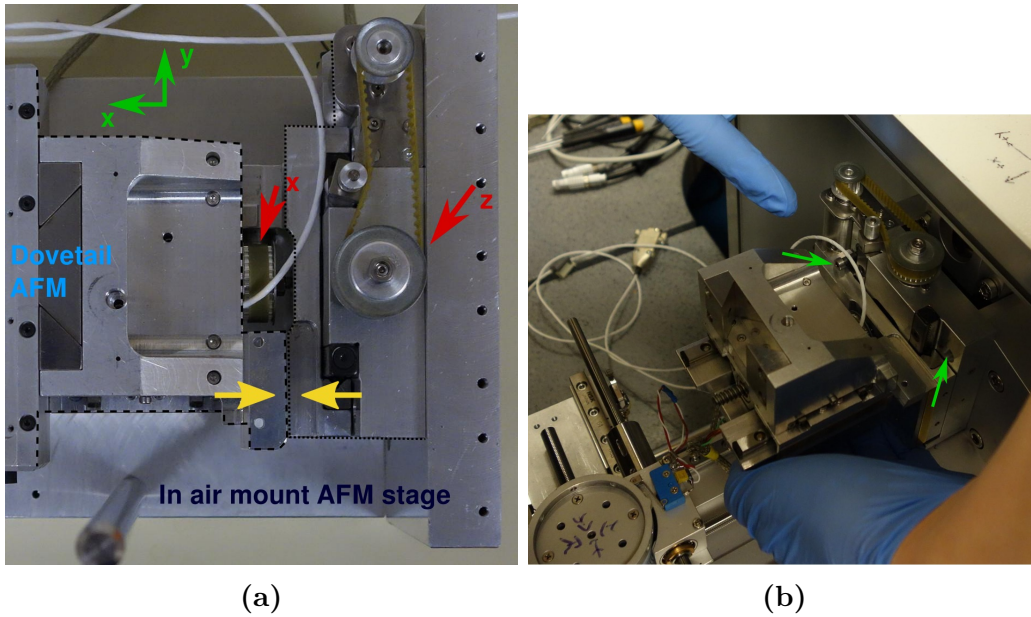
Fig. B.3.: (a) Position of the stage regarding the x-direction. The stage is mounted on a L-shaped in air holder. On the left side, the dovetail of the AFM is seen. The red arrows indicate the positions of the driving wheels, which can be turned to move the according axis. The yellow arrows show the mounting position of the x-axes of the stage. The edges of the left and right metal parts should overlap each other, as shown by the yellow arrows. **(b)** The stage is mounted by two screws (green arrows) on the SEM chamber door.

After the cables are ready, the AFM coarse positioning stage should be prepared for mounting inside of the Chamber.

B.1.2. Preparing the AFM stage

The z- and x-axes of the coarse positioning stage need to be retracted to certain positions before mounting. This can be done by manually spinning (always wear gloves!) the driving wheels with the motor controllers turned off. For the z-axis, the position of the stage should be about 1 mm above the minimum value, for the x-axis the position is shown by the yellow arrows in Figure B.3a.

The y-axis is only capable of moving about 2 mm in total, no adjustment is needed before the stage is mounted. Moving the y-axis manually will damage the piezo stick-slip motor. Handle this part of the stage with care! A schematic of the stage explaining the moving parts, axis and the working principle is given in Appendix D.

B.1.3. Preparing the AFM

To fit the AFM unit and cables into the SEM chamber, the Faraday cage of the SEM's SE Everhart-Thornley detector [125], [83, pp. 81] needs to be removed. The cables and connectors on the left side of the AFM may deform the Faraday cage. It is carefully unscrewed by touching the wires of the cage using gloves. The detector with the cage already removed is shown in Figure B.5b.

Pre-selecting AFM cantilevers is recommended in order to avoid re-opening the chamber and pumping. It should be already mentioned here, that plugging in the two cables of the AFM housing shown in Figure B.2c when it is already mounted on the coarse positioning stage may harm the sensitive piezo stick-slip motor of the x-axes. The two cables of the AFM housing should be plugged in before mounting the AFM.

B.2. Mounting stage and AFM

After preparing all parts, the chamber can be vented and opened to mount all components. First, the coarse positioning stage is fixed by hardened, vacuum suitable screws, see Figure B.3b.

After the stage is in place, the SEM stage support (a magnet holder) is mounted to reduce vibrations of the system. The magnet holder is not compatible with the ASMEC indenter and should be removed after unmounting the AFM. The position of the magnet holder must be set as shown in Figure B.4. A wrong position of the magnet holder may damage the SEM stage.
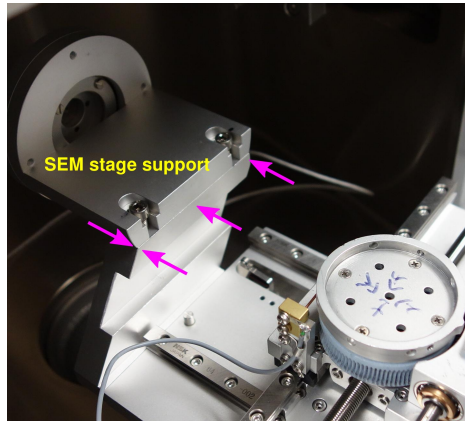

Fig. B.4.: Mounting of the SEM stage support. The edges of the metal parts of the stage mount and the SEM stage must overlap each other at the position indicated by the pink arrows.

B.3. Plugging in the cables

Cables and plugs are chosen in a way that they can not be confused when plugged in. There is one exception, and that is for the LEMO vacuum feedthroughs of the SEM chamber. The plug of the PI slip-stick motor and one plug of the AFM can be mistaken. Take great care to plug in the stage at the back of the SEM chamber, the AFM cables are plugged at the SEM door. The in air AFM extender cables are marked with a yellow tape (see Figure B.2d). The vacuum feedthroughs for the piezo motor, stepper motor and AFM are shown in Figure B.5. Don't plug the cables of the AFM unit when it is already mounted at the coarse positioning stage, it may damage the stick slip motor.

B.4. Final steps after mounting the AFM

After all cables are connected[1] and a cantilever is in place on the nose, the AFM is mounted on the coarse positioning stage as a final step. The dovetail is locked by using a 1.5 mm hex-wrench on the right side of the coarse positioning stage. When closing the chamber, make sure not to catch or damage any of the cables.

---

[1]The cables of the AFM unit need to be plugged in before mounting the AFM on the coarse positioning stage to prevent damage of the stage!
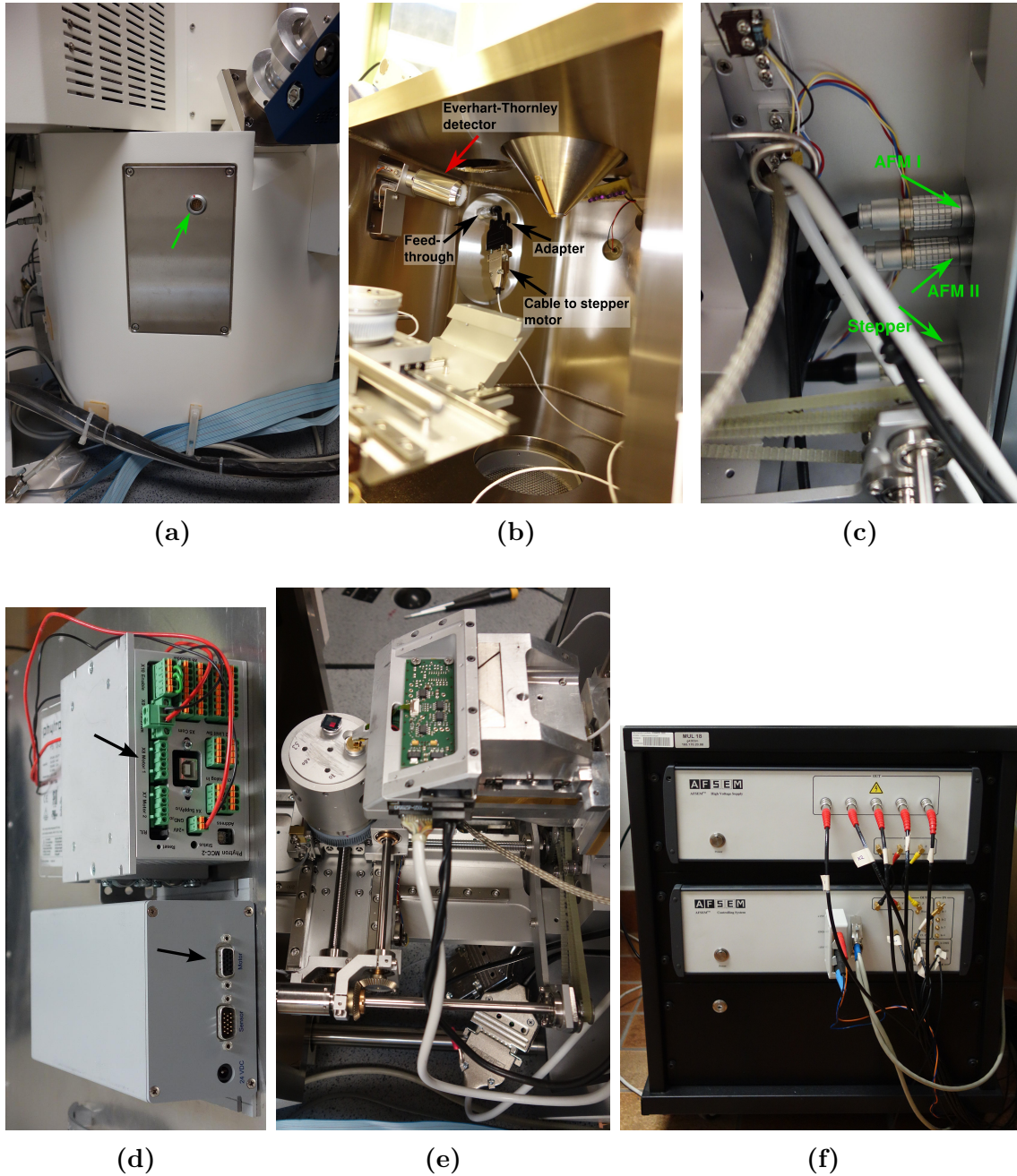
(a) **(b)** **(c)**

(d) **(e)** **(f)**

Fig. B.5.: Feedthroughs and plugs for the in vacuum setup. **(a)** Feedthrough of the piezo stick slip motor on the left back of the SEM chamber. **(b)** View at the stick slip cables and plugs inside the chamber. **(c)** Feedthroughs and plugs of the AFM and the stepper motors. **(d)** Motor controllers and plugs. **(e)** The setup is ready for closing the chamber. **(f)** All cables of the AFM controller and HV unit are connected, the system is ready.

C. Using the AFM in SEM: Step by step guidance

Before starting, read the Anfatec manual [126] provided with the AFM instrument. Also read Appendices B, D, A and Section 3.3.2. The following step-by-step instructions provide a guideline how to get first images with the new prototype:

1. Mount the instrument according to Appendix B. Wear gloves at all times.

2. Mount the sample, manually approach the AFM to the sample by using the coarse stage as shown in Figure B.3a. For a shorter sample-cantilever approach procedure, the distance between AFM cantilever and sample should be about one to two millimeters before closing the SEM chamber and pumping.

3. Test the system and cantilever signal according to Section 3.3.1.

4. Turn on the high voltage amplifier.

5. Set the excitation voltage of the tapping piezo to $0.1\,\mathrm{V}$.

6. Close the SEM chamber and pump the system.

7. After a short period of pumping, tune the cantilever in tapping mode, adjust the excitation voltage of the tapping piezo to a value to have a peak tapping amplitude of $20\,\mathrm{mV}$ to $30\,\mathrm{mV}$.

8. Wait until the SEM is ready (achieved vacuum). Keep everything turned on to avoid thermal drift caused by the electrical heating of the system.

9. Choose the AFM contact mode or tapping mode.

10. Set the setpoint to a very low value. For the tapping mode choose 95%.

11. Choose a spot for cantilever approach with the SEM. Avoid positions close to the area of interest.

12. Turn on the SEM, find your sample and cantilever by using the SEM stage and the AFM coarse stage at very low magnifications (10x to 50x).

13. Repeat alignment of sample and cantilever at a SEM magnification of 500x.

14. Keep the magnification of the SEM at 500x.

15. Set the AFM k_i gains for auto approach to 500.

16. Set the AFM controller gains. Use 250 for the k_i-value and 500 for the k_p-value.

17. Set the AFM scanning range to $1\,\mu m$ and the scanning speed to $0.1\,s^{-1}$.

18. Approach the AFM cantilever to the sample surface by focusing the SEM electron beam on the AFM cantilever and the sample surface. Count the clicks of the SEM focus wheel. One click of the SEM focus wheel corresponds to 50 steps of the AFM coarse stage in z-direction.

19. Check your cantilever position every 500 to 1000 steps of the AFM coarse stage with the help of the SEM.

20. After reaching a distance between AFM cantilever and sample surface of about 1000 stage steps (that is 20 clicks of the SEM focus wheel), use the automatic approach routine of the AFM software. For the case of a too slow or too fast auto approach, hit the ESC-button to abort and re-tune the setpoint and k_i values.

21. After approach, check the z-drift of the system. If the drift is higher than $1\,nm/s$, wait a few minutes for the coarse stage to stabilize, correct the coarse z-position using the AFM stage from time to time to avoid a cantilever crash caused by the drift.

22. Check the interaction of AFM cantilever and surface with the AFM controller software. Adjust the setpoint to have a value of $5\,nm$ to $15\,nm$ cantilever-surface interaction.

23. Start scanning. Adjust the gains, scan range and scanning speed. Adjust the setpoint and gains for optimal imaging.

D. The coarse positioning AFM stage

D.1. Stage hardware

With the AFM inside of the SEM a coarse positioning stage was built to perform the following tasks (axes, total movement and resolution given in brackets):

- **Coarse approach (z):** Move or retract the scanner to/from the surface ($L_z = 15\,mm/\Delta L_z = 0.5\mu m$).

- **Parking position (x):** Retract the scanner from the SEM electron beam to a parking position for standard SEM operation. Parking the AFM can be necessary to improve imaging with the SE detector [83, pp. 81] or for special SEM equipment like a EBSD detector or a four-quadrant BSE detector. ($L_x = 25\,mm/\Delta L_x = 0.5\mu m$).

- **SEM beam alignment (x, y):** The tip of the AFM cantilever needs to be aligned to the SEM electron beam for simultaneous AFM/SEM imaging. ($L_y = 2\,mm/\Delta L_y = 1.0\mu m$)

Components and working principle

The stage was custom built to fit the needs for the AFM in combination with the large chamber SEM Zeiss Leo DSM 982. An overview is given in Figure D.1 to show the working principle and moving parts linked to the axis directions.

The x- and z-stage are driven by vacuum compatible step motors from Phytron (Groebenzell, Germany) [127]. The y-axis is driven by a NEXAKT Piezowalk motor from PI (Karlsruhe, Germany) [128], which also is vacuum compatible. To be flexible according to different sample heights and to be able to park the AFM far away from the SEM electron beam, the x- and z-axes are driven by step-motors. The y axes is only needed for a fine alignment of the AFM cantilever with SEM beam and therefore a compact piezo stick slip motor is sufficient for this task.

Vacuum compatibility

All electrical and mechanical parts were chosen for vacuum compatibility. The screw holes and voids are vented to prevent virtual leaks. An ultra high vacuum compatible grease was used for the moving parts.
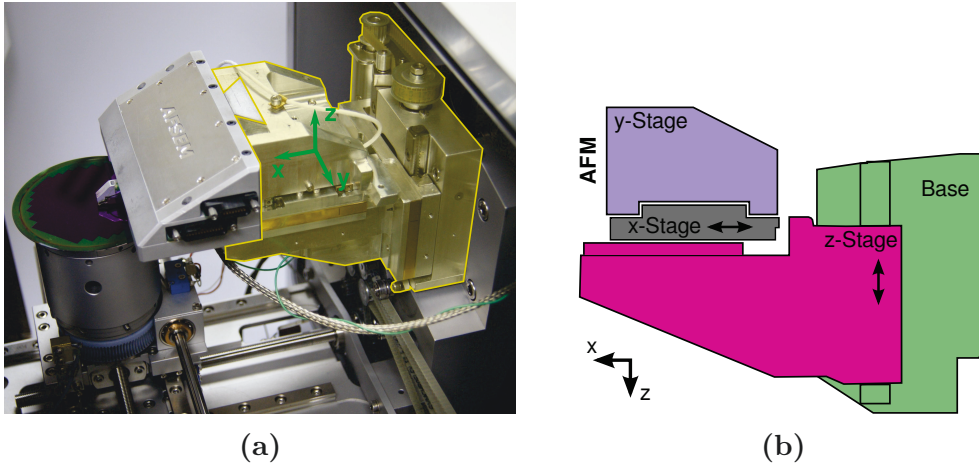
D. The coarse positioning AFM stage

Fig. D.1.: Photo and schematic of the coarse positioning stage
to show the working principle. **(a)** Photo with highlighted stage
mounted on the z stage of the SEM goniometer. **(b)** Schematic of
the coarse positioning stage. Handle the turquoise part of the stage,
driven by the piezo motor, with care.

D.2. Stage software

The stage control software is written in Python [129], a modern, platform independent
programming language. The step width of the x- and y-axis are adjusted by a scroll
bar. Two buttons, one for coarse movements and one fine alignment are available.
A screenshot of the software interface is shown in Figure D.2a. The z-axes of the
coarse stage is controlled by the Anfatec [46] AFM controller software. Both axes can
be deactivated. In the case of the stepper motors, the stepping motor end phase is
completely turned off to minimize electromagnetic distortions.
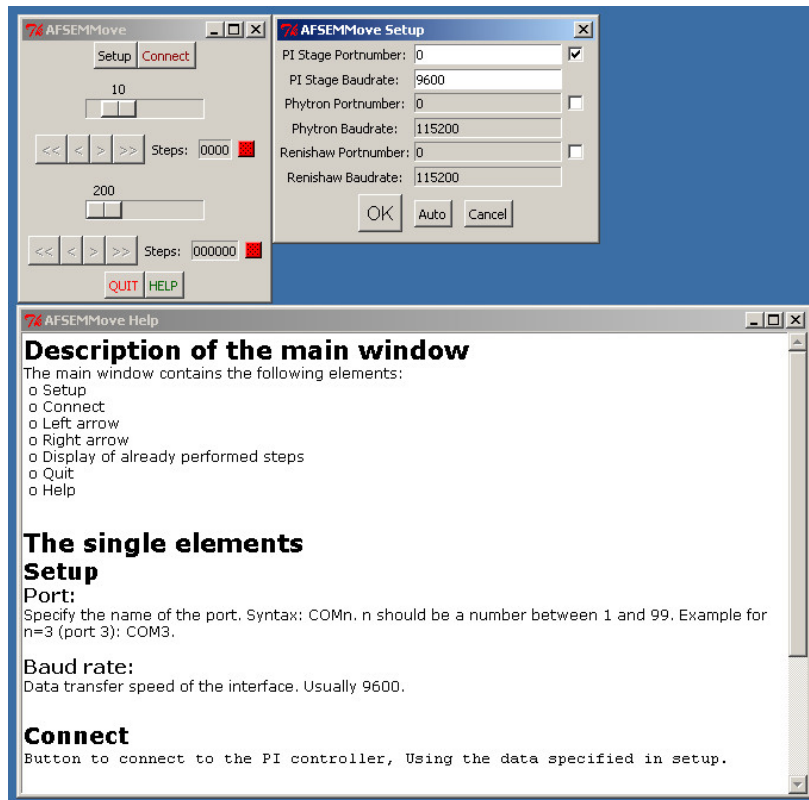
(a)
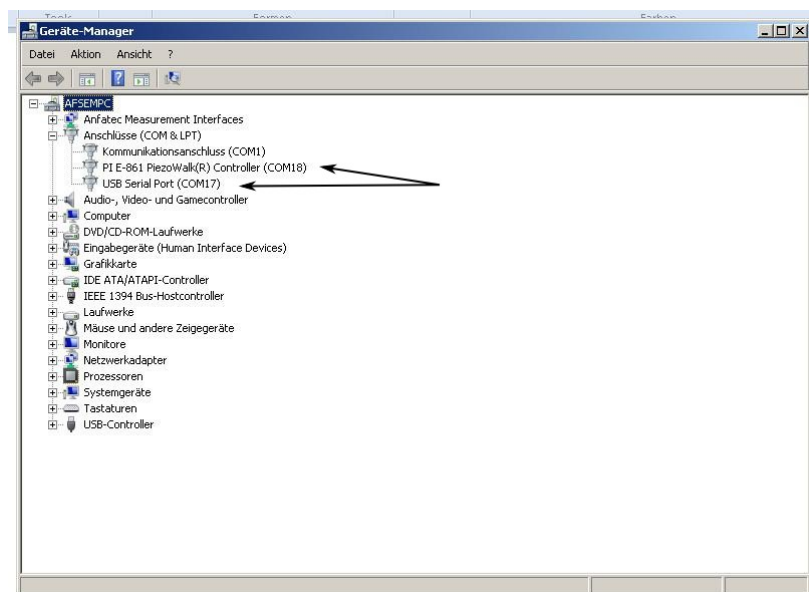
(b)

Fig. D.2.: Stage control software: **(a)** interface **(b)** windows hardware configuration to find out the port number of the motor's serial ports.

E. Software used to create this work

This work was created by entirely using free open source software (OSS). Table E.1 enlists details about the software worked with.

Name	Function	License
Debian Linux[a]	Unix-like operating system and Linux distribution	DFSG-compliant[b]
Tex Live[c]	Software distribution for the LaTeX typesetting system	LaTeXProject Public License and GPL[d]
Gnuplot	Graphing utility	Gnuplot OSS license
Inkscape[e]	Vector graphics editor	GPL
Gimp[f]	Image manipulation program	GPL
Image Magick[g]	Software suite for displaying, converting and manipulating images	Apache 2.0 License
Blender[h]	3D computer graphics software	GPL

Table E.1.: OSS used to create this work.

[a]https://www.debian.org
[b]Debian Free Software Guidelines
[c]http://www.tug.org/texlive/
[d]GNU General Public License, https://gnu.org/licenses/gpl.html
[e]https://inkscape.org
[f]http://www.gimp.org/
[g]http://www.imagemagick.org/
[h]http://www.blender.org/

Bibliography

[1] G. Gottstein. *Physikalische Grundlagen der Materialkunde.* Springer Berlin Heidelberg New York, 2007.

[2] J. Weertmann and J. R. Weertmann. *Elementary Dislocation Theory.* Oxford University Press, 1992.

[3] D. Hull and J. Bacon. *Introduction to Dislocations.* Butterworth-Heinemann, 2011.

[4] F.C. Frank and W.T. Read Jr. "Multiplication processes for slow moving dislocations [7]". *Physical Review* 79.4 (1950), pp. 722–723. DOI: `10.1103/PhysRev.79.722`.

[5] N. Thompson. "Dislocation nodes in face-centred cubic lattices". *Proceedings of the Physical Society. Section B* 66.6 (1953), pp. 481–492. DOI: `10.1088/0370-1301/66/6/304`.

[6] E.O. Hall. "The deformation and ageing of mild steel: III Discussion of results". *Proceedings of the Physical Society. Section B* 64.9 (1951), pp. 747–753. DOI: `10.1088/0370-1301/64/9/303`.

[7] N.J. Petch. "The Cleavage Strength of Polycrystals". *J. Iron Steel Inst. London* 173 (1953), 25–28.

[8] W.D. Nix and H. Gao. "Indentation size effects in crystalline materials: A law for strain gradient plasticity". *Journal of the Mechanics and Physics of Solids* 46.3 (1998), pp. 411–425.

[9] M.D. Uchic, D.M. Dimiduk, J.N. Florando, and W.D. Nix. "Sample dimensions influence strength and crystal plasticity". *Science* 305.5686 (2004), pp. 986–989. DOI: `10.1126/science.1098993`.

[10] J. De La Figuera, M.A. Gonzalez, R. Garcia-Martinez, J.M. Rojo, O.S. Hernan, A.L. Vazquez De Parga, and R. Miranda. "STM characterization of extended dislocation configurations in Au(001)". *Physical Review B - Condensed Matter and Materials Physics* 58.3 (1998), pp. 1169–1172.

[11] K. Lueders and R.O. Pohl, eds. *Pohls Einfuehrung in die Physik: Elektrizitaetslehre und Optik.* Springer-Verlag Berlin Heidelberg, 2006.

[12] M. Knoll and E. Ruska. "Das Elektronenmikroskop". *Zeitschrift für Physik* 78.5-6 (1932), pp. 318–339. DOI: `10.1007/BF01342199`.

[13] M. Ardenne. "Das Elektronen-Rastermikroskop - Theoretische Grundlagen". *Zeitschrift für Physik* 109.9-10 (1938), pp. 553–572. DOI: `10.1007/BF01341584`.

[14] G. Binnig and H. Rohrer. "Scanning tunneling microscopy". *Surface Science* 126.1-3 (1983), pp. 236–244. DOI: `10.1016/0039-6028(83)90716-1`.

[15] G. Binnig, C.F. Quate, and Ch. Gerber. "Atomic force microscope". *Physical Review Letters* 56.9 (1986), pp. 930–933. DOI: `10.1103/PhysRevLett.56.930`.

[16] G. Meyer and N.M. Amer. "Novel optical approach to atomic force microscopy". *Applied Physics Letters* 53.12 (1988), pp. 1045–1047. DOI: `10.1063/1.100061`.

[17] C.S. Smith. "Piezoresistance effect in germanium and silicon". *Physical Review* 94.1 (1954), pp. 42–49. DOI: `10.1103/PhysRev.94.42`.

[18] K. Hoffmann. *An Introduction to Measurements using Strain Gages*. HBM, Pfungstadt, 1987.

[19] G. Binnig, H. Rohrer, Ch. Gerber, and E. Weibel. "Surface Studies by Scanning Tunneling Microscopy". *Phys. Rev. Lett.* 49 (1 July 1982), pp. 57–61. DOI: `10.1103/PhysRevLett.49.57`.

[20] L. Vasquez, A. Bartolome, R. Garcia, A. Buendia, and A.M. Baro. "Combination of a scanning tunneling microscope with a scanning electron microscope". *Review of Scientific Instruments* 59.8 (1988), pp. 1286–1289. DOI: `10.1063/1.1139710`.

[21] A.V. Ermakov and E.L. Garfunkel. "A novel AFM/STM/SEM system". *Review of Scientific Instruments* 65.9 (1994), pp. 2853–2854. DOI: `10.1063/1.1144627`.

[22] U. Stahl, C.W. Yuan, A.L. De Lozanne, and M. Tortonese. "Atomic force microscope using piezoresistive cantilevers and combined with a scanning electron microscope". *Applied Physics Letters* 65.22 (1994), pp. 2878–2880. DOI: `10.1063/1.113030`.

[23] J. A. Harley. "Advances in piezoresistive probes for atomic force microscopy". PhD thesis. Department of mechanical engineering of Stanford university, 2000.

[24] *Homepage of Topometrix*. Topometrix. URL: `http://elchem.kaist.ac.kr/jhkwak/topometrixweb/topohome.htm`.

[25] A. Emundts, P. Coenen, G. Pirug, B. Voigtlaender, H.P. Bonzel, and P. Wynblatt. "Combination of a Besocke-type scanning tunneling microscope with a scanning electron microscope". *Review of Scientific Instruments* 72.9 (2001), pp. 3546–3551. DOI: `10.1063/1.1392341`.

[26] K. Besocke. "An easily operable scanning tunneling microscope". *Surface Science* 181.1-2 (1987), pp. 145–153. DOI: `10.1016/0039-6028(87)90151-8`.

[27] S. Bauerdick, C. Burkhardt, R. Rudorf, W. Barth, V. Bucher, and W. Nisch. "In-situ monitoring of electron beam induced deposition by atomic force microscopy in a scanning electron microscope". *Microelectronic Engineering* 67-68 (2003). Ed. by Rothuizen H. Staufer U. Vettig P. Brugger J. Gobrecht J., pp. 963–969. DOI: `10.1016/S0167-9317(03)00160-6`.

[28]   *Homepage Kleindiek Nanotechnik.* Kleindiek Nanotechnik GmbH. URL: http://www.nanotechnik.com.

[29]   E. Celik and E. Madenci. "Characterization of metallic nanowires by combining atomic force microscope (AFM) and scanning electron microscope (SEM)". Vol. 1. Anaheim, CA, 2010, pp. 13–16.

[30]   W.F. Oele, J.W.J. Kerssemakers, and J.Th.M. De Hosson. "In situ generation and atomic scale imaging of slip traces with atomic force microscopy". *Review of Scientific Instruments* 68.12 (1997), pp. 4492–4497. DOI: 10.1063/1.1148419.

[31]   P. Franciosi, L.T. Le, G. Monnet, C. Kahloun, and M.-H. Chavanne. "Investigation of slip system activity in iron at room temperature by SEM and AFM insitu tensile and compression tests of iron single crystals". *International Journal of Plasticity* 65 (2014), pp. 226–249. DOI: 10.1016/j.ijplas.2014.09.008.

[32]   C. Kahloun, L.T. Le, G. Monnet, M.-H. Chavanne, E. Ait, and P. Franciosi. "Topological analysis of 1 1 0 slip in an alpha-iron crystal from in situ atomic force microscopy". *Acta Materialia* 61.17 (2013), pp. 6459–6465. DOI: 10.1016/j.actamat.2013.07.023.

[33]   C. Coupeau, J.C. Girard, J. Grilhe, and J. Lepinoux. "Statistical analysis of insitu slip lines by atomic force microscopy observations". *Philosophical Magazine A: Physics of Condensed Matter, Structure, Defects and Mechanical Properties* 76.6 (1997), pp. 1139–1152.

[34]   F. Foucher and C. Coupeau. "Effect of the dislocation emergence on the mechanical behavior of coated materials: Elastic energy relaxation or adhesion modification". *Surface and Coatings Technology* 202.4-7 (2007), pp. 1094–1097. DOI: 10.1016/j.surfcoat.2007.07.106.

[35]   C. Coupeau, J. Grilhe J., E. Dion, L.D. De Morais, and J. Colin. "Evidence of vacuum between buckled films and their substrates". *Thin Solid Films* 518.18 (2010), pp. 5233–5236. DOI: 10.1016/j.tsf.2010.04.026.

[36]   K. Fukushima, D. Saya, and H. Kawakatsu. "Development of a versatile atomic force microscope within a scanning electron microscope". *Japanese Journal of Applied Physics, Part 1: Regular Papers and Short Notes and Review Papers* 39.6 B (2000), pp. 3747–3749.

[37]   K. Fukushima, S. Kawai, D. Saya, and H. Kawakatsu. "Measurement of mechanical properties of three-dimensional nanometric objects by an atomic force microscope incorporated in a scanning electron microscope". *Review of Scientific Instruments* 73.7 (2002), p. 2647. DOI: 10.1063/1.1488150.

[38]   C. Motz, T. Schoeberl, and R. Pippan. "Mechanical properties of micro-sized copper bending beams machined by the focused ion beam technique". *Acta Materialia* 53.15 (2005), pp. 4269–4279. DOI: 10.1016/j.actamat.2005.05.036.

[39] P. Egberts, T. Filleter, and R. Bennewitz. "A kelvin probe force microscopy of charged indentation-induced dislocation structures in KBr". *Nanotechnology* 20.26 (2009), p. 7. DOI: 10.1088/0957-4484/20/26/264005.

[40] T. Filleter, S. Maier, and R. Bennewitz. "Atomic-scale yield and dislocation nucleation in KBr". *Physical Review B - Condensed Matter and Materials Physics* 73.15 (2006), p. 10. DOI: 10.1103/PhysRevB.73.155433.

[41] K.A. Nibur, D.F. Bahr, and B.P. Somerday. "Hydrogen effects on dislocation activity in austenitic stainless steel". *Acta Materialia* 54.10 (2006), pp. 2677–2684. DOI: 10.1016/j.actamat.2006.02.007.

[42] Y.K. Yong, S.S. Aphale, and S.O.R. Moheimani. "Design, identification, and control of a flexure-based XY stage for fast nanoscale positioning". *IEEE Transactions on Nanotechnology* 8.1 (2009), pp. 46–54. DOI: 10.1109/TNANO.2008.2005829.

[43] *Homepage GETec.* GETec KG (Vienna, Austria). 2015. URL: http://www.getec-afm.com/.

[44] *Homepage SCL-Sensor.Tech.* SCL-Sensor.Tech. Fabrication GmbH (Vienna, Austria). 2015. URL: http://www.sclsensortech.com/.

[45] T.R. Rodriguez and R. Garcia. "Theory of Q control in atomic force microscopy". *Applied Physics Letters* 82.26 (2003), pp. 4821–4823. DOI: 10.1063/1.1584790.

[46] *Homepage Anfatec Instruments.* Anfatec Instruments AG (Oelsnitz, Germany). URL: http://www.anfatec.de/.

[47] *Homepage Techproject.* Techproject (Vienna, Austria). 2015. URL: http://www.techproject.at/.

[48] T. Ando, N. Kodera, E. Takai, D. Maruyama, K. Saito, and A. Toda. "A high-speed atomic force microscope for studying biological macromolecules". *Proceedings of the National Academy of Sciences of the United States of America* 98.22 (2001), pp. 12468–12472. DOI: 10.1073/pnas.211400898.

[49] M. Leitner, G.E. Fantner, E.J. Fantner, K. Ivanova, T. Ivanov, I. Rangelow, A. Ebner, M. Rangl, J. Tang, and P. Hinterdorfer. "Increased imaging speed and force sensitivity for bio-applications with small cantilevers using a conventional AFM setup". *Micron* 43.12 (2012), pp. 1399–1407. DOI: 10.1016/j.micron.2012.05.007.

[50] M.W. Fairbairn, S.O.R. Moheimani, and A.J. Fleming. "Q control of an atomic force microscope microcantilever: A sensorless approach". *Journal of Microelectromechanical Systems* 20.6 (2011), pp. 1372–1381. DOI: 10.1109/JMEMS.2011.2168809.

[51] D.S. Gianola, A. Sedlmayr, R. Mnig, C.A. Volkert, R.C. Major, E. Cyrankowski, S.A.S. Asif, O.L. Warren, and O. Kraft. "In situ nanomechanical testing in focused ion beam and scanning electron microscopes". *Review of Scientific Instruments* 82.6 (June 2011), p. 12. DOI: 10.1063/1.3595423.

[52] *Homepage Kammrath & Weiss GmbH*. Kammrath & Weiss GmbH. URL: http://www.kammrath-weiss.com/en/.

[53] *Homepage Accurion*. Accurion GmbH (Goettingen, Germany). 2015. URL: http://accurion.com/active-vibration-isolation-technology.

[54] Z. Wang, H. Bei, E.P. George, and G.M. Pharr. "Influences of surface preparation on nanoindentation pop-in in single-crystal Mo". *Scripta Materialia* 65.6 (2011), pp. 469–472. DOI: 10.1016/j.scriptamat.2011.05.030.

[55] M. Haghshenas and R.J. Klassen. "Assessment of the depth dependence of the indentation stress during constant strain rate nanoindentation of 70/30 brass". *Materials Science and Engineering A* 572 (2013), pp. 91–97. DOI: 10.1016/j.msea.2013.02.009.

[56] W.W. Gerberich, S.K. Venkataraman, H. Huang, S.E. Harvey, and D.L. Kohlstedt. "The injection of plasticity by millinewton contacts". *Acta Metallurgica Et Materialia* 43.4 (1995), pp. 1569–1576. DOI: 10.1016/0956-7151(94)00351-H.

[57] P. Qiu and C. Leygraf. "Initial oxidation of brass induced by humidified air". *Applied Surface Science* 258.3 (2011), pp. 1235–1241. DOI: 10.1016/j.apsusc.2011.09.080.

[58] S.C. Chang and H.C. Chen. "The determination of F.C.C. crystal orientation by indentation". *Acta Metallurgica Et Materialia* 43.6 (1995), pp. 2501–2505.

[59] J.A. Venables and C.J. Harland. "Electron Back-Scattering Patterns - a New Technique for Obtaining Crystallographic Information in the Scanning Electron Microscope." *Phil Mag* 27.5 (1973), pp. 1193–1200.

[60] *Homepage Rigaku Smartlab*. Rigaku Corporation. 2015. URL: http://www.rigaku.com/de/products/xrd/smartlab.

[61] L. Spiess, R. Schwarzer, H. Behnken, and G. Teichert. *Moderne Roentgenbeugung, Roentgendiffraktometrie fuer Materialwissenschaftler, Physiker und Chemiker*. Teubner, 2005.

[62] J. Brentano. "Focussing method of crystal powder analysis by x-rays". *Proceedings of the Physical Society of London* 37.1 (1924), pp. 184–193. DOI: 10.1088/1478-7814/37/1/326.

[63] W. Borchardt-Ott and Heidrun Sowa. *Kristallographie, Eine Einfuehrung fuer Naturwissenschaftler*. Springer, 2013.

[64] W. Kleber, H.J. Bautsch, and J Bohm. *Einfuehrung in die Kristallographie*. 19th ed. Oldenbourg, 2010.

[65] Y. Gaillard, C. Tromas, and J. Woirgard. "Study of the dislocation structure involved in a nanoindentation test by atomic force microscopy and controlled chemical etching". *Acta Materialia* 51.4 (2003), pp. 1059–1065. DOI: 10.1016/S1359-6454(02)00509-8.

[66] D. Kiener, R. Pippan, C. Motz, and H. Kreuzer. "Microstructural evolution of the deformed volume beneath microindents in tungsten and copper". *Acta Materialia* 54.10 (2006), pp. 2801–2811. DOI: 10.1016/j.actamat.2006.02.024.

[67] M. Rester, C. Motz, and R. Pippan. "Microstructural investigation of the volume beneath nanoindentations in copper". *Acta Materialia* 55.19 (2007), pp. 6427–6435. DOI: 10.1016/j.actamat.2007.08.001.

[68] M.J. Cordill. "Deformation Mechanisms of Single Crystals at the Nanoscale". PhD thesis. University of Minnesota, 2007.

[69] W.W. Gerberich, M.J. Cordill, W.M. Mook, N.R. Moody, C.R. Perrey, C.B. Carter, R. Mukherjee, and S.L. Girshick. "A boundary constraint energy balance criterion for small volume deformation". *Acta Materialia* 53.8 (2005), pp. 2215–2229. DOI: 10.1016/j.actamat.2005.01.028.

[70] Y.M. Soifer, A. Verdyan, M. Kazakevich, and E. Rabkin. "Edge effect during nanoindentation of thin copper films". *Materials Letters* 59.11 (2005), pp. 1434–1438. DOI: 10.1016/j.matlet.2004.08.043.

[71] R.E. Miller, L.E. Shilkrot, and W.A. Curtin. "A coupled atomistics and discrete dislocation plasticity simulation of nanoindentation into single crystal thin films". *Acta Materialia* 52.2 (2004), pp. 271–284. DOI: 10.1016/j.actamat.2003.09.011.

[72] G. Moser, H. Felber, B. Rashkova, P.J. Imrich, C. Kirchlechner, W. Grosinger, C. Motz, G. Dehm, and D. Kiener. "Sample preparation by metallography and focused ion beam for nanomechanical testing [Probenfertigung mittels Metallographie und lonenmikroskopie für nanomechanische Experimente]". *Praktische Metallographie/Practical Metallography* 49.6 (2012), pp. 343–355.

[73] C. Kirchlechner, W. Grosinger, M.W. Kapp, P.J. Imrich, J.-S. Micha, O. Ulrich, J. Keckes, G. Dehm, and C. Motz. "Investigation of reversible plasticity in a micron-sized, single crystalline copper bending beam by X-ray Microlaue diffraction". *Philosophical Magazine* 92.25-27 (2012), pp. 3231–3242. DOI: 10.1080/14786435.2012.669067.

[74] K.S. Ng and A.H.W. Ngan. "Deformation of micron-sized aluminium bi-crystal pillars". *Philosophical Magazine* 89.33 (2009), pp. 3013–3026. DOI: 10.1080/14786430903164614.

[75] P.J. Imrich, C. Kirchlechner, C. Motz, and G. Dehm. "Differences in deformation behavior of bicrystalline Cu micropillars containing a twin boundary or a large-angle grain boundary". *Acta Materialia* 73 (2014), pp. 240–250. DOI: 10.1016/j.actamat.2014.04.022.

[76] B. Graffel, F. Mueller, A.-D. Mueller, and M. Hietschold. "Feedforward correction of nonlinearities in piezoelectric scanner constructions and its experimental verification". *Review of Scientific Instruments* 78.5 (2007), pp. 537061–537066. DOI: 10.1063/1.2736786.

[77] D. Necas and P. Klapetek. "Gwyddion: An open-source software for SPM data analysis". *Central European Journal of Physics* 10.1 (2012), pp. 181–188. DOI: 10.2478/s11534-011-0096-2.

[78] *Gwyddion: A software for AFM data visualization and analysis.* URL: http://gwyddion.net/.

[79] J.S. Villarrubia. "Morphological estimation of tip geometry for scanned probe microscopy". *Surface Science* 321.3 (1994), pp. 287–300. DOI: 10.1016/0039-6028(94)90194-5.

[80] P. West. *Introduction to Atomic Force Microscopy.* Paulwestphd.com, 2006.

[81] D. Kramer, H. Huang, M. Kriese, J. Robach, J. Nelson, A. Wright, D. Bahr, and W.W. Gerberich. "Yield strength predictions from the plastic zone around nanocontacts". *Acta Materialia* 47.1 (1998), pp. 333–343.

[82] J.B.F. Cripps and H. Sang. "Stereo height measurements in scanning electron microscopy". *Review of Scientific Instruments* 41.12 (1970), pp. 1825–1827. DOI: 10.1063/1.1684419.

[83] L. Reimer and G. Pfefferkorn. *Raster-Elektronenmikroskopie.* Springer, 1973.

[84] P. Klapetek, D. Necas, and C. Anderson. *Gwyddion user guide.*

[85] J. Thornton. *Scanning Probe Microscopy Training Notebook.* Digital Instruments, 1998.

[86] K. Durst, B. Backes, O. Franke, and M. Goeken. "Indentation size effect in metallic materials: Modeling strength from pop-in to macroscopic hardness using geometrically necessary dislocations". *Acta Materialia* 54.9 (2006), pp. 2547–2555. DOI: 10.1016/j.actamat.2006.01.036.

[87] S. Shim, H. Bei, E.P. George, and G.M. Pharr. "A different type of indentation size effect". *Scripta Materialia* 59.10 (2008), pp. 1095 –1098. DOI: http://dx.doi.org/10.1016/j.scriptamat.2008.07.026.

[88] M.J. Cordill, M.D. Chambers, M.S. Lund, D.M. Hallman, C.R. Perrey, C.B. Carter, A. Bapat, U. Kortshagen, and W.W. Gerberich. "Plasticity responses in ultra-small confined cubes and films". *Acta Materialia* 54.17 (2006), pp. 4515–4523. DOI: 10.1016/j.actamat.2006.05.037.

[89] S.G. Corcoran, R.J. Colton, E.T. Lilleodden, and W.W. Gerberich. "Anomalous plastic deformation at surfaces: Nanoindentation of gold single crystals". *Physical Review B - Condensed Matter and Materials Physics* 55.24 (1997), R16057–R16060.

[90] M.J. Cordill, W.M. Mook, A.K. Nair, D. Farkas, and W.W. Gerberich. "Novel routes to nanocrystalline mechanical characterization". *JOM* 59.9 (2007), pp. 59–61. DOI: 10.1007/s11837-007-0119-z.

[91] D.F. Bahr, D.E. Kramer, and W.W. Gerberich. "Non-linear deformation mechanisms during nanoindentation". *Acta Materialia* 46.10 (1998), pp. 3605–3617.

[92] N.A. Fleck, G.M. Muller, M.F. Ashby, and J.W. Hutchinson. "Strain gradient plasticity: Theory and experiment". *Acta Metallurgica Et Materialia* 42.2 (1994), pp. 475–487.

[93] J.-Y. Kim, B.-W. Lee, D.T. Read, and D. Kwon. "Influence of tip bluntness on the size-dependent nanoindentation hardness". *Scripta Materialia* 52.5 (2005), pp. 353–358. DOI: 10.1016/j.scriptamat.2004.10.036.

[94] R.K. Abu Al-Rub. "Prediction of micro and nanoindentation size effect from conical or pyramidal indentation". *Mechanics of Materials* 39.8 (2007), pp. 787–802. DOI: 10.1016/j.mechmat.2007.02.001.

[95] D. Bhattacharyya, N.A. Mara, P. Dickerson, R.G. Hoagland, and A. Misra. "Compressive flow behavior of Al–TiN multilayers at nanometer scale layer thickness". *Acta Materialia* 59.10 (2011), pp. 3804 –3816. DOI: http://dx.doi.org/10.1016/j.actamat.2011.02.036.

[96] Vinay Sriram, Jenn-Ming Yang, Jia Ye, and Andrew M. Minor. "In-situ metrology and testing of nanotwinned copper pillars for potential air gap applications". *Microelectronic Engineering* 87.11 (2010), pp. 2046 –2049. DOI: http://dx.doi.org/10.1016/j.mee.2010.04.019.

[97] A.K. Nair, M.J. Cordill, D. Farkas, and W.W. Gerberich. "Nanoindentation of thin films: Simulations and experiments". *Journal of Materials Research* 24.3 (2009), pp. 1135–1141. DOI: 10.1557/jmr.2009.0136.

[98] A.C. Fischer-Cripps. *Nanoindentation*. Third Edition. Springer New York Dordrecht Heidelberg London, 2011. DOI: DOI10.1007/978-1-4419-9872-9.

[99] T. Chudoba, P. Schwaller, R. Rabe, J.-M. Breguet, and J. Michler. "Comparison of nanoindentation results obtained with Berkovich and cube-corner indenters". *Philosophical Magazine* 86.33-35 SPEC. ISSUE (2006), pp. 5265–5283. DOI: 10.1080/14786430600746424.

[100] A.K. Srivastava. "Orientation, microstructure and pile-up effects on nanoindentation measurements of fcc and bcc metals". MA thesis. University of North Texas, 2008.

[101] M. Rester, C. Motz, and R. Pippan. "Indentation across size scales - A survey of indentation-induced plastic zones in copper 1 1 1 single crystals". *Scripta Materialia* 59.7 (2008), pp. 742–745. DOI: 10.1016/j.scriptamat.2008.06.003.

[102]   N. Zaafarani, D. Raabe, F. Roters, and S. Zaefferer. "On the origin of deformation-induced rotation patterns below nanoindents". *Acta Materialia* 56.1 (2008), pp. 31–42. DOI: 10.1016/j.actamat.2007.09.001.

[103]   W. Zielinski, H. Huang, and W.W. Gerberich. "Microscopy and microindentation mechanics of single crystal Fe-3 wt.%Si: Part II. TEM of the indentation plastic zone". *Journal of Materials Research* 8.6 (1993), pp. 1300–1310.

[104]   D. Tabor. *The Hardness of Metals.* Oxford Classic Texts in the Physical Sciences, 1951.

[105]   D. G. Coates. "Kikuchi-like reflection patterns obtained with the scanning electron microscope". *Philosophical Magazine* 16.144 (1967), pp. 1179–1184. DOI: 10.1080/14786436708229968. eprint: http://dx.doi.org/10.1080/14786436708229968.

[106]   A.J. Wilkinson and P.B. Hirsch. "Electron diffraction based techniques in scanning electron microscopy of bulk materials". *Micron* 28.4 (1997), pp. 279–308. DOI: 10.1016/S0968-4328(97)00032-2.

[107]   T. Kremmer. "Ermuedungseigenschaften und Mikrostrukturevolution von mikro- und nanokristallinen Mikrobiegeproben". MA thesis. Department Materials Physics at the University of Leoben, 2012.

[108]   A.T. Jennings, J. Li, and J.R. Greer. "Emergence of strain-rate sensitivity in Cu nanopillars: Transition from dislocation multiplication to dislocation nucleation". *Acta Materialia* 59.14 (2011), pp. 5627–5637. DOI: 10.1016/j.actamat.2011.05.038.

[109]   *A Practical Guide to SPM Scanning Probe Microscopy.* Veeco Instruments Inc. 2005.

[110]   A.E. Vladar, M.T. Postek, and R. Vane. "Proceedings of Active monitoring and control of electron beam induced contamination". *Metrology, Inspection, and Process Control for Microlithography XV.* Ed. by Sullivan N.T. Vol. 4344. Santa Clara, CA, 2001, pp. 835–843. DOI: 10.1117/12.436724.

[111]   A.J.V. Griffiths and T. Walther. "Quantification of carbon contamination under electron beam irradiation in a scanning transmission electron microscope and its suppression by plasma cleaning". *Journal of Physics: Conference Series* 241.012017 (2010), p. 5. DOI: 10.1088/1742-6596/241/1/012017.

[112]   N. Sullivan, T. Mai, S. Bowdoin, and R. Vane. "A study of the effectiveness of the removal of hydrocarbon contamination by oxidative cleaning inside the SEM". *Microscopy and Microanalysis* 8.SUPPL. 2 (2002), pp. 720–721.

[113]   C. Kirchlechner. "Plasticity at the Micron Scale: A micro-Laue Study". PhD thesis. Erich Schmid Institute of Materials Science, 2011.

[114] C. Kirchlechner, J. Keckes, C. Motz, W. Grosinger, M.W. Kapp, J.S. Micha, O. Ulrich, and G. Dehm. "Impact of instrumental constraints and imperfections on the dislocation structure in micron-sized Cu compression pillars". *Acta Materialia* 59.14 (2011), pp. 5618–5626. DOI: 10.1016/j.actamat.2011.05.037.

[115] H. Gleskova, I.-C. Cheng, S. Wagner, J.C. Sturm, and Z. Suo. "Mechanics of thin-film transistors and solar cells on flexible substrates". *Solar Energy* 80.6 (2006), pp. 687–693. DOI: 10.1016/j.solener.2005.10.010.

[116] M.J. Cordill, O. Glushko, J. Kreith, V.M. Marx, and C. Kirchlechner. "Measuring electro-mechanical properties of thin films on polymer substrates". *Microelectronic Engineering* (2014). DOI: 10.1016/j.mee.2014.08.002.

[117] V.M. Marx, F. Toth, A. Wiesinger, J. Berger, C. Kirchlechner, M.J. Cordill, F.D. Fischer, F.G. Rammerstorfer, and G. Dehm. "The influence of a brittle Cr interlayer on the deformation behavior of thin Cu films on flexible substrates: Experiment and model". *Acta Materialia* 89 (2015), pp. 278–289. DOI: 10.1016/j.actamat.2015.01.047.

[118] B. Putz, R.L. Schoeppner, O. Glushko, D.F. Bahr, and M.J. Cordill. "Improved electro-mechanical performance of gold films on polyimide without adhesion layers". *Scripta Materialia* (2015). DOI: 10.1016/j.scriptamat.2015.02.005.

[119] J. Berger. "Role of microstructure on the electro-mechanical behaviour of copper films on polyimide". MA thesis. University of Leoben, 2014.

[120] *Homepage Keithley Instruments*. Tektronix. URL: http://www.keithley.com/.

[121] M.J. Cordill and V.M. Marx. "Fragmentation testing for ductile thin films on polymer substrates". *Philosophical Magazine Letters* 93.11 (2013), pp. 618–624. DOI: 10.1080/09500839.2013.830792.

[122] B. Putz. "The influence of high current densities on intact and cracked thin gold films on flexible polyimide substrate". MA thesis. University of Leoben, 2014.

[123] O. Glushko and M.J. Cordill. "Electrical resistance of metal films on polymer substrates under tension". *Experimental Techniques* (2014). DOI: 10.1111/ext.12082.

[124] N. Lu, X. Wang, Z. Suo, and J. Vlassak. "Metal films on polymer substrates stretched beyond 50%". *Applied Physics Letters* 91.22 (2007), 379–385. DOI: 10.1063/1.2817234.

[125] T.E. Everhart and R.F.M. Thornley. "Wide-band detector for micro-microampere low-energy electron currents". *Journal of Scientific Instruments* 37.7 (1960), pp. 246–248. DOI: 10.1088/0950-7671/37/7/307.

[126] A.-D. Mueller and F. Mueller. *ANFATEC SCAN – THE IMAGE ACQUISITION*. Version 19. Anfatec GmbH.

[127] *Homepage Phytron*. Phytron GmbH. 2015. URL: http://www.phytron.at/.

[128] *Homepage Physik Instrumente.* PI Physik Instrumente GmbH. 2015. URL: http://www.physikinstrumente.de/.

[129] *Homepage Python programming language.* 2015. URL: https://www.python.org/.

Index